Ultrafast ionization and rotational dynamics of molecules in strong laser fields

Junyang Ma

2021 届研究生博士学位论文

分类号: _____ 学校代码: 10269

密级: _____ 学号: 52162099013

East China Normal University

博士学位论文

DOCTORAL DISSERTATION

分子强场电离与转动超快动力学研究

院　系： 精密光谱科学与技术国家重点实验室

专　业： 光学

研究方向： 超快激光物理

学位申请人： 马俊杨

指导教师： 吴健 教授　Olivier FAUCHER 教授

2021 年 04 月 10 日

Dissertation for doctoral degree in 2021 Student ID: 52162099013

University code: 10269

East China Normal University

Ultrafast ionization and rotational dynamics of molecules in strong laser fields

Department: State Key Laboratory of Precision Spectroscopy

Major: Optics

Research direction: Ultrafast laser physics

Candidate: Junyang MA

Supervisor: Prof. Jian WU and Prof. Olivier FAUCHER

April 10, 2021

Abstract

The investigation of ultrafast molecular dynamics is of great importance towards the understanding of a variety of natural phenomena in physical and chemical sciences. With the rapid development of femtosecond laser systems and precision detection technologies, it is possible now to visualize and steer the motion of molecules in matter as well as the ultrafast dynamics of electrons and nuclei in molecules on a microscopic timescale. When a molecule is exposed to a strong laser field, the electrons in molecule can be freed or excited, and often followed by molecular dissociation, in which the electrons and nuclei exhibit a strong correlation, while the electronic motion on attosecond timescale is much faster than that of the nuclei ranging from femtosecond to picosecond timescale. One of the examples is the absorbed photon energy shared by the electron and nucleus in molecular dissociative ionization process. In addition, a lot of physical processes such as the electron tunneling ionization have a strong dependence on the spatial orientation of molecular axes with respect to the polarization of the incident laser field. Confining molecular axes to a specific direction is significant in unambiguously understanding and control the ultrafast response of the molecules to the laser fields. The field-free molecular alignment, stimulated by the intense femtosecond laser fields, is recognized as a powerful method to control the spatio-temporal distribution of the molecular axis and serves as an important tool for studying the rotational dynamics of complex molecules and ultrafast collisional dissipation of dense gas medium.

By using the waveform controlled strong femtosecond laser fields, and the advanced detection technologies of multi-particle coincidence measurement of Cold target recoil ion momentum spectroscopy and time resolved birefringence detection, this thesis investigates the ultrafast Rydberg excitation, dissociation, rotation and collision dynamics of molecules. The main contents are summarized below.

1. Dissociative Rydberg excitation of molecule in strong laser field

The generation of Rydberg nuclear fragments in molecular dissociative ionization processes are accessed via either the frustrated tunneling ionization or the multiphoton resonant excitation. Different characteristics of these two mechanisms in kinetic energy release spectra are observed and studied in this thesis.

First, the dissociative frustrated multiple ionization of HCl molecules in near infrared femtosecond laser fields are experimentally investigated, in which processes the tunneled electrons are recaptured by the outgoing ionic nuclear fragments. Several dissociative frustrated multiple ionization channels by trapping one or two released electrons to highly excited Rydberg states are observed. The formed excited nuclear fragments, depending on their principle quantum numbers, can be either directly detected in the photoion-photoion coincidence spectrum and forming a “knee” structure in the kinetic energy release spectrum, or singly ionized by a weak static electric field of the spectrometer after the strong laser pulse and be identified in the photoelectron-photoion coincidence spectrum. The KER spectrum and momentum angular distribution of dissociative Rydberg excitation channels are similar to that of the corresponding dissociative ionization channels, which results from the electron recapture occurs at the end of the laser pulse, and thus has almost no influence on the nuclear kinetic energy.

Second, the multiphoton dissociative Rydberg excitation (DRE) of O_2 molecule in ultraviolet femtosecond laser field, forming an O and an excited O^* fragments, is experimentally observed by studying the photoelectron-photoion coincidence spectrum. The discrete peak positions of the sum kinetic energy releases spectrum of the ejected electron and nuclear fragments of the DRE channel are measured to be similar to that of the dissociative single ionization (DSI) channel. However, their nuclear kinetic energy spectra are distinct which is inconsistent with the frustrated tunneling ionization mechanism. The experimental results indicate that the absorbed photon energy above

threshold is mostly deposited to the nuclear kinetic energy in the DRE channel. While the released electron will take away a part of the absorbed photon energy in the corresponding dissociative ionization channel, resulting in a smaller nuclear kinetic energy as compared to the DRE channel. By analyzing the kinetic energies spectra, the multiphoton resonance excitation is recognized as the mechanism in accessing the DRE channel, which generally occurs when the energy gap between the excited and ground states matches the energy of one or sum of several photons. Moreover, different pathways towards the DRE and DSI are identified based on the correlated dynamics of the ejected nuclear fragments and electrons.

2. Tunneling-site-sensitive ultrafast dynamics of molecule in strong laser field

As compared to atoms, on the one hand, the dissociation accompanying multiple excitation and ionization often occurs in molecules excited by ultrashort laser pulses. On the other hand, these ultrafast processes have a strong dependence on the electron tunneling site in molecular frame. In this thesis, the electron tunneling site sensitive ultrafast dynamic in molecular dissociative ionization processes are experimentally explored.

First, molecular bond breaking is one of the key ingredients for light-induced chemical reactions. Here, the asymmetric dissociative double ionization of HCl molecules with respect to the molecular orientation and instantaneous laser field vector are experimentally revealed by employing the angular streaking technique and analyzing the asymmetric sum momentum spectra of the ejected nuclear fragments as a recoil of the ejected electrons in elliptically polarized laser pulse. Three different dissociative pathways involving various molecular orbitals of HCl are distinguished. The experimental results show that the HCl molecule is preferred to be ionized when the laser field vector points from H to Cl, which is not consistent with the expectation by a tunneling model associated with the laser induced Stark shifts of the HCl and HCl^+.

Our results indicate that the asymmetric dissociative double ionization of HCl molecules are mainly governed by the profiles of multiple molecular orbitals.

For complex triatomic molecules, the dissociative double ionization of N_2O molecule，including denitrogenation and deoxygenation channels, is experimentally investigated by using the similar procedure. Different pathways towards the denitrogenation and deoxygenation channels, involving various bound and repulsive states by removing electrons from different molecular orbitals, are uncovered by examining the momentum angular distributions and asymmetric sum momentum spectra. The experimental results demonstrate that the asymmetric dissociative double ionization of N_2O molecules are governed by the detailed potential energy curves, the profiles of the molecular orbitals, and the electron localization-assisted enhanced ionization of the stretched molecules.

Second, the strong laser field tunneling ionization induced transient valence charge localization and its ultrafast intramolecular motion are explored and visualized. Taking the dissociative single ionization of HCl as a research system, when the valence electron tunnels out with an exit near H (or Cl), an initial optical-field-induced transient charge is localized on H (or Cl) site and subject to subsequent rearrangements. The asymmetric transient charge localization, depending on the electron tunneling site in the molecular frame, is encoded in the asymmetric momentum of the outgoing proton fragments acquired from the strong laser field. Combining the angular streaking technique and axial recoil approximation, the electron tunneling site dependent asymmetric momentum angular distribution of outgoing proton fragments is clearly observed, which allows one to reveal the asymmetric initial transient charge localization.

3. Ultrafast rotational dynamics of asymmetric-top acetone molecule

Controlling molecular axes to a specific direction is a long-standing goal in ultrafast physics, which enables to distinguish the molecular orientation effect on the measured results. Impulsive alignment induced by ultrafast laser pulses with field-free revivals is

considered as a powerful method to control the spatio-temporal distribution of the molecular axes. Field-free molecular alignment is also recognized as an important tool for studying basic physical processes such as rotational dynamics of complex molecules and collisional dissipation. However, the achievement of molecular alignment for non-linear molecules is a much more challenging task, especially in the case of asymmetric-top molecules. In this thesis, the ultrafast rotational dynamics of asymmetric-top acetone molecule in gas phase in intense femtosecond laser fields is investigated by using molecular alignment and rotational echoes.

Field-free alignment revivals of acetone molecule in gas phase created by a linearly polarized laser field are observed in the experiment. By combining the measurements and calculations and comparing with the CO_2 molecule, the observed very weak alignment revivals are attributed to large molecular asymmetry, ultrafast collisional decay and multiphoton resonant dissociation. The field-free alignment degree of acetone is improved by using rotational alignment echoes excited by a pair of time delayed intense femtosecond laser pulses. As compared to the linear molecules, the fractional alignment echoes are observed in the sensitive birefringence measurement, which can be used to study the nonlinearity of complex molecular system. Moreover, the third-harmonic generation from a circularly-polarized fundamental laser pulse in a sample of aligned acetone molecules is demonstrated. The experimental findings are fully supported and reproduced by classical molecular dynamics simulations and quantum calculations.

4. Ultrafast collisional dissipation probed by molecular rotational alignment echo

The measurement of the molecular rotational dynamics in dense gas media, where interactions between atoms and/or molecules cause a rapid relaxation of the system, have attracted much attention in the past few years. In this thesis, the ultrafast collisional dynamics of molecules in dissipative media are explored by using molecular

rotational alignment echoes.

First, the ultrafast collisional dissipation of the linear CO_2 and the symmetric-top C_2H_6 molecules in pure gas and diluted in helium at high pressure (for which field-free alignment revivals are unobservable) are successfully studied by using the molecular rotational alignment echoes produced in the first few picoseconds after the laser interaction (before the appearance of the first alignment revival). The reduced amplitude of the rotational alignment echoes with increasing the time delay between the two pump laser pulses, reflecting the collisional relaxation of the system, are clearly observed by probing the transient birefringence of the medium. The measured decay time constants of the rotational alignment echoes are in good agreement with the purely classical molecular dynamics simulations. Our results demonstrate that alignment echoes enable the observation of extremely fast collisional dissipation occurring in few picoseconds for linear and symmetric-top molecules, and potentially for asymmetric-top molecules and liquid.

Second, nonsecular dynamics in ultrafast relaxation induced by thermal collisions are successfully unveiled by using rotational alignment echoes. The rotational decoherence of N_2O molecules diluted in helium mixtures created by two successive nonresonant intense femtosecond laser pulses are probed by analyzing the reduction of amplitude of the density-normalized alignment echoes with increasing the gas density at fixed time delay. The decay time constants at different times ranging from 2.8 to 17.6 ps are measured. By interrogating the system at the early stage of its collisional relaxation, a significant variation of the collisional decay time constant with the time of appearance of the rotational alignment echoes is observed, featuring a decoherence process that is well reproduced by the nonsecular equations for modeling molecular collisions. Our results indicate that the transfers among coherences as well as between populations and coherences in the nonsecular regime reduce the decoherence rate of the system lasting for a few picoseconds.

Key Words: Femtosecond laser, Strong-field tunneling ionization of molecules, Dissociative Rydberg excitation of molecules, Electron-nuclear correlated dynamics in molecules, Molecular alignment and rotational alignment echo, Asymmetry-top molecules, Collisional dissipation.

摘要

原子分子层面的微观超快动力学行为是人们认识物理和化学等自然科学的重要基础。随着飞秒激光系统和精密探测技术的快速发展，在其本征时间尺度上探测和操控物质内分子以及分子内电子和原子核的极端超快运动已经成为可能。在超快激光的作用下，分子内的电子会被电离或者激发，之后通常还会发生分子解离。在这个过程中，电子与原子核之间具有很强的关联性，尽管分子内电子运动的时间尺度在阿秒量级而核运动的时间尺度在飞秒至皮秒量级。比如在分子电离解离过程中分子内的电子和原子核共享从激光场中吸收的光子能量。不仅如此，许多的超快物理过程很大程度上依赖于分子空间取向相对于激光电场偏振方向的夹角，例如分子内电子强场隧穿电离等。将分子轴限制在特定的方向对理解和控制分子对激光的超快响应具有非常重要的意义。飞秒激光激发的分子无场排列被认为是操控分子时空间取向的有效方法，同时也是研究复杂分子转动和探测气体介质中原子分子超快碰撞的强有力工具。

本文利用时频域精密控制的超快强激光脉冲，结合多体符合测量冷靶反冲离子动量谱仪以及时间分辨双折射平衡探测等先进技术，研究了分子超快电离解离、里德堡态激发、分子转动以及超快碰撞过程，主要内容总结如下。

1. 激光驱动分子解离里德堡态激发

受挫隧穿电离和多光子共振激发是分子电离解离过程中形成里德堡态原子核碎片的两种不同激发机制。本文观测到这两种机制在核碎片动能谱中不同的特征并进行了深入研究。

首先，实验研究了氯化氢分子在近红外飞秒激光中的多重受挫电离解离，在这个过程中解离的离子碎片可以重俘获出射的电子形成高激发里德堡态原子核碎片。实验观测到了氯化氢分子的几种不同受挫电离解离通道，包括重捕获一个或者两个隧穿电离的电子到高激发里德堡态。根据形成的里德堡态原子核碎片的主量子数大小，受挫电离解离通道可以在光离子-光离子符合测量谱中被直接测

量到，并在动能谱中形成“膝盖”结构。或者里德堡态原子核碎片被谱仪中的加速直流电场电离，并在光电子-光离子符合测量谱中被甄别出来。研究发现受挫电离解离通道的原子核碎片动能分布和动量角分布与相应的电离解离通道相同，这表明电子重俘获发生在激光脉冲尾部，并对原子核碎片动能分布几乎没有影响。

此外，利用光电子-光离子符合探测技术，实验研究了氧气分子在紫外飞秒激光中的解离里德堡态激发，在这个过程中氧气分子解离生成一个中性的氧原子和一个处于高激发态的氧原子。实验结果发现氧气分子解离里德堡态通道的原子核碎片动能谱的峰值位置与氧气分子单电离解离通道的电子和原子核碎片的总动能谱的峰值位置相同。但是这两个通道的原子核碎片动能谱峰值位置是不同的，这与受挫隧穿电离机制相矛盾。实验结果表明，在氧气分子解离里德堡态通道中，分子吸收的超过阈值部分的能量主要存储在原子核碎片动能里。而在氧气分子单电离解离通道中，这部分能量被电离的电子吸收了一部分，从而使电离解离通道中的原子核碎片动能下降。通过分析能量谱，多光子共振激发被认为是紫外飞秒激光中氧气分子解离里德堡态的激发机制，这一过程通常发生在激发态和基态之间的能量差值刚好等于一个或者几个光子的能量之和时。基于观测到的分子内核与电子的关联性特征谱，本文揭示了产生氧气分子解离里德堡态通道和单电离解离通道的不同途径。

2. 激光场中与分子内电子隧穿位置相关联的超快动力学

与原子相比，一方面，分子在与超短脉冲激光作用中会发生多重电离解离以及解离里德堡态激发。另一方面，分子在激光场中的超快动力学行为与其内的电子在分子坐标系中的隧穿位置有很强的关联性。本文探究了在分子电离解离过程中与电子隧穿位置相关联的超快动力学过程。

首先，分子化学键断裂是光诱导化学反应的关键过程之一。本文利用椭圆偏振激光中的角条纹技术，测量和分析了解离离子碎片的不对称总动量谱（也就是电子的反冲动量谱），揭示了氯化氢分子空间取向相对于激光瞬时电场矢量方向的不对称双电离解离。实验观测到氯化氢分子三种不同的双电离解离路径，涉及了不同的分子轨道。实验结果表明，当激光电场矢量方向从H指向Cl时，氯化氢

分子更加容易电离解离，这与基于激光诱导的HCl和HCl^+的斯塔克移动隧穿电离模型预测结果相反。本文实验结果表明，氯化氢分子的不对称双电离解离主要是由氯化氢分子不对称的分子轨道形状决定。

对于复杂的三原子分子，采用相似的方法对一氧化二氮分子的双电离解离通道（包括脱氮通道和脱氧通道）进行了实验研究。通过分析解离离子碎片的动量角分布和不对称总动量谱，实验发现脱氮和脱氧通道是通过不同的路径实现的，这个过程涉及了多种束缚和解离态，而这些态是通过电离不同分子轨道的电子形成的。实验结果表明，一氧化二氮分子的不对称双电离解离主要由势能曲线，分子轨道形状以及电子局域增强电离共同决定。

另外，本文对由激光诱导隧穿电离引起的瞬时电荷局域及其在分子内的演化过程进行了研究。以氯化氢分子单电离解离过程为研究对象，当电子从氯化氢分子的氢原子（或氯原子）一侧隧穿电离时，激光诱导的瞬态电荷主要局域在氢原子（或氯原子）一侧，随后开始发生演化。解离氢离子碎片从激光电场中获得的不对称动量大小与其不对称瞬态电荷有关。结合角条纹技术以及傍轴近似，与电子隧穿位置相关联的氢离子不对称动量角分布被观测到，揭示了氯化氢分子单电离解离过程中的不对称瞬态电荷局域。

3. 丙酮分子的超快转动力学

将分子轴固定在特定的空间方向能够让我们辨别分子空间取向对物理测量结果的影响。由超快激光脉冲驱动的无场分子排列被认为是操控分子轴时空分布的有效方法。无场分子排列也是研究基本物理过程的重要工具，例如复杂分子的转动动力学和原子分子的超快碰撞。但是，实现激光驱动的非线性分子无场排列是一项极具挑战性的任务，尤其是不对称陀螺分子。本文利用分子排列和回声研究了不对称陀螺分子丙酮在飞秒激光中的超快转动力学。

实验观测到了由线偏振激光激发的气态丙酮分子无场排列信号。结合实验测量与理论模拟结果并与线性分子二氧化碳进行比较，观测到的极弱排列信号主要归因于丙酮分子具有较大的不对称性，分子间超快碰撞耗散和多光子共振解离。利用一对具有时间延迟的飞秒激光激发的分子转动回声，丙酮分子的无场空间排

列程度被有效提高。与线性分子相比，分数排列回声首次在双折射测量中被观察到，这一现象可以用来研究复杂分子系统的非线性效应。另外，利用排列的丙酮分子，实验产生了基频圆偏振激光的三次谐波。实验测量结果得到了经典和量子模拟计算结果的有效支持。

4. 利用分子转动回声探测超快碰撞耗散

在稠密气体介质中测量分子转动动力学在过去几年中引起了人们极大的关注，因为原子与分子以及分子与分子之间的相互作用会导致测量系统发生碰撞耗散。本文利用分子转动排列回声研究了分子在耗散介质中的超快速碰撞过程。

首先，利用分子排列回声，本文成功地在激光与气体介质相互作用之后的几个皮秒内（小于分子的第一个排列周期）研究了线性分子二氧化碳和对称陀螺分子丙烷在高气压（在此气压下分子排列信号完全消失）纯气体以及与氦气混合物中的超快碰撞耗散。实验上清楚地观察到分子排列回声幅值大小随着两束泵浦激光之间的时间延迟的增加而减小，这一现象反映了系统的超快碰撞弛豫。实验测量得到的分子转动排列回声的衰减时间常数与纯经典分子动力学模拟的结果非常相近。研究结果表明，分子转动排列回声可以在几个皮秒的时间范围内探测线性分子和对称陀螺分子在稠密介质中的超快碰撞耗散过程，并有望推广到不对称陀螺分子以及液体中。

此外，本文利用分子排列回声成功研究了分子超快碰撞耗散中的非久期动力学。以一氧化二氮分子和氦气的混合物为研究对象，实验观测到在固定的时间延时处（两束泵浦激光的时间延时），一氧化二氮分子排列回声的密度归一化幅值随气体密度的升高而减小，这一现象反映出研究体系的退相干性。实验测量了从2.8皮秒到17.6皮秒之间的分子排列回声衰减时间常数，发现碰撞衰减时间常数随分子回声出现的时间有着显着变化，这一退相干特征在理论上很好地用非久期近似模型重现。我们的研究结果表明发生在非久期近似下的相干性转移会使量子系统的退相干过程变缓，并持续几个皮秒。

关键词：飞秒激光，分子强场隧穿电离，分子解离里德堡态激发，分子内电子-核关联，分子转动排列和回声，不对称陀螺分子，碰撞耗散。

Contents

List of Figures

Chapter 1 Introduction

1.1 The interaction of light and matter

The interaction of light with matter is one of the most fundamental processes in nature, e.g., the interaction between sunlight and plants to produce oxygen to maintain our lives through photosynthesis. The investigation of mechanisms behind light-matter interaction such as the well-known photoelectric effect [1] has always been fascinating research topics. In 1960, the generation of the world's first laser [2] marked a new age for the study of the interaction of light and matter due to the high spatial and spectral coherence of the laser emission. Since then, the interest in the laser-matter interaction field has increased, mainly due to the improving capabilities to control the laser characteristics by using advanced technologies, including Q-switching [3], Mode-locking [4-6], Chirped Pulse Amplification [7], and Kerr-lens mode-locking [8], which allow the laser pulse duration to be reduced and the intensity to be increased gradually. Nowadays, ultrashort and intense lasers are powerful tools for tracing and controlling chemical reactions. In1999, the Nobel Prize in Chemistry was awarded to Zewail for his innovative contribution to the field of femtochemistry [9]. Moreover, ultrafast laser provides a lot of well-known applications to improve the quality of our daily life, such as material processing and new techniques for medical treatments.

These examples illustrate how important it is to explore and control the processes of laser-matter interaction. Recently, the rapid development of femtosecond laser and precision measurement technology have opened a new area for the investigations of microscopic reaction process at the molecular level, which is significant for understanding chemical reactions and ultrafast physics. When ultrashort and intense laser pulses interact with molecules, many interesting processes such as ionization,

dissociation, nonlinear excitation, and rotation occur. The basic concepts involved in strong laser field physics and a series of ultrafast dynamics are presented in this chapter.

1.2 Strong laser field induced molecular excitation, ionization, and dissociation

The strong laser fields with high intensity (~10^{14} W/cm^2) allow for generating an electric field equivalent to the Coulomb field inside a molecule. Therefore, the Coulomb potential barrier of molecule can be distorted drastically and the electron will be freed to continuum or excited to Rydberg states, and often followed by immediately molecular dissociation to generate outing nuclear fragments.

1.2.1 Tunneling and multiphoton ionization or excitation

A fundamental understanding of the strong field ionization was described in a pioneering theoretical model proposed by Keldysh in 1964 [10]. When a molecule is exposed to a strong laser field, the bound electron can be released by multiphoton ionization or tunneling ionization as illustrated in the sketches of Figs. 1.1, which are quantitatively distinguished by using the Keldysh parameter γ,

$$\gamma = \sqrt{\frac{I_p}{2U_p}} \tag{1-1}$$

where I_p is the ionization potential of the molecule, U_p, determined by the peak strength E and frequency ω of the laser field, is the ponderomotive energy and given by,

$$U_p = \sqrt{\frac{e^2E^2}{4m_e\omega^2}} \tag{1-2}$$

in which m_e and e are the mass and charge of electron, respectively. When the Keldysh parameter $\gamma > 1$, the ultrafast process is dominated by the multiphoton mechanism, which is often excited by the short wavelength laser field with low intensity [11]. When the intensity goes even stronger, the bound electron could tunnel out the molecular potential which are dramatically distorted by the intense oscillating electric fields. The

tunneling regime is characterized by the Keldysh parameter $\gamma < 1$, which is often induced by long wavelength laser field with high intensity [12].

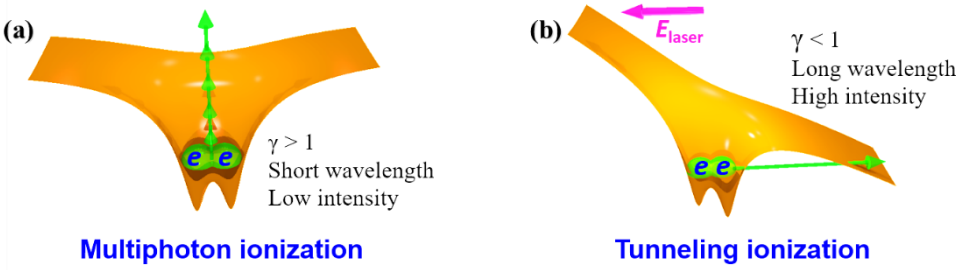

Figure 1. 1 Schematic sketches of strong laser field ionization. (a) Multiphoton ionization, (b) Tunneling ionization.

Rather than direct ionization, the molecules can also be excited into Rydberg states with extremely large orbitals. The pathways towards the Rydberg excitation are similar to the ionization in strong laser field, including multiphoton resonant excitation [13-18] and frustrated tunneling ionization [19-28].

1.2.2 Molecular dissociative ionization and Rydberg excitation

As compared to atoms, dissociation accompanying multiple excitation and ionization often occurs in molecules driven by ultrashort laser pulses [29-40]. Taking the diatomic AB molecule as an example, the AB molecule can be first singly ionized and may dissociate into $A(B)^+ + B(A)$ fragments which is usually called dissociative single ionization. As the laser intensity increases, the dissociative double and multiple ionization with the formation of $A^{m+} + B^{n+}$ fragments (*m* and *n* represent charge states) will be produced.

Interestingly, there is a certain probability that the released electrons be finally trapped by the dissociative charged fragments leading to the Rydberg fragments, which processes are schematic displayed in Fig. 1.2 for AB molecule, and usually called molecular dissociative Rydberg excitation [41-51]. The underlying physics related to molecular dissociative Rydberg excitation have been explored not only for homonuclear diatomic molecules such as hydrogen [41-43] and nitrogen [45] but also

for complex molecular targets [44]. Recently, a complete measurement of the photoelectron, ionic, and neutral Rydberg nuclear fragments from a molecule was performed [52-55], which unambiguously identified the dissociative Rydberg excitation channel and most importantly enabled to reveal the critical role of electron-nuclear correlation [53].

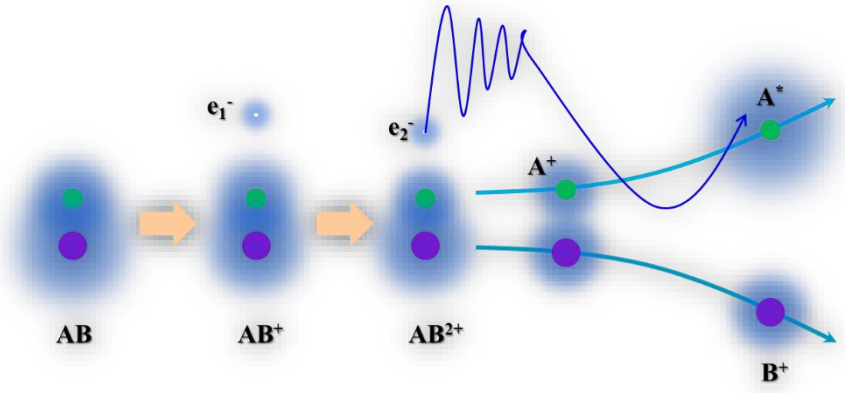

Figure 1. 2 Schematic diagram of Rydberg excitation in dissociative double ionization of AB molecule.

1.3 Electron-nuclear correlation in molecular dissociation

The understanding of motions of electrons and nuclei in a molecule are usually separated according to the Born-Oppenheimer approximation. However, the electron-nuclear correlation in molecular photoionization and fragmentation is crucial for us to study the ultrafast dynamics of molecules, which provides a novel angle to explore some interesting phenomenon such as the photon energy sharing in dissociative multiphoton ionization [56-65], high order above-threshold dissociation [66], and molecular orientation dependent tunneling ionization [67-76], which cannot be revealed if only the electrons or nuclear fragments are studied independently.

1.3.1 Electron-nuclear energy correlation in multiphoton process

In multiphoton regime, the molecular bond can be broken after the ionization if the absorption of several photons with a total photon energy exceeding the molecular

dissociation limit. The partition of the absorbed photon energy among the released electrons and dissociative fragments in molecular system are an essential process [56-63] . With assistance of the electron-nuclear joint energy spectrum, the photon energy sharing between the ejected electron and outgoing nuclei in the above threshold multiphoton dissociative ionization of diatomic molecules of H_2 and CO were observe in coincidence measurement [60-62]. The population of numerous vibrational states of the molecular cation in the ionization process is recognized as an energy reservoir in photon energy sharing between the emitted electron and the nuclear fragments [61].

1.3.2 Molecular orientation dependent tunneling ionization

Electron-nuclear energy sharing was also observed in the electron rescattering induced high order above threshold dissociation of H_2 molecules [66]. Not only is there a correlation in the sharing of observed photon energy, there is also a strong correlation between the electron tunneling site and molecular orientation in the tunneling ionization. Significant different characteristics of freed electron such as momentum distributions and ionization rate were observed for the electron released along or perpendicular to the molecular axis [77-82]. Moreover, the second electron from the up-field molecular potential well at the critical internuclear distance is more easily to be ionized after the first ionization step for symmetric H_2, N_2 and C_2H_2 molecules, which is assisted by the electron localization-assisted enhanced ionization mechanism [76, 83-92].

For heteronuclear molecules such as CO, the shape of the molecular orbitals are not symmetrical with respect to the molecular center like N_2 and H_2 molecules, the tunneled electrons with exit close to C or O site show different ionization rate, which is mainly governed by the shape of molecular orbitals [75]. Specially, the molecular orbitals structure dominated ionization model predicts that OCS molecule is preferred to be ionized when the electric field points from S to O atom, which is not consistent with the experimental observation and is explained by an tunneling model in which the laser

induced Stark shifts associated with the permanent dipoles and polarizabilities of the neutral molecule and its cation are considered [71].

1.4 Molecular rotational alignment and echo in space and time

Rotating the molecular axes to a specific direction, an efficient way to overcome the random spatial orientation, is at the heart of many ultrafast physical processes as mentioned before. The molecular rotational alignment can be achieved by three different pathways: collisional alignment [93-95], static electric field induced molecular orientation for polar molecules [96-99] and strong laser field kicked molecular alignment (orientation) [100-110].

The expression of the laser field is given by $E(t) = Ef(t)\cos(\omega t)$, where E is the amplitude, $f(t) = \exp[-(2\ln 2)t^2/\tau^2]$ is the Gaussian envelope, τ is the duration, and ω is the frequency of the laser pulse. When the laser pulse duration is longer or shorter than the molecular rotational period, the molecular alignment occurs in adiabatic or non-adiabatic regimes, respectively [100-105]. In the former, such as alignment driven by a nanosecond laser field, the molecule is excited to “pendular” states [100] and is aligned to the polarization of laser field only during the laser pulse.

The non-adiabatic regime, which applies to femtosecond laser pulse, as employed in this thesis, has advantages that other methods cannot match, such as to enable a field-free alignment of the molecules, and thus has been widely used in various applications, including molecular orbital imaging [78-82], high harmonic generation [111, 112], air lasing [113, 114], and collisional dissipations [115-123], to name but a few. Up to know, field-free molecular alignment has been achieved by molecular rotational alignment or molecular rotational alignment echoes [124-132] (more details can be found in chapter 5). In contrast to molecular rotational alignment, whose temporal positions of field-free alignment revivals are tied to the molecular rotational constants, molecular rotational alignment echoes offer much more flexibility for its time of appearance, at twice the

time delay between the two stimulated laser pulses, for what concerns the primary echo.

1.4.1 Field-free molecular rotational alignment

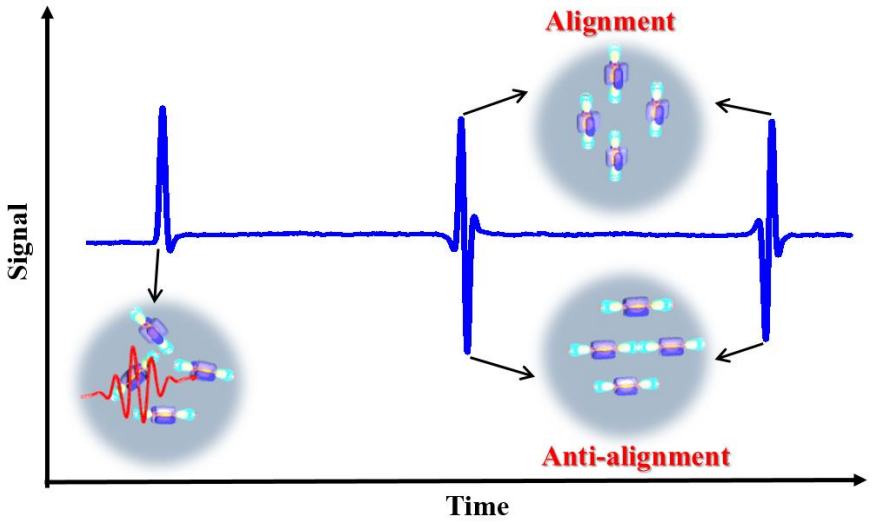

Figure 1. 3 Sketches of laser induced molecular rotational alignment for N_2O molecules.

When exposed to a strong laser pulse, the fast oscillation of electrons in the applied electric field produces an induced dipole moment [100, 104]. The torque applied to the molecule, resulting from the coupling between the induced dipole and the external field, leads to the alignment of the molecule along the laser polarization. When the pulse duration is far less than the rotational period of the molecules, the molecules are excited to higher rotational states and field-free alignment revivals [107, 133-135] are raised periodically. The alignment signals include alignment and anti-alignment, corresponding to molecular axes aligned along the polarization of the kicked laser field or delocalized in the plane perpendicular to the laser field, respectively, as schematically displayed in Fig. 1.3. The degree of molecular alignment has a strong dependence on temperature and laser parameters such as intensity and duration [136, 137]. In previous works, some approaches have been proposed for the enhancement of field-free alignment degree by applying more laser pulses at the time of maximal alignment [138, 139].

1.4.2 Molecular rotational alignment echo

Echo phenomenon is ubiquitous in nature, with the most common example of an acoustic wave reflected by the rocks: the sound echo. In 1950, the echo was firstly observed in a spin system at twice the delay between the two irradiated pulses [140]. Since then, echo effects have been investigated in various fields such as photon echo [141], plasma-wave [142], cold atoms [143, 144], particle accelerators [145], magnetic resonance imaging [146], and free electron lasers [147-150].

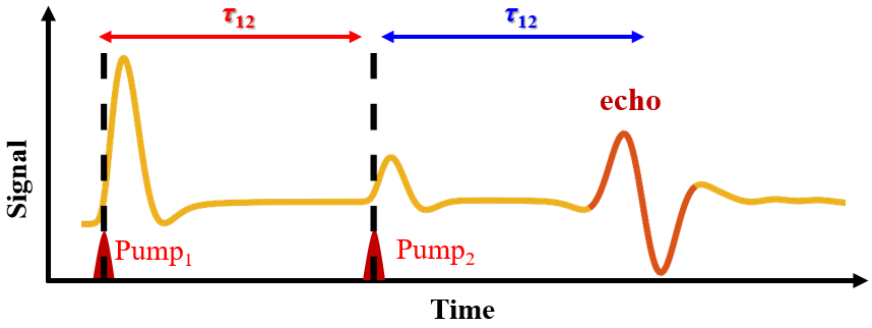

Figure 1. 4 Schematic representation of laser induced molecular rotational alignment echo.

Recently, a new kind of echo, called molecular rotational alignment echoes were discovered in gas molecules stimulated by a pair of time delayed intense femtosecond laser pulses [124, 126, 128]. For molecular rotational alignment echoes, as displayed in Fig. 1.4, the first ultrashort laser pulse produces a superposition of rotational coherences resulting in an alignment of the molecular axis along the polarization of the laser field. Soon after this excitation, the alignment vanishes due to the free evolution of the coherences. A second ultrashort pulse, delayed by τ_{12}, is then applied in order to rephase most of the coherences of the system at the time $2\tau_{12}$ where molecules realign as to form the rotational alignment echo. Note that rotational alignment echoes are classical phenomena which are different from the quantum revivals [124, 126].

1.5 Ultrafast collisional dynamics of atoms and molecules

Molecular dynamics in dissipative media, where interactions between atoms or

molecules cause a rapid relaxation of the system, have attracted much attention for their important applications in many research fields [151, 152]. Indeed, most real gas media being at non-negligible pressure, intermolecular collisions affect the spectral properties of radiative processes as well as the energy redistribution over the internal and external degrees of freedom of the system [151]. In the past few years, field-free molecular alignment induced by a linearly polarized laser pulse has been employed as a powerful tool to probe the collisional relaxation of molecules in timescales of few tens to hundreds of picoseconds [118, 119, 153-155]. The decreased amplitude of the rotational alignment revivals with increasing the time delay, reflecting the collisional relaxation of the system, have been used to track the ultrafast collisional dissipation of the molecular systems. Unfortunately, this strategy cannot be used to explore ultrafast dissipation occurring at high gas densities, because the field-free rotational alignment revivals vanish after a few tens of picoseconds due to the high collisional rate.

1.6 Theoretical descriptions of decoherence process

The theoretical descriptions of ultrafast collisional dynamics of laser stimulated field-free molecular alignment in dissipative gas media were performed by two different models in previous studies, a quantum [116, 120] and a requantized classical one [117, 156, 157]. The quantum model, using a density matrix formalism in which the effects of intermolecular collisions were described through rotational state-to-state rates constructed within the Energy Corrected Sudden (ECS) approximation, was proposed by Ramakrishna and Seideman in their pioneer papers [116, 120]. In this quantum model, the rotational state-to-state rates were independent on magnetic quantum number M, which was the projection along the polarization axis of the total angular momentum J. It turned out that the idea was good, but the model used to describe the collision was incomplete, leading to theoretical results inconsistent with the experimental observation [154].

Recently, a similar quantum treatment (requantized Classical Molecular Dynamics Simulations) for a quantitative description of the collisional dissipation of molecular alignment but with *J* and *M* dependent rotational state-to-state rates of both elastic and inelastic collisions was proposed by J.-M. Hartmann *et.al* [117, 157]. The slower decay of the permanent alignment as compared to the transient alignment, both mainly sensitive to inelastic collisions, indicated a strong propensity of the collisions to conserve the angular momentum orientation (i.e., *M/J*). This theoretical predictions were confirmed by the experimental observations [117, 154].

Until now, most of quantum models used for the calculation of dissipation induced by intermolecular collision are based upon the secular approximations which neglects transfers occurring among the coherences and between coherence and populations [151, 158, 159]. The understanding of the long-lived quantum coherence, which plays an essential role in diverse natural phenomena and technological applications, requires a detailed modeling of the system-bath interactions beyond the so-called secular approximation which provides a description of the system-bath coupling for Markovian systems [155, 158-161] that assumes that all collisions are completed and un-correlated. Despite continuous theoretical progress on understanding nonsecular dynamics, convincing experimental observations are still lacking due to nonsecular only works in a short time interval and the observable signals are generally difficult to obtain.

1.7 Organization of the thesis

By using the advanced techniques of Cold target recoil ion momentum spectroscopy and time resolved birefringence balanced detection, this thesis investigates the ultrafast ionization and rotational dynamics of molecules in intense femtosecond laser field. A general introduction into the physics of molecular excitation, ionization, dissociation, rotation and collision dynamics is presented in the chapter 1. The experimental techniques, including intense femtosecond laser system, Cold target recoil ion

momentum spectroscopy and time resolved birefringence balanced detection, are described in the chapter 2. Subsequently, the main subjects of this thesis is split into two parts.

The strong-field ionization and dissociation of molecules are experimentally investigated by using the Cold target recoil ion momentum spectroscopy. Chapter 3 focuses on the molecular dissociative Rydberg fragmentation, where two mechanisms of frustrated tunneling ionization and multiphoton resonate excitation are revealed based on the observed results. In the chapter 4, the molecular orientation dependent and electron tunneling-site-sensitive ultrafast dissociative ionization dynamics of molecules such as asymmetric transient valence charge localization are explored.

The rotational dynamics of molecules are experimentally investigated in a statics gas cell by using the time resolved birefringence balanced detection. Chapter 5 discusses the ultrafast rotational dynamics of asymmetry-top acetone molecule in strong laser field based on the molecular alignment and rotational alignment echoes. In the chapter 6, the ultrafast collisional dissipation of molecules at high gas densities and nonsecular dynamics in molecular collision is investigated using molecular rotational alignment echoes.

The last chapter is the summary and outlook of this thesis.

Chapter 2 Experimental techniques

In this chapter, the experimental techniques used throughout this thesis are presented. In the first section, the systems to generate intense femtosecond laser pulses are introduced. In the section 2.2, the multi-particle coincidence measurement of Cold target recoil ion momentum spectroscopy (COLTRIMS) and data processing are described. Finally, the time resolved birefringence balanced detection and working principle used to measure aligned molecules are depicted in the section 2.3.

2.1 Femtosecond laser systems

The generation of extremely short and intense femtosecond laser pulses is the first step to investigate the ultrafast molecular physics. The experiments performed in COLTRIMS in this thesis are stimulated by laser pulses with duration 25 fs, wavelength 790 nm, single laser shot energy 0.8 mJ, and repetition rate 10 kHz produced by FEMTOLASERS Company. The experiments performed in time resolved birefringence balanced detection are excited by laser pulses with duration 100 fs, wavelength 800 nm, single laser shot energy 3.5 mJ, and repetition rate 1 kHz generated by Spectra Physics Company. In this section, the system from FEMTOLASERS Company is selected as an example to simply describe the generation of intense femtosecond laser pulses. As schematic shown in Fig. 2.1, the laser system is mainly composed of two parts, an oscillator and an amplifier.

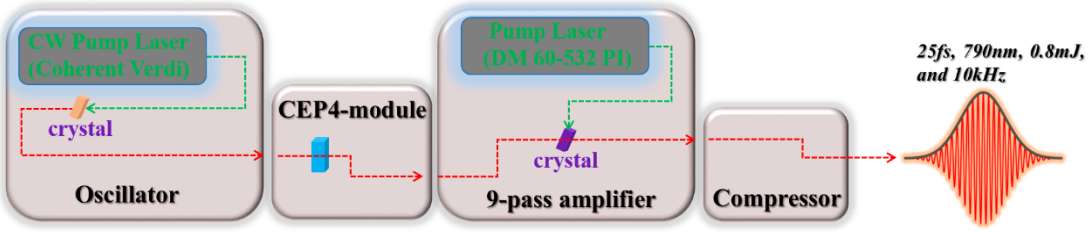

Figure 2. 1 Schematic sketches of femtosecond laser system. The propagation of laser pulses in the system are extremely complicated, here is simplified.

2.1.1 Generation of ultrashort laser pulse

According to the uncertainty principle, the full width at half maximum of laser pulse in time domain τ and frequency domain ω satisfy $\tau \times \omega \geq \kappa = 0.441$ for a Gaussian shape laser pulse. Therefore, the laser pulses with a broader wavelength spectrum have a shorter duration. The Ti:Sapphire crystal in oscillator, pumped by a laser with wavelength at 532nm, is employed to generate an ultra-wideband spectrum with wavelength ranging from 670 to 1070 nm, as schematic displayed in Fig. 2.1.

The mode locking based on the nonlinear Kerr effect to phase the modes with different frequencies in the oscillator is a key part in the generation of femtosecond laser pulses [8]. The Kerr effect means that the nonlinear relationship between the refractive index of the medium and laser intensity, which can be formulated as,

$$\mathrm{n}(\lambda, E) = n_0(\lambda) + S_1(\lambda) \times E + S_2(\lambda) \times E^2 + \cdots \quad (2\text{-}1)$$

where E is the strength of laser filed, $n_0(\lambda)$ is the intrinsic refractive index of the medium, $S_1(\lambda)$ and $S_2(\lambda)$ are the first and second order nonlinear coefficient of the medium, respectively. When a Gaussian shape laser pulse passes through the medium, the center refractive index is larger than that at edge, causing the medium itself to be equivalent to a focusing lens. Therefore, the high intensity part of laser pulses are continuously amplified until saturation, while the low intensity parts are blocked due to the larger beam spot after the laser pulses go back and forth in the oscillator many times. In addition, the laser pulse will be temporally stretched by positive dispersion after passing through the medium, a grating or prism pair or chirped mirrors with negative dispersion are employed to accurately compensate the dispersion. The parameters of final output ultrashort laser pulses from oscillator are width less than 7 fs, pulse energy less than 6 nJ, and repetition rate 75 MHz.

However, the carrier-envelope phase (CEP) [162], i.e., the relative phase between the carrier wave and the envelope of ultrashort laser pulse, is not fixed for every ultrashort pulses from oscillator. The precise and CEP stabilization, which can be

achieved by using CEP-4 module, is a key ingredient for a lot of experiments in ultrafast molecular physics. The working principle of CEP-4 can be simplified as: the carrier-envelope offset frequency is first measured and then subtracted from every single comb line in an acousto-optic frequency shifter.

2.1.2 Chirped pulse amplification

The output ultrashort laser pulses from oscillator have to be amplified before to perform strong-field experiments. However, it is easy to damage the medium during the amplification process due to the extremely high peak intensity. Chirp Pulse Amplification (CPA) technology, proposed by D. Strickland and G. Mourou in 1985 [7], was regarded as the most successful way to solve this problem, which was award the 2018 Nobel Prize in Physics [163]. In the positive dispersion, the laser pulse with shorter wavelengths are delayed more than longer ones in time, the opposite happens in case of negative dispersion, which is called “chirp”. The output femtosecond pulses from oscillator is temporally stretched (positive dispersion) by a stretcher and subsequently 9-pass amplified within a cooled Ti:sapphire crystal pumped by a strong laser pulse wavelength centered at 527 nm. The amplified laser pulses are afterwards compressed by introducing negative dispersion in compressor module. Finally, the output intense femtosecond laser pulses from amplifier provides the following parameters: pulse duration 25 fs, central wavelength 790 nm, single laser shot energy 0.8 mJ, and repetition rate 10 kHz.

2.2 Cold target recoil ion momentum spectroscopy

In the chapters 3 and 4 of this thesis, the COLTRIMS is employed for studying the laser induced ultrafast molecular ionization, excitation and dissociation processes. The generated electrons and ions are measured in coincidence [164, 165], which enables to retrieve the three dimensional momentum distributions and kinetic energy release (KER)

of ejected electrons and ions simultaneously and thus allows us to reveal the critical role of electron-nuclear correlation.

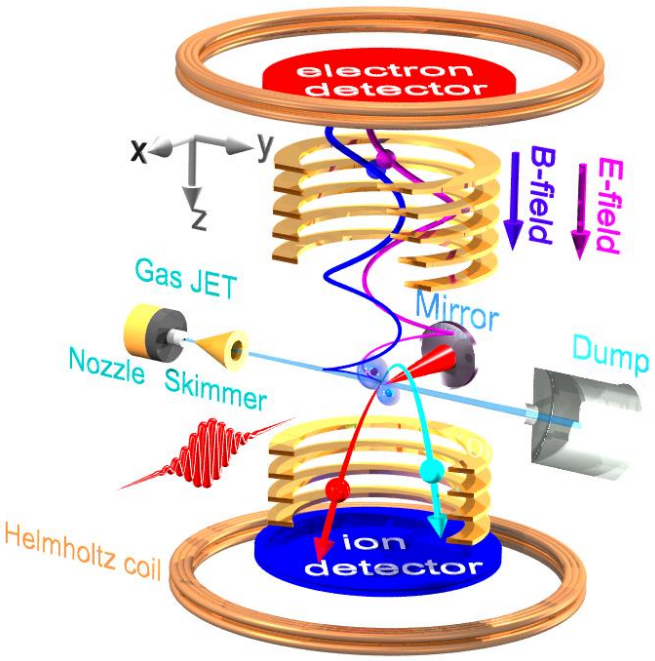

Figure 2. 2 Schematic sketches of COLTRIMS.

Briefly, as schematically illustrated in Fig. 2.2, the supersonic molecular beam propagates along $+y$ direction and interacts with laser pulses propagating along $+x$ direction after a concave reflection mirror (f = 75 mm) inside the ultrahigh vacuum chamber. The produced ions and electrons are accelerated and guide by the homogeneous weak static electric field of spectrometer and magnetic field (mainly used to force the electrons onto a helical trajectory and improve their collected efficiency), and detected in coincidence by two time and position sensitive micro channel plates (MCP) detectors at the opposite ends of the spectrometer. The homogenous magnetic field is produced by a pair of Helmholtz coils outside of the ultrahigh vacuum chamber. The homogenous static electric field of spectrometer is generated by a stack of spaced metal plates connected by high resistance. The three dimensional momenta of the detected ions and electrons are reconstructed in the off-line analysis based on the measured time-of-flight (TOF) and positions of the impacts. It should be emphasized that compared with other detections such as Velocity Map Imaging (VMI) [166, 167],

coincidence measurement is the biggest advantages of COLTRIMS.

2.2.1 Gas jet

The ultrahigh vacuum chamber, below 10^{-10} mbar in main chamber, is necessary for the coincidence measurement of ions and electrons in COLTRIMS. The molecular beam with extremely low density and temperature in laser interaction zone is produced by a supersonic gas jet [168], which enable to decrease the thermal momentum of gas target and achieve an optimal momentum resolution of the spectrometer. The supersonic gas jet is mainly composed of a nozzle with diameter of 30 μm and a skimmer with diameter of 200 μm. The high pressure (a few bars) gas at room temperature in a tube is quasistatically and adiabatically expand to low pressure region through a nozzle. Subsequently, the center of the gas beam with low density and temperature is extracted by a skimmer. The disordered gas molecules are filtered out by the skimmer and two apertures, which allow us to avoid an uncertainty between molecular beam and laser focal spot in the interaction zone. Note that the collision between molecules and/or atoms in the interaction zone is so weak that it can be ignored.

2.2.2 Spectrometer

The generated ions and electrons ejected from the molecules are detected in coincidence by two time and position sensitive MCP detectors at the opposite ends of the spectrometer. Noting the pressure in the main chamber is in the order of 10^{-10} mbar and the collisions between the charged fragments and the rest gas are unlikely. The MCP detectors are composed of MCP and delay line anode, as displayed in Fig. 2.3. When a particle (ion, electron, and excited neutral fragment) hits the inner wall of the MCP, it will trigger an electron multiplication, which increases the probability of the particle being detected. Subsequently, the generated electron cloud from the MCP is accelerated to the delay line anode which is employed to record the position.

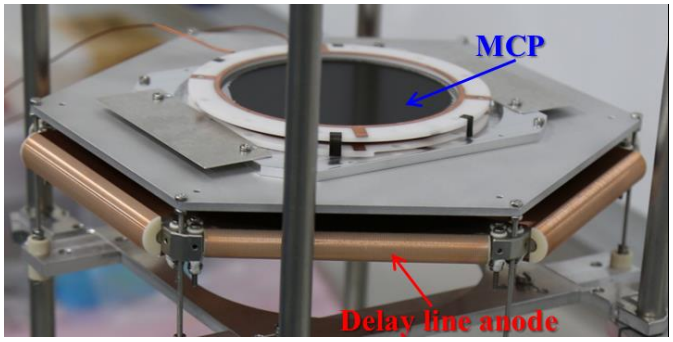

Figure 2. 3 The MCP detector, including three MCPs and one delay line anode (HEX).

The delay line anode, wound by non-insulated thin copper wire, is divided into quadrilateral (DLD) used for ion detector and hexagonal (HEX) employed for electron detector in our setup, as schematic shown in Figs. 2.4. Both work on the same principle, but the latter provides higher efficiency.

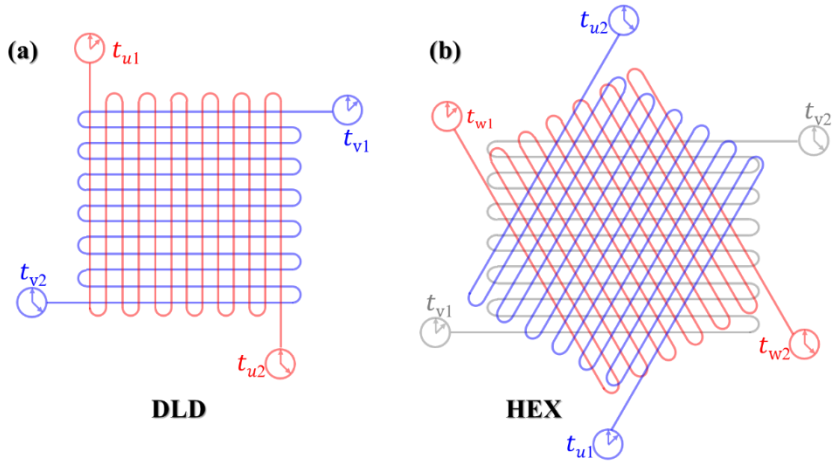

Figure 2. 4 The working mechanism diagram of delay line anode of DLD (a) and HEX (b).

Taking the DLD as an example, the electron cluster produced by MCP hits two orthogonally wound delay lines (*u* layer and *v* layer), a pair of signal pulses propagating in opposite directions with same speed are generated on each delay line. The times for the electric signal pulses on each delay line to both ends are noted as t_{u1}, t_{u2} and t_{v1}, t_{v2}, respectively, and thus the position of particle impact (u, v) can be expressed as the following formulas,

$$u = f_u\,(t_{u1} - t_{u2}) \tag{2-2}$$

$$v = f_v\,(t_{v1} - t_{v2}) \tag{2-3}$$

where f_u and f_v are coefficients related to the propagation speed of the electric signal

pulses. In general, each layer of delay lines contains a signal and a reference lines, which enable us to effectively improve the signal to noise ratio with the help of differential amplification principle.

2.2.3 Data acquisition

The obtained analogue electrical signals from the MCP and delay line anode are firstly decoupled, and then pass through a differential amplifier and an analog to digital conversion. In order to improve the accuracy of time response of signal, a Constant Fractional Discriminator (CFD) is employed. The CFD splits the input signal into two parts with different ratio. One signal is delayed by time, and another is reversed. Finally, a bipolar signal that independent on the signal amplitude is formed, and the zero point of signal is served as the digitized threshold. After CFD processing, the analogue electrical signals are converted to digital NIM (nuclear instrument methods) signals. Subsequently, a time to digital converter is used to convert the NIM signal into a computer readable digital signal. The laser trigger signal detected by a photodiode, providing the starting point of the TOF of measured particles, is processed through the similar procedure. The COBOLD software package developed by RoentDek company controls the device and performs online preliminary analysis [169]. The momentum calculation of the measured electrons and nuclear fragments is performed by using "Root" programs in the off-line analysis.

2.2.4 Three dimensional momentum reconstruction

The three dimensional momenta of the ejected particles from the interaction zone are reconstructed by solving Newton's equations based on the TOF (t) and positions (x, y) of the measured particles, the applied uniform electric field E (along $+z$), and the magnetic field B (along $+z$). For the ion detector with two layers of u and v, the relationship between the Cartesian coordinates (x_{uv}, y_{uv}) and the coordinates (u, v) is

governed by the following formulas,

$$x = x_{uv} \tag{2-4}$$

$$y = y_{uv} \tag{2-5}$$

Therefore the three dimensional momenta of the generated ionic fragments can be expressed as the following formulas,

$$P_{x(y),ion} = \frac{M_{ion} \times x(y)_{ion}}{t_{ion}} \tag{2-6}$$

$$P_{z,ion} = \frac{M_{ion} \times L_{ion}}{t_{ion}} - \frac{Q \times E \times t_{ion}}{2} \tag{2-7}$$

where t_{ion} is the TOF of ion, $x(y)_{ion}$ is the position hitting on the ion detector, L_{ion} is the distance between the interaction zone of the strong laser fields with molecules and the ion detector, M_{ion} is the mass of ion, and Q represents the charge state of ion.

For the electron detector with three layers of u, v, and w setting at angle of 60 degrees, the relationship between the Cartesian coordinates (x_{uv}, y_{uv}) and the coordinates (u, v, w) is expressed by the following formulas:

$$x_{uv} = u \tag{2-8}$$

$$y_{uv} = 1/\sqrt{3}(2v - u) \tag{2-9}$$

$$x_{uw} = u \tag{2-10}$$

$$y_{uw} = 1/\sqrt{3}(2w + u) \tag{2-11}$$

$$x_{vw} = v - w \tag{2-12}$$

$$y_{vw} = 1/\sqrt{3}(v + w) \tag{2-13}$$

Thus the three dimensional momenta of the measured electrons can be expressed as the following formulas,

$$P_{x,e} = \frac{m_e \omega_g}{2} \times \left(\frac{x_e}{\tan\left(\frac{\omega_g t_e}{2}\right)} - y_e\right) \tag{2-14}$$

$$P_{y,e} = \frac{m_e \omega_g}{2} \times \left(\frac{y_e}{\tan\left(\frac{\omega_g t_e}{2}\right)} + x_e\right) \tag{2-15}$$

$$P_{z,e} = \frac{m_e \times L_e}{t_e} - \frac{q \times E \times t_e}{2} \tag{2-16}$$

where t_e is the TOF of electron, $x(y)_e$ is the position hitting on the electron detector, L_e is the distance between the interaction region and the electron detector, m_e is the mass

of electron, and q represents the charge of electron. $\omega_g = \frac{q \times B}{m_e}$ is the gyration frequency of electron.

2.3 Time resolved birefringence balanced detection

In the chapters 5 and 6 of this thesis, the time resolved birefringence balanced detection [170, 171] is used for measuring the laser induced field-free alignment of molecules (including molecular alignment and rotational alignment echoes). The measurements performed in dense gas medium allow us to explore the interaction between molecules and/or atoms.

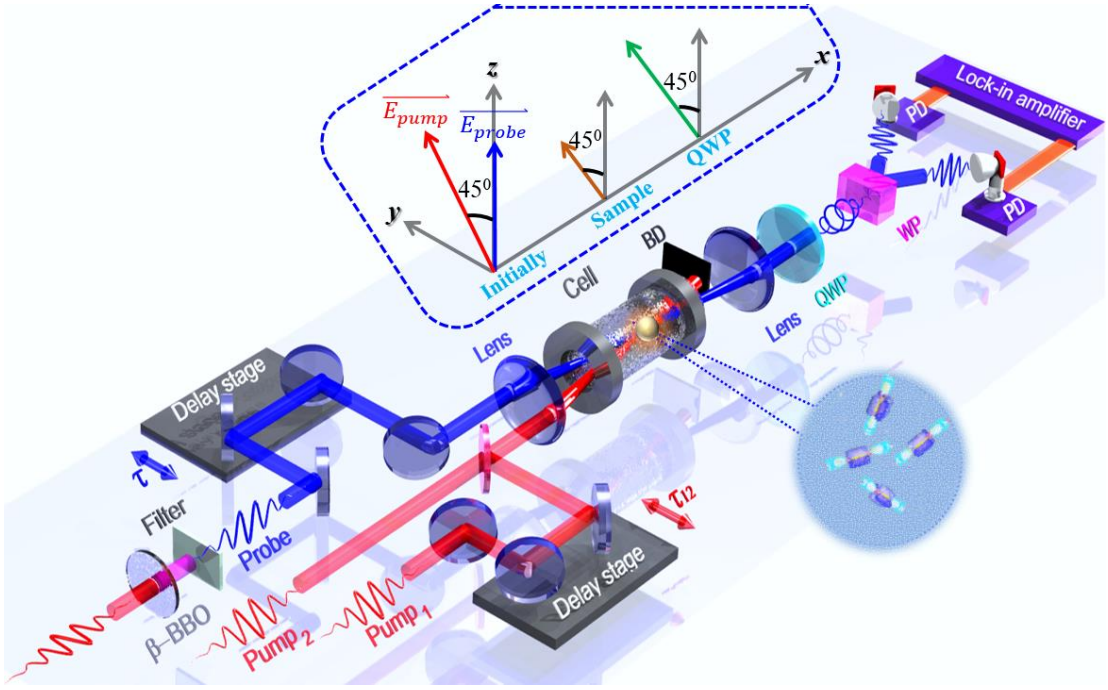

Figure 2. 5 Schematic sketches of the time resolved birefringence balanced detection. The polarization states of probe after the interaction zone and quarter wave plate are shown in the insets.

The experimental setup for the generation and measurement of molecular rotational echoes is schematically shown in Fig. 2.5. A pair of time delayed (τ_{12}) collinear pump femtosecond laser pulses (100 fs, 800 nm, 1 kHz) with parallel linear polarizations (polarized at 45° with respect to *z* axis), labeled $Pump_1$ and $Pump_2$, are tightly focused (300-mm focal lens for experiments in the chapter 5 and 100-mm focal lens for experiments in the chapter 6) into a static cell. The probe laser beam, a weak linearly

polarized (along *z* axis) ultraviolet femtosecond laser pulse centered at 400 nm produced by frequency doubling the near infrared laser pulse in a type I barium borate crystal, is temporally delayed from $Pump_1$ by τ and spatially overlapped with the pumps foci with a small crossing angle (~ 4^o) enabling to filter out the pump laser pulses after the interaction region. There is a bandpass filter (not shown) centered at 400 nm to filter out the 800nm laser pulses before the photodiode detector. One of the advantages of this approach is the cancellation of the influence of scattered photons from the pump laser pulses, especially in high-pressure samples. The energy and polarization states of the pump and probe laser beams are controlled by means of half wave plates and polarizers. For molecular alignment experiment involving a single pump excitation, the $Pump_2$ laser pulse is blocked.

The birefringence of the gas target resulting from the anisotropic distribution of molecular axes stimulated by the pump laser pulses is encoded in the modification of the polarization of the probe laser pulse, which is analyzed by a highly sensitive balanced detection, including a quarter wave plate (QWP) followed by a Wollaston prism (WP) and a balanced pair of photodiodes (PD), as shown in Fig. 2.5. The separated vertical and horizontal polarization components after the WP are independently measured by the two photodiodes, which are connected head-to-tail so that the difference of their signals is directly obtained and then amplified by a Lock-in amplifier triggered by the laser repetition rate. The amplified output signals from the Lock-in amplifier are recorded by a computer. The data acquisition and control of the motorized delay lines are interfaced by LabVIEW.

2.3.1 Pump-probe technique

To investigate the time evolution of ultrafast molecular processes such as filed-free molecular alignment, a time resolved pump-probe technique is employed in the experiment. The molecule is first excited by the pump laser pulse, and then is visualized

by the probe laser pulse with a variable time delay. In order to fulfill these requirements, a Mach-Zehnder interferometer is used as displayed in Fig. 2.6.

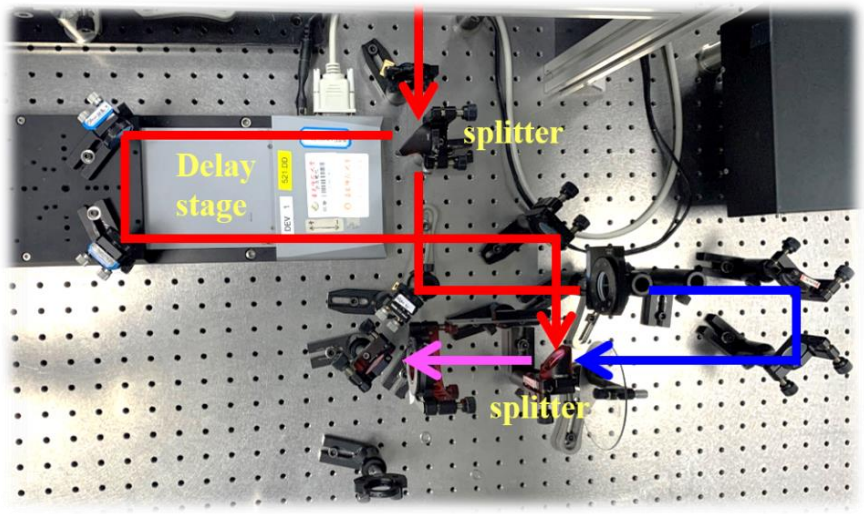

Figure 2. 6 The Mach-Zehnder interferometer.

Briefly, the output laser pulse from the laser system is split into two parts by a beam splitter which should be very thin (~1mm) in order to minimize the dispersion. Subsequently, the laser pulse characteristics such as frequency, energy, and beam size are modified individually. Finally, the laser pulses are recombined into a collinear geometry by a beam splitter (such as two pumps in Fig. 2.5) or with a small crossing angle (such as pump and probe in Fig. 2.5). The automatized linear delay stage with micrometer accuracy is employed, which allow us to precisely change the time delay between pump and probe in femtosecond timescale.

2.3.2 Optical transient birefringence induced by aligned molecules

The anisotropic distribution of the aligned molecules produces a birefringence which affects the polarization of the probe laser pulse. The latter is analyzed by using a quarter wave plate followed by a Wollaston prism in a balanced detection scheme. Before the interaction zone in gas cell, the probe laser pulse, propagating along *x* and polarized along *z* axis, can be expressed by using a Jones matrix,

$$E_{probe} = E_p \begin{bmatrix} 0 \\ 1 \end{bmatrix} \begin{matrix} y \\ z \end{matrix} \qquad (2\text{-}17)$$

The aligned molecular gas sample can be assimilated to a birefringence wave plate

which fast axis is along the polarization of pump lase pulse. Thus the Jones matrix of aligned molecular gas sample is given by [172],

$$W_{sample} = \begin{bmatrix} \cos\frac{\delta}{2} & -i\sin\frac{\delta}{2} \\ -i\sin\frac{\delta}{2} & \cos\frac{\delta}{2} \end{bmatrix} \quad (2\text{-}18)$$

where $\delta = (n_{\parallel} - n_{\perp})\frac{\omega L}{c} = \Delta n\frac{\omega L}{c}$ is the phase difference, ω is the angular frequency of the probe laser pulse, L is the interaction distance of pump and probe laser pulses, c is the velocity of light. $n_{\parallel} = n_0 + \frac{N\Delta\alpha}{2n_0\varepsilon_0}\left(\langle\cos^2\theta\rangle - \frac{1}{3}\right)$ and $n_{\perp} = n_0 - \frac{N\Delta\alpha}{4n_0\varepsilon_0}(\langle\cos^2\theta\rangle - \frac{1}{3})$ are the parallel (along the polarization of pump laser pulse) and vertical refractive index of gas media (linear molecules) [110, 173-175], in which N is the number density of molecules, θ is the angle between the molecular axis and the pump pulse polarization, $\Delta\alpha = \alpha_{\parallel} - \alpha_{\perp}$ is the polarizability difference, ε_0 is the dielectric constant of vacuum, and n_0 is the linear refractive index. $\Delta n = n_{\parallel} - n_{\perp} = \frac{3N\Delta\alpha}{4n_0\varepsilon_0}(\langle\cos^2\theta\rangle - \frac{1}{3})$, in which the $\left(\langle\cos^2\theta\rangle - \frac{1}{3}\right)$ is usually used to characterize the degree of molecular alignment.

The optical axis of the quarter wave plate is placed at 45° between the *y* and *z* axis, its Jones matrix is,

$$W_{QWP} = \frac{1}{\sqrt{2}}\begin{bmatrix} 1 & -i \\ -i & 1 \end{bmatrix} \quad (2\text{-}18)$$

Therefore, after passing through the gas sample and quarter wave plate, the final output probe laser pulse is given by,

$$E_{output} = W_{QWP}W_{sample}E_{probe} = \frac{E_p}{\sqrt{2}}\begin{bmatrix} -i\sin\frac{\delta}{2} - i\cos\frac{\delta}{2} \\ \cos\frac{\delta}{2} - \sin\frac{\delta}{2} \end{bmatrix} \quad (2\text{-}19)$$

The horizontal and vertical laser pulses are separated by using a Wollaston prism and then send to a pair of photodiodes. The output signal from the balanced detection is the intensity difference between the measured horizontal and vertical laser pulses, which is given by $S = S_H - S_V = I_{probe}\sin(\delta)$ where I_{probe} proportional to E_p^2 is the intensity of probe laser pulse. The phase difference δ induced by pump laser pulses in gas sample is too small so that $S \approx I_{probe}\,\delta = I_{probe}\frac{\omega\Delta nL}{c} \propto (\langle\cos^2\theta\rangle - \frac{1}{3})$, thus the

measured S is proportional to the birefringence of medium and directly reflects the molecular alignment degree [170, 171].

2.3.3 Balanced photodiodes detector and Lock-in amplifier

In the measurement, the heterodyne signals are measured by a balanced detection. One of its most important advantages is to effectively reduce the noise caused by the laser intensity fluctuations and significantly improve the signal to noise as compared to the homodyne signals [172], and also to provide a signal that is proportional to $(\langle\cos^2\theta\rangle - \frac{1}{3})$, which is not the case for an homodyne detection unable to distinguish between molecular axes aligned or anti-aligned [110, 176, 177]. It should be noted that the probe laser pulse energy is set to less than 10 nJ in order to avoid the saturation of the photodiodes and to reduce the alignment of molecules induced by the probe itself. The analogue signals output from the balanced detection are sent to a Lock-in amplifier. Lock-in amplification is a well-known phase-sensitive technique made to distinguish the components of the signals at a specific reference frequency in order to filter out the noise at frequencies other than the reference [178], which in our experiment is the trigger-out of the laser. After a series of processing by the Lock-in amplifier, the output signal (mainly amplitude in our measurement) is recorded by the computer.

2.3.4 Data processing and analysis

The data acquisition systems in the measurement can simultaneously get the delay stage position (time delay between pump and probe laser pulses), the Lock-in amplifier output signals, and the gas pressure in the static cell. Subsequently, these information are stored to a .TXT file in the computer. The data analysis, such as the measure of amplitude of the molecular rotational echoes and the numerical fittings of the data, is then performed by using a Matlab software.

Chapter 3 Dissociative Rydberg excitation of molecule in strong laser field

In this chapter, the dissociative Rydberg excitation of molecule in strong laser field is experimentally investigated by using the COLTRIMS. In the first section, two different mechanisms to access dissociative Rydberg excitation of molecules are introduced. In the section 3.2, the coincidence measurements of dissociative Rydberg fragments by using two different techniques are presented. In the section 3.3, the dissociative multiple Rydberg excitation of HCl molecules induced by frustrated tunneling ionization is explored. Finally, in the section 3.4, the dissociative Rydberg excitation of O_2 molecules excited by multiphoton resonant excitation is studied and the electron-nuclear correlation in molecular dissociative processes is discussed.

3.1 Dissociative Rydberg excitation of molecule

The generation of Rydberg nuclear fragments in molecular dissociative ionization processes can be achieved via either the frustrated tunneling ionization [19-28] or the multiphoton resonant excitation [13-18]. In the multiphoton resonant excitation scenario, the formation of Rydberg fragments generally occurs when the energy gap between the excited and ground states matches the energy of one or sum of several photons. However, in the frustrated tunneling ionization scenario, the ejected electron cannot obtain enough drift energy from the laser field to overcome the attractive Coulomb potential of the parental nucleus, and thus recaptured by the dissociative ionic fragment to form the Rydberg fragment at the ends of the strong laser pulse.

3.2 Coincidence measurement of Rydberg nuclear fragments

The coincidence measurement of Rydberg fragments formed in molecular dissociation processes are achieved by two different techniques: Photoion-photoion coincidence (PIPICO) [52-54, 179, 180] and Photoelectron-photoion coincidence (PEPICO) [24, 28, 181, 182].

3.2.1 Photoion-photoion coincidence (PIPICO)

The generated dissociative Rydberg fragments can be charged and neutral. For the former case, the charged Rydberg fragment and ionic fragment ejected from a multiply ionized molecule are accelerated by the static electric field of the spectrometer and coincidently detected by ion detector. Taking the dissociative frustrated triple ionization of HCl molecule as an example [183], i.e., $HCl \xrightarrow{\text{laser field}} H^+ + Cl^{+*} + 2e^-$, in which process one of the three released electrons is recaptured by the Cl^{2+} fragment forming Cl^{+*} fragment, the dissociative ionic fragments H^+ and Cl^{+*} are coincidently measured by employing the PIPICO spectrum, as shown in Fig. 3.1. However, this PIPICO line also contains the dissociative double ionization of HCl molecule, i.e., $HCl \xrightarrow{\text{laser field}} H^+ + Cl^+ + 2e^-$, which can be distinguished from each other in the KER spectrum as discussed in the following.

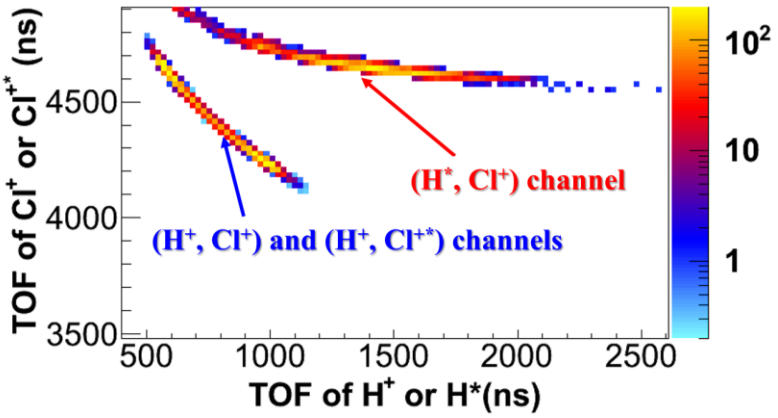

Figure 3. 1 Measured PIPICO spectrum of the (H^+, Cl^+), (H^+, Cl^+) and (H^*, Cl^+) channels.

For the latter case, the neutral Rydberg fragment with a certain kinetic energy and

internal potential energy larger than the working function of MCP has a certain probability to be directly detected by the ion detector [19, 41, 184], featured with a much longer TOF as compared to the photoionization created charged ions [52, 54, 179]. For instance, the generation of H^* and Cl^+ fragments in dissociative frustrated double ionization of HCl, i.e., $HCl \xrightarrow{\text{laser field}} H^* + Cl^+ + e^-$ (in which process one of the two ionized electrons is recaptured by the H^+ fragment forming H^* fragment), is coincidently measured and identified in the PIPICO spectrum as shown in Fig. 3.1. Note that only the initial momentum of H^* fragment towards the ion detector can be coincidently detected with Cl^+ fragment [54].

3.2.2 Photoelectron-photoion coincidence (PEPICO)

The ionic or neutral Rydberg fragments with very high principle quantum number formed in molecular dissociation process can be afterwards field ionized by the weak static electric field (DC-field) of the spectrometer in COLTRIMS [24, 28, 181, 182], and thus the higher charged fragments are eventually measured by the ion detector. Taking the processes involving laser induced dissociative Rydberg fragments and postpulse field ionization by DC-field of HCl molecule as an example [183], i.e., $HCl \xrightarrow{\text{laser field}} H^+ + Cl^{q+*} + (q+1)e^- \xrightarrow{\text{DC-field}} H^+ + Cl^{(q+1)+} + (q+2)e^-$, the pathways of "$Cl^{+*} \xrightarrow{\text{DC-field}} Cl^{2+} + e^-$" and "$Cl^* \xrightarrow{\text{DC-field}} Cl^+ + e^-$" are distinguished in the PEPICO spectrum, as displayed in Fig. 3.2. When the electron TOF is smaller than about 60 ns, the electron is mainly released by the strong laser field. When the electron TOF is larger than about 100 ns, the electron is mainly freed by the DC-field. It should be noted that the measured longer TOF of electron is attributed to the lifetime of Rydberg fragment and the TOF of electron from releasing to arrival at the electron detector, because the starting point of TOF is triggered by the laser pulse as mentioned in the chapter 2.

The lowest principle quantum number n_F of a neutral Rydberg fragment being ionized by the DC-field is roughly calculated by using the Saddle point approximation,

which is expressed as $F_{dc}=1/(9n_F^4)$ in atomic units, where F_{dc} is the strength of DC-field. For the case of charged Rydberg fragment, the influence on the charge state is considered and thus $F_{dc}=Z^3/(9n_F^4)$ where Z represents the charge state [185].

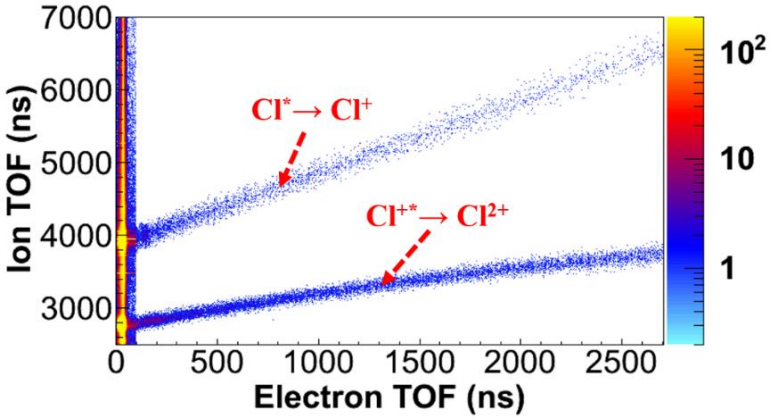

Figure 3. 2 The measured PEPICO spectrum of HCl. A couple of postpulse ionization channels for the highly excited ion fragments, i.e. $Cl^{q+*} \xrightarrow{\text{DC-field}} Cl^{(q+1)+}$ where (q = 0,1), are denoted by the red dashed arrows.

3.3 Dissociative frustrated multiple ionization of HCl molecule

In this section, the dissociative frustrated multiple ionization of HCl molecule is experimentally investigated by using linearly and circularly polarized femtosecond pulses with duration 25 fs and wavelength 790 nm [183]. The peak intensities of the linearly and circularly polarized laser fields are estimated to be 5×10^{14} W/cm^2 and 9×10^{14} W/cm^2, respectively. The corresponding Keldysh parameters for the linear and circular polarization conditions are 0.48 and 0.35, both lying in the tunneling regime. The strength of the DC-field of the spectrometer is 22.2 V/cm, and the neutral Rydberg fragments with principal quantum number $n > 70$ can be ionized by the DC-field. The excited Rydberg fragments, depending on their occupied principle quantum numbers, can be either directly identified by employing the PIPICO spectrum or singly ionized by the DC-field after the laser pulse and distinguished in the PEPICO spectrum.

3.3.1 Rydberg fragment with low principle quantum number

Figures 3.3(a) and (b) show the measured KER spectra of dissociative multiple ionization of HCl molecule, i.e., HCl → H^+ + Cl^{q+} + (q+1)e^- denoted as HCl (1,q) channels, in the linearly and circularly polarized laser fields, respectively. In Fig. 3.3(a), the clear "knee" structures located at the high energy side of the main peak are observed. Interestingly, the "knee" structure from the HCl (1,q) channels approximately lines up with the main peak of the HCl (1,q+1) channels, which are manifested by the green guiding dashed lines in the plot.

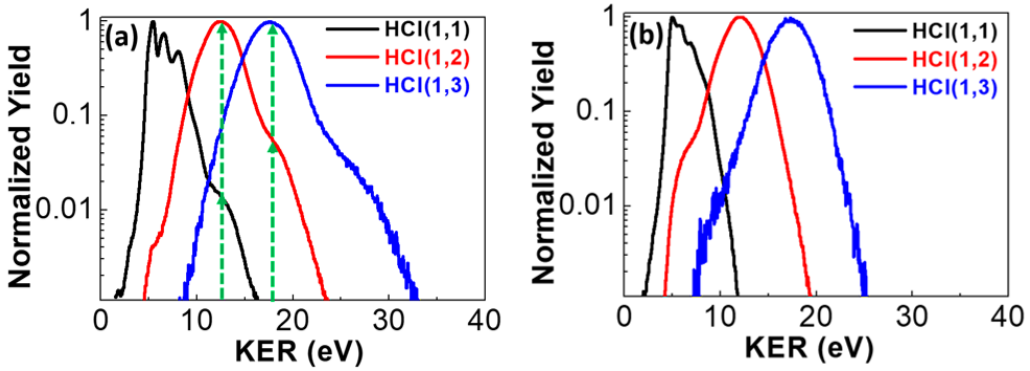

Figure 3. 3 (a) The KER spectra of the HCl (1,q) (q=1, 2, and 3) channels in linearly polarized laser field. (b) The same to (a) but for circular polarization.

According to precious works [41, 44], the electron recapture occurs approaching the end of the stimulated laser pulse and thus the recapture of the electron to the ionic fragment has trivial influence on the KER distributions of dissociative nuclear fragments. For example, the KER distribution of dissociative frustrated ionization (H^+, H^*) is similar to that of the dissociative ionization (H^+, H^+) [41, 54]. This indicates that the signal in the "knee" structure mainly from the dissociative frustrated multiple ionization, i.e., HCl → H^+ + Cl^{q+*} + (q+1)e^- denoted as HCl (1,q^*) channels, and the measured excited fragments Cl^{q+*} with lower principle quantum numbers survive in the DC-field of the spectrometer and thus finally be detected by the ion detector. The "knee" structures are absent in the circularly polarized laser field as shown in Fig. 3.3(b), which provides a well verification for the frustrated tunneling ionization mechanism [41, 46].

The electron localizing on the hydrogen core, and forming the HCl (*,q) channel, i.e., $HCl \rightarrow H^* + Cl^{q+} + qe^-$, is also observed in the measurement. Note that the polarization of linearly polarized laser filed is rotated to *z* axis in order to increase the collection efficiency. The PIPICO spectrum of HCl (*,1) channel is displayed in Fig. 3.1 and the KER spectrum of the HCl (*,1) is presented in Fig. 3.4. The main peaks of KER distributions of HCl (*,1) channel is attributed to the electron recaptured by the ionic hydrogen. Interestingly, by comparing with the KER spectrum in circular polarization, the "knee" structures around 11-14 eV are observed for both the HCl (1,1) and HCl (*,1) channels in linear polarization, indicating that the HCl (*,1) channel in this KER range is formed by recapture of two electrons by both the ionic chloride and the hydrogen. In principle, the probability for two electron recapture is much smaller than that for the single recapture case, which is consistent with the previous study performed in argon dimer [44] .

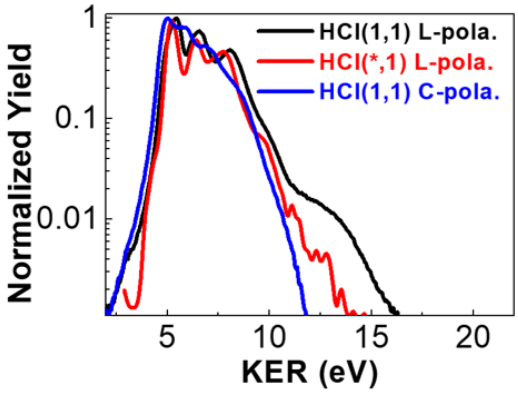

Figure 3. 4 The KER spectra of the HCl (*,1) channel in linearly polarized laser field and of the HCl (1,1) channel in both linear and circular polarization.

3.3.2 Rydberg fragment with high principle quantum number

The dissociative excited fragment Cl^{q+*} with high principal quantum number can be ionized by the DC-field of the spectrometer, thus the $Cl^{(q+1)+}$ fragment is formed and finally measured by the ion detector. The processes involving electron-recapture-induced excitation and postpulse DC-field ionization can be expressed as $HCl \xrightarrow{\text{laser field}} H^+ + Cl^{q+*} + (q+1)e^- \xrightarrow{\text{DC-field}} H^+ + Cl^{(q+1)+} + (q+2)e^-$, and is denoted as HCl (1,$q^* \rightarrow$q+1)

channel in the following discussion. As displayed in Fig. 3.2, the long lived highly excited fragments Cl^{q+*} can be easily distinguished with diagonal distributions, the survival time of Cl^{q+*} can be retrieved as T_{elec} - T_0, where T_0 = 36 ns is the most probable TOF of electrons released in the strong laser field, T_{elec} is the measured TOF of individual electrons. The retrieved survival times of the fragments Cl^{q+*} in the HCl (1, $q^* \rightarrow q+1$) channels (q = 0, 1) are plotted in Fig. 3.5.

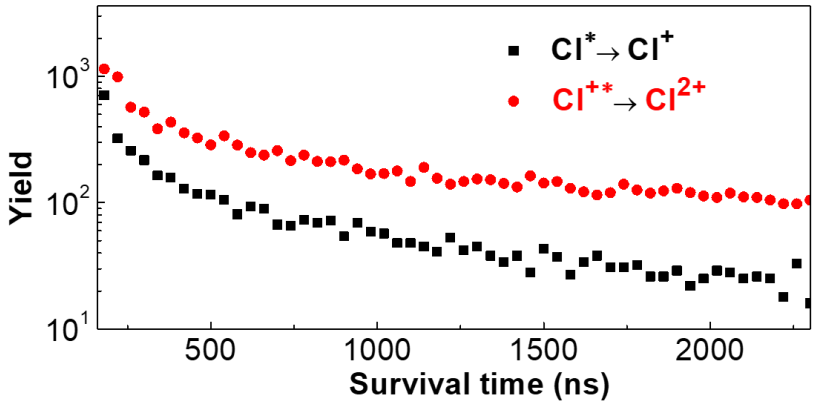

Figure 3. 5 Retrieved survival time of the $Cl^{q+*} \xrightarrow{\text{DC-field}} Cl^{(q+1)+} + e^-$ pathways (q = 0, 1).

The processes of "$Cl^{+*} \xrightarrow{\text{DC-field}} Cl^{2+}$" and "$Cl^{*} \xrightarrow{\text{DC-field}} Cl^{+}$" are also clearly observed in the plot of TOF as a function *y* position of ions, as shown in Fig. 3.6. Besides the major signal distributions around the TOFs of 2752 ns and 3891 ns corresponding to the fragments of Cl^{2+} and Cl^+, the additional distributions extending from the main distributions are measured. Starting from two extreme cases, one is that the generated dissociative excited fragments Cl^{+*} are ionized by the DC-field immediately after the strong laser pulses, their TOF will be the same as that of the Cl^{2+}. On the other hand, when the fragments Cl^{+*} are ionized right before its arrival at the ion detector, the TOF will be the same as that of Cl^+. Two pairs of elongated distributions between the Cl^+ (TOF_{Cl^+} = 3891 ns) and the Cl^{2+} (TOF_{Cl^+} = 2752 ns) peaks are observed in Fig. 3.6, in which the outer line extended within the displacement of about ±2.8 mm to ±5.5 mm in the *y* direction is caused by "$Cl^{+*} \xrightarrow{\text{DC-field}} Cl^{2+}$" pathway, while the inner pair lying at smaller *y* positions with |y| < 2.8 mm is attributed to the delayed

dissociation of the long-lived HCl^{2+} [186]. Moreover, the longer linear distribution starting from the Cl^+ peak and occupying the long TOF region along the y = 0 axis is mainly attributed to the "Cl^{*} $\xrightarrow{\text{DC-field}}$$Cl^{+}$" pathway.

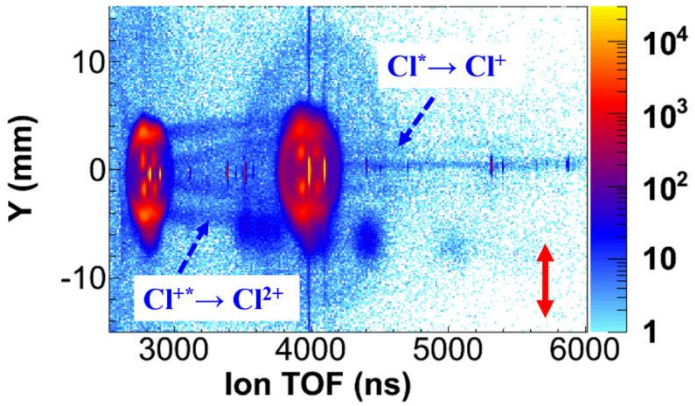

Figure 3. 6 Ionic yields as a function of TOF and displacements in the *y* direction of HCl molecules in strong laser field. The polarization direction is indicated by the red arrow.

The three dimensional momentum of the $Cl^{(q+1)}$ fragment from "Cl^{q*} $\xrightarrow{\text{DC-field}}$$Cl^{(q+1)}$" channel are reconstructed by solving the Newton's equations of $P_{x(y)} = M_{Cl}L_{x(y)}/T_{ion}$ and $P_z = [M_{Cl}L_z - \frac{1}{2}qE(T_{ion} - T_{elec} + T_0)^2]/T_{ion}$. Here T_{elec} is the TOF of electron, T_{ion} is the TOF of ion, $L_{x(y)}$ is the position of ion hitting on the detector, L_z is the distance between the interaction zone of the strong laser fields and the ion detector, E is the strength of applied static DC electric field of the spectrometer, M_{Cl} is the mass of ionic fragment, and q represents the charge state of ion. The tiny recoil momentum of the ejected electron from the DC-field-induced ionization of the Cl^{q+*} fragments is neglected here, and thus the momentum distributions and KER spectrum of the HCl $\xrightarrow{\text{laser field}}$ $H^+ + Cl^{q+*} + (q+1)e^-$ channel are similar to that of the HCl $\xrightarrow{\text{laser field}}$ $H^+ + Cl^{q+*} + (q+1)e^- \xrightarrow{\text{DC-field}} H^+ + Cl^{(q+1)+} + (q+2)e^-$ channel.

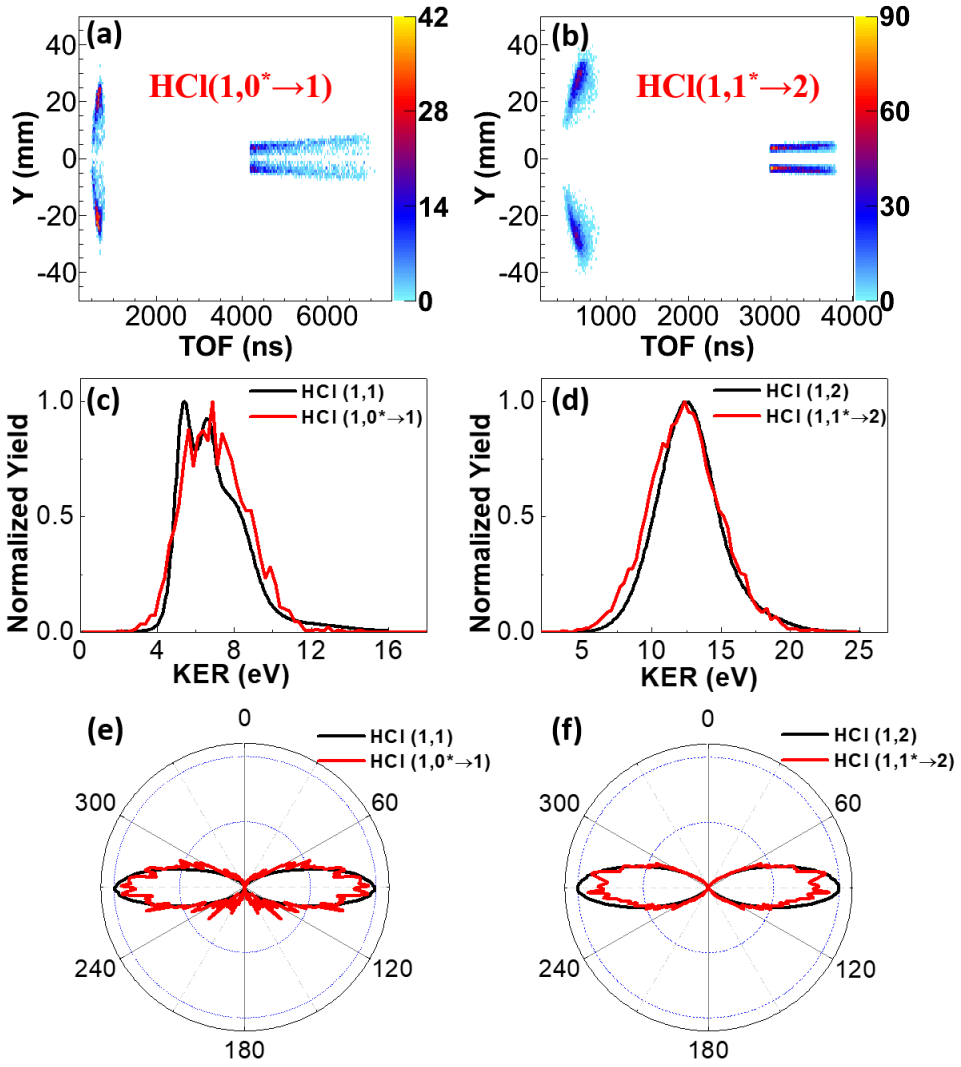

Figure 3. 7 (a) (b) Ionic yields as a function of TOF and *y* positions of the HCl (1,q^*→q+1) channels. (c) (d) The KER spectra of the HCl (1,q+1) and the HCl (1,q^*→q+1) channels. (e) (f) Polar plots of the momentum angular distributions of the HCl (1,q+1) and the HCl (1,q^*→q+1) channels in the polarization plane. Here, q = 0, 1.

Figures 3.7(a) and (b) display the measured ion yields of H^+ and $Cl^{(q+1)+}$ fragments from the HCl (1,q^*→q+1) channels (q = 0, 1) as a function of the ion TOF and *y* positions, which are selected based on the law of momentum conservation of the two measured nuclear fragments and PEPICO spectrum. Figures 3.7(c-f) (red solid curves) are the measured momentum angular distributions and KER spectrum of the HCl (1,q^*→q+1) channels (q = 0, 1). For comparison, the corresponding measurements of the HCl (1,q) channels are shown by the black solid curves. The similar KER spectra and angular distributions are observed for both the HCl (1,q^*→q+1) and HCl (1,q+1)

channels, which indicate that the HCl $(1,q^{*}\rightarrow q+1)$ channel is excited by the frustrated tunneling ionization mechanism. The narrow momentum angular distributions along the laser polarization direction (90º and 270º) suggest that the dissociation process occurred within a femtosecond timescale.

3.4 Electron-nuclear correlation in dissociative multiphoton ionization and Rydberg excitation of O_2 molecule

The electron-nuclear correlation in the dissociative single ionization ($O_2 + n\hbar\omega \rightarrow O + O^+ + e^-$, denoted as DSI channel) and dissociative single Rydberg excitation ($O_2 + n\hbar\omega \rightarrow O + O^*$, denoted as DRE channel) of O_2 molecule are experimentally investigated in this section [187]. Both channels are excited by a linearly polarized (along *y* axis) ultraviolet femtosecond laser pulse centered at 395 nm produced by frequency doubling a near infrared laser pulse with 25 fs and 790 nm in a β-barium borate crystal. The peak intensity of the laser field in the interaction zone is measured to be 4.0×10^{13} W/cm^2 with a corresponding Keldysh parameter of 3.3, and thus in the multiphoton ionization regime. The strength of the DC-field of the spectrometer is 8.7 V/cm, and the neutral Rydberg fragments with principal quantum number $n > 90$ can be ionized by the DC-field.

3.4.1 Dissociative single Rydberg excitation of O_2 molecule

The DRE channel should be most likely to be generated as for its low excitation energy, but yet lacks direct experimental observation, because the unexcited neutral fragment O cannot be detected by ion detector and thus leading false coincidence measurement with O^* fragment in the PIPICO spectrum. However, the fragment O^* with high principal quantum number has a certain probability to be ionized by the DC-field of the spectrometer and identified by employing the PEPICO spectrum, as shown in Fig. 3.8 between the two blue dotted lines. The horizontal line centered at ion TOF

of 5826 ns in the plot is the false coincidence events, which is exclude in the data analysis process. The processes involving photon excitation created Rydberg fragments O^* and the post-pulse DC-field ionization, i.e. $O_2 + n\hbar\omega \rightarrow O + O^* \xrightarrow{\text{DC-field}} O + O^+ + e^-$, is denoted as $O_2(^*\rightarrow 1,0)$ channel in the following discussion. As displayed in Fig. 3.8, the process of postpulse DC-field ionization of highly excited Rydberg particles is not restricted to O^* fragments but can also be observed in O_2^*.

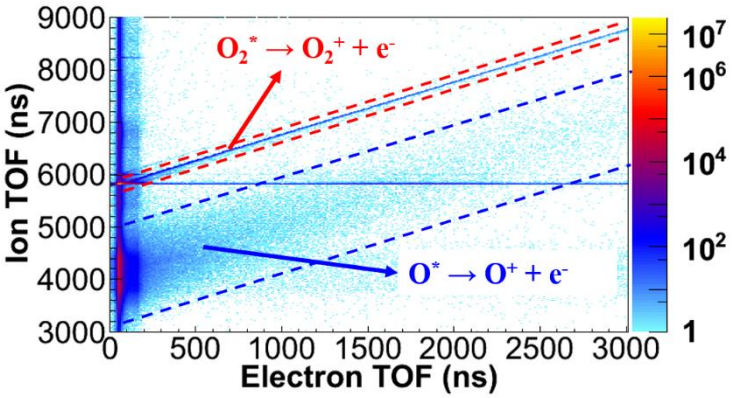

Figure 3. 8 The PEPICO spectrum of O_2 molecules stimulated by a linearly polarized ultraviolet femtosecond laser pulse.

The three dimensional momentum distributions of nuclear fragments O^+ in the $O_2(^*\rightarrow 1,0)$ channel can be obtained by solving the Newton's equations as used in the last section. The kinetic energy of the neutral fragment O is calculated according to the recoil momentum of the detected O^+ ejected from the a molecule. As mentioned before, the tiny momentum of the ejected electron induced by the DC-field ionization is neglected, and thus the KER spectrum of nuclear fragments, labeled as E_N in the plot, in $O_2(^*\rightarrow 1,0)$ is similar to that of the DRE channels. Figures 3.9(a) and (b) (blue line) are the momentum distributions in *y*-*z* plane and KER spectrum of the nuclear fragments of the DRE channel. The KER spectrum of associated DSI channel measured in the same experimental condition is displayed by the red curve in the plot. According to the frustrated tunneling ionization mechanism, both DRE and DSI channels should have almost the same KER spectrum of nuclear fragments, which is not the case in present work and thus excludes the electron recapture scenario.

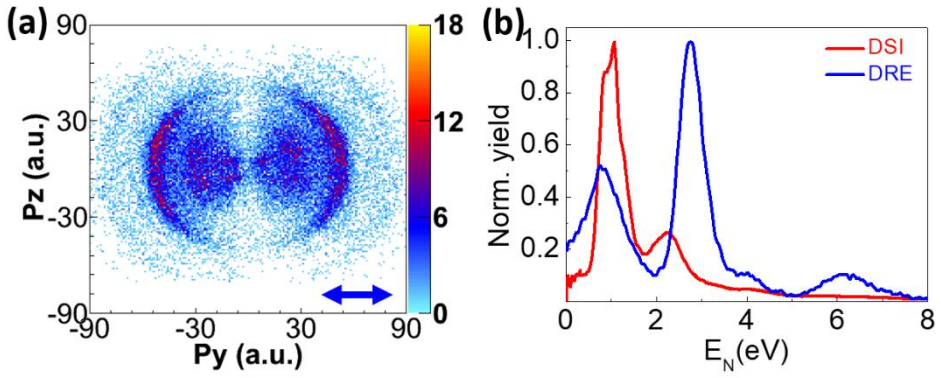

Figure 3. 9 (a) The momentum distribution in the *y*-*z* plane of the DRE channel. The blue arrow represents the polarization of the laser field. (b) The KER spectra of the DSI and DRE channels.

3.4.2 Correlation of dissociative single Rydberg excitation and ionization channels

In the multiphoton processes, the absorbed photon energy above the dissociation threshold of molecule is deposited to the KER of outgoing electrons and the dissociative nuclear fragments via their interaction [53, 56, 61]. The sum-kinetic energy of the ejected electron and nuclear fragments of the DSI and DRE channels are given by $E_{sum} = E_N + E_e = E_O^+ + E_O + E_e \approx n\hbar\omega - D_{ls} - U_p$ for the DSI channel, and $E_{sum} = E_N = E_O^* + E_O = E_O^+ + E_O \approx n\hbar\omega - D_{lr} - U_p$ for the DRE channel. Here, n, U_p, D_{ls}, and D_{lr} denote the number of absorbed photons with energy of $\hbar\omega$ (~3.15 eV), the ponderomotive energy of the electron in the oscillating laser field (~0.5 eV in this experiment), and the corresponding dissociation limitations of the DSI and DRE channels, respectively. The value of D_{lr} are similar to that of D_{ls} due to the high principal quantum number of Rydberg fragments in the measurement. According to the E_{sum} formula, the peak positions of the E_{sum} spectrum of DRE channel should be similar to that of DSI channel in the multiphoton resonance excitation and ionization if molecules absorb a same number of photons in accessing two channels.

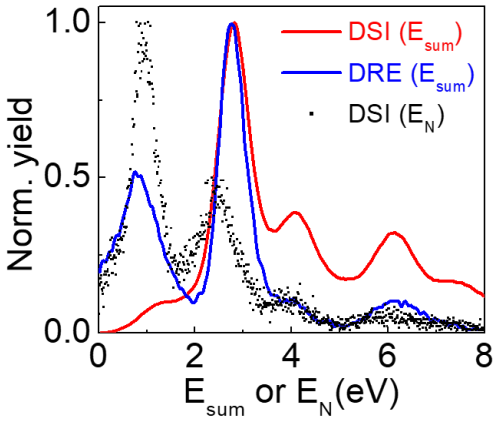

Figure 3. 10 The sum-kinetic energy spectra of the DSI and DRE channels. The black dots represents the E_N of DSI channel by gating the energy of electrons smaller than 0.2 eV.

As shown in Fig. 3.10, the similar peak locations of the E_{sum} are observed for the DSI and DRE channels, which provides an evidence for the preliminary guess. As for the different KER spectrum observed in Fig. 3.9(b) for DSI and DRE channels, recall that the E_{sum} formula of the DSI and DRE channels, as compared to the DRE channel, the absorbed photon energy above the ionization threshold can be carried by the freed electron in the DSI channel, thus leading to a higher KER values in the DRE channel than that of the DSI channel. By comparing the observed features of the DSI and DRE channels in Figs. 3.9(b) and 3.10, the multiphoton resonance excitation is recognized as the scenario to access the DRE channel.

3.4.3 Different pathways towards dissociative channels

Figure 3.11(a) shows the joint energy spectrum (JES) of the coincidently measured electron and nuclear fragments of the DSI channel, where the multiple diagonal lines indicate that the observed photon energy sharing between the emitted electron and nuclear fragments. The horizontal lines in Fig. 3.11(a) indicate the the population of various vibrational states of the molecular cation as observed in CO molecules [61]. However, different from the simplest H_2 molecules [60], various molecular orbitals and electronic states are involved in the DSI channel of O_2 molecule, leading to a superposition of several sets of structure in the JES.

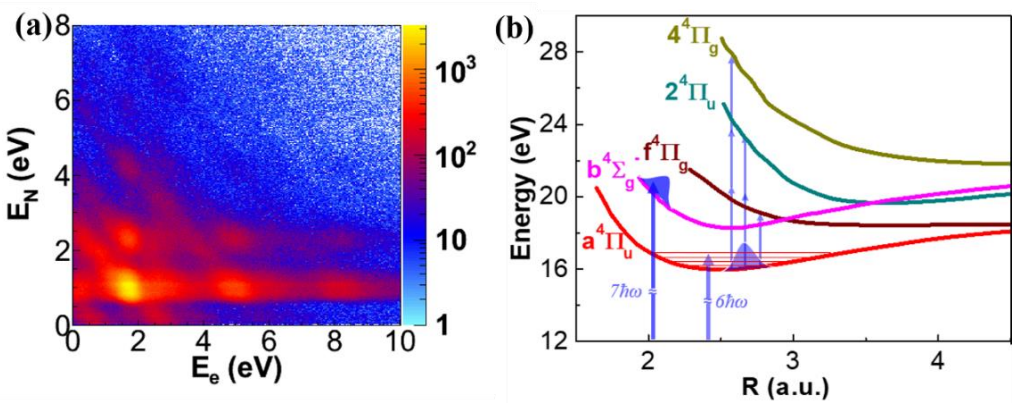

Figure 3. 11 (a) Measured electron-nuclear joint energy spectrum of the DSI channel. (b) Relevant potential energy curves of O_2^+ adopt from [188, 189], and a simplified transition scheme of different pathways towards the DSI channel.

Figure 3.11(b) shows the relevant potential energy curves of the O_2^+. The $a^4\Pi_u$ state is populated by removing one electron from the HOMO-1 by absorbing six photons, which is then more likely photon-coupled to various dissociative states. According to the selection rules of the dipole transition [188], the DSI channel with KER bigger than 0.6 eV may be accessed via three different pathways, as illustrated in simplified transition scheme in Fig. 3.11(b). The photon ionization created nuclear wave-packet on the $a^4\Pi_u$ state can be one-, two- and three-photons coupled to the $f^4\Pi_g$, $2^4\Pi_u$ and $4^4\Pi_g$ repulsive states followed by immediately dissociation to different limits and ending with KER values centered at 1.0, 2.3 and 4.2 eV, respectively. As can be seen in Fig. 3.11(a), the first order E_{sum} values corresponding to three different KER values are centered at 2.8, 4.1, and 6.1 eV, respectively. Note that multi-order E_{sum} spectrum spaced by the photon energy is observed in the same pathway caused by above threshold ionization. The KER region smaller than 0.6 eV is most likely produced in the following pathway: removal of one electron from the HOMO-2 by absorbing seven photons and one of the quartet states $b^4\Sigma_g^-$ is launched, part of O_2^+ populated on this state with sufficient energy is dissociated with E_{sum} centered at 1.0 eV. By considering different numbers of absorbed photons and molecular dissociation limits, the expected first order E_{sum} values of the $b^4\Sigma_g^-$, $f^4\Pi_g$, $2^4\Pi_u$ and $4^4\Pi_g$ states are 0.9, 2.7, 4.0, and 5.9 eV, respectively, which agree with the experimentally measured values.

As discussed above, the absorbed excess photon energy is mainly deposited to the nuclear fragments in the DRE channel, and thus the DSI and DRE channels should have similar peak positions in KER spectrum when E_e closes to zero in the DSI channel, as shown in Fig. 3.10 (black dots), which imply the correlation between electrons and nuclear fragments. In analogy to the DSI channel, for the DRE channel, the neutral O_2 molecules absorb seven, seven, eight, and nine photons from the strong laser field and populate to four different Rydberg states (very close to the $b^4\Sigma_g^-$, $f^4\Pi_g$, $2^4\Pi_u$ and $4^4\Pi_g$ states) followed by immediate dissociation, generating fragments O and O^* with KER centered at 0.9, 2.8, 4.0, and 6.2 eV, respectively. For instance, the neutral O_2 molecule on the ground state may absorb seven photons to the Rydberg state (very close to the $f^4\Pi_g$ state) with a dissociation limit of 18.8 eV. According to the formula $E_{sum} = E_N = E_O{}^* + E_O \approx n\hbar\omega - D_{lr} - U_p$, an $E_N \approx 2.7$ eV is obtained, which agree with the observed E_N of 2.8 eV in the measurement.

3.5 Conclusions

In this chapter, different characteristics were shown in the processes of molecular dissociative Rydberg excitation accessed via the frustrated tunneling ionization and multiphoton resonance excitation. For the former, the dissociative frustrated multiple ionization of HCl molecule stimulated by a near infrared intense femtosecond laser pulse was experimentally investigated. The excited charged fragments, depending on their occupied principle quantum numbers, can be either directly identified in the PIPICO spectrum, or singly ionized by the DC-field and be distinguished in the PEPICO spectrum. The KER spectrum and momentum angular distribution of the nuclear fragments of dissociative Rydberg excitation channel were similar to that of the corresponding dissociative ionization channel, which was generally explained by the electron recapture occurs at the end of the laser pulse, therefore it has almost no effect on nuclear dynamics.

For the latter, the dissociative single Rydberg excitation of O_2 molecules in ultraviolet femtosecond laser fields was experimentally studied by using the PEPICO spectrum. The absorbed photon energy above threshold was deposited to the nuclear kinetic energy in the dissociative Rydberg excitation. While the released electron took away part of the absorbed photon energy in the corresponding dissociative ionization channel, resulting in a smaller nuclear kinetic energy, which processes were well revealed by studying the electron-nuclear correlation. By considering the total kinetic energies of all the ejected particles with that of the dissociative single ionization channel, the multiphoton resonance excitation was recognized as the underlying mechanism.

Chapter 4 Tunneling-site-sensitive ultrafast dynamics of molecule in strong laser field

In this chapter, the electron tunneling site sensitive ultrafast dynamic in molecular dissociative ionization are explored. In the first section, the concept of angular streaking in elliptically polarized laser pulse is presented. In the section 4.2, the molecular orientation dependent dissociative double ionization of HCl molecule and N_2O molecule are experimentally investigated. In the section 4.3, the asymmetric transient valence charge localization and its evolution is observed and studied in molecular orientation dependent dissociation of HCl molecule.

Note that the theoretical calculations presented in the section 4.3 were performed by Dr. H. Ni, which are only briefly described in this thesis.

4.1 Angular streaking by elliptically polarized laser pulse

Driven by an elliptically polarized femtosecond laser pulse, the tunneled electron acquires a final momentum approximately vertical to the instantaneous electric field vector at the ionization instant, which is called angular streaking [91, 190, 191]. Taking the dissociative single ionization of HCl molecule driven by a counter-clockwise rotating elliptically polarized laser field as an example, as schematic illustrated in Fig. 4.1, a bound electron (represented by a pink ball) freed by an instantaneous electric field pointing to -*y* will primarily tunnel from the +*y* site, and end up with a final momentum almost along the +*z* axis. Vice versa, a bound electron freed by an instantaneous electric field pointing to +*y* will primarily tunnel from the -*y* site, and end up with a final momentum almost along the -*z* axis. If the induced laser field is a clockwise rotating elliptically polarized laser field, a bound electron freed by an instantaneous electric field pointing to -*y* (+*y*) will primarily tunnel from the +*y* (-*y*) site,

and end up with a final momentum almost along the -*z* (+*z*)axis.

Meanwhile, the ejecting direction of the nuclear fragments such as H^+ from the breaking molecule provides the orientation of the molecule axis at the ionization instant according to the axial recoil approximation [192]. Thereby, by measuring the ejected electron and nuclear fragments in coincidence, the molecular orientation and the tunneling site of photoelectron in the molecular frame can be determined. Moreover, the electron recollisional processes are omitted in elliptically polarized laser field with large ellipticity, and thus only sequential multiple ionization is occurred [191].

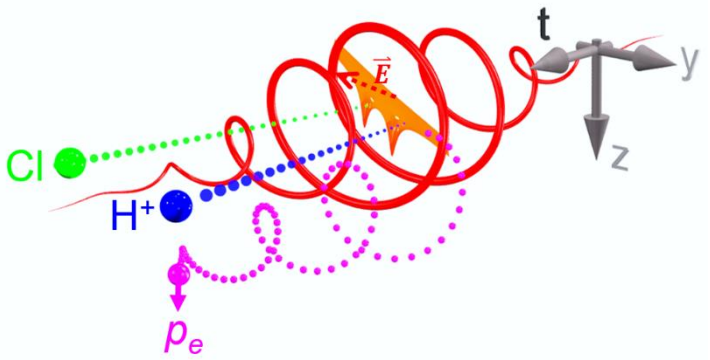

Figure 4. 1 Schematic sketches of angular streaking driven by an elliptically polarized laser pulse.

4.2 Molecular orientation dependent ionization and dissociation

In this section, the laser field vector dependent intrinsic dissociative double ionization of the diatomic heteronuclear molecule HCl and more complex triatomic molecule N_2O are experimentally explored by employing the angular streaking technique in elliptically polarized laser pulse [186, 193]. The instantaneous asymmetry of the molecular bond breaking is revealed by gating the ejected direction of the ionic fragments and tracing their sum momentum spectra as a recoil of the ejected electrons, which encode the instantaneous vector of the laser field at the ionization instants. Different pathways towards the dissociative double ionization channels, involving various bound and repulsive states and molecular orbitals, are discussed.

4.2.1 Molecular orbital dominated ionization of HCl molecule

Different pathways toward dissociative double ionization of HCl molecule ($HCl \rightarrow H^+ + Cl^+ + 2e^-$, denoted as HCl (1,1) channel) are experimentally explored by using the linearly and elliptically polarized intense femtosecond laser field with duration 25 fs and wavelength centered at 790 nm. The peak intensity and ellipticity of the elliptically polarized laser field are measured to be 9.0×10^{14} W/cm^2 and 0.72, with its major and minor polarization along the *y* and *z* axes, respectively. For the laser intensities used in present work, the Keldysh parameters is estimated to be smaller than 1, and thus in the tunneling ionization regime.

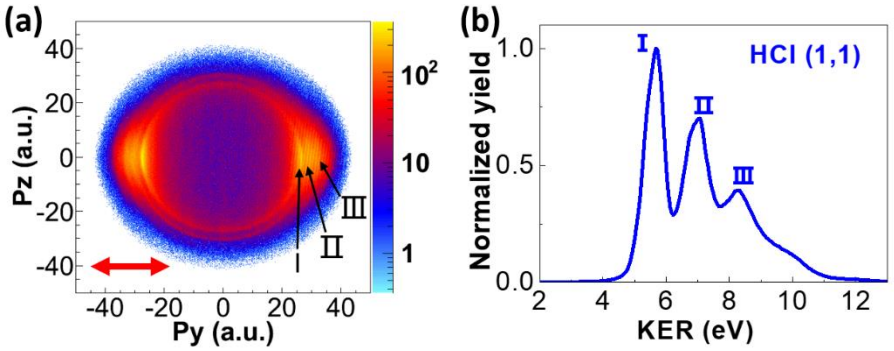

Figure 4. 2 (a) The momentum distributions of the ionic fragments of HCl (1,1) channel. The red arrow represents the polarization of the laser field. (b) The corresponding KER spectrum.

The momentum distributions in the *y*-*z* plane and the KER spectrum of the HCl (1,1) channel induced by a linearly polarized laser field (along *y* axis and intensity of 3.4×10^{14} W/cm^2) are shown in Figs. 4.2(a) and (b), respectively, three distinct ring structures corresponding to three different KER values centered around 5.7, 7.0 and 8.2 eV (marked as I, II, and III) are measured. More events being detected along the polarization of laser field indicates that the molecular bond is more easily to be broken when the molecular axis is paralleled to the laser field polarization. The higher KER components beyond 8 eV shows relatively narrower momentum angular distribution than that of the KER peaks I and II region, which is maybe attributed to the released electrons from different molecular orbitals.

According to precious studies, the freed electrons from different molecular orbitals can be distinguished by analyzing the asymmetric KER-dependent sum momentum distributions of ionic fragments in elliptically polarized laser field, which are mainly given by their distinct molecular orbital profiles [60, 75]. As mentioned before, for the counter-clockwise rotating electric fields (from +*y* to +*z*), the electrons with final momentum along the -z/+z axis are released when the instantaneous laser field points to the +*y*/-*y* directions. The momentum distributions of the sequentially ejected two electrons are imprinted on the ion sum momentum distributions of the correlated ionic fragments according to the law of momentum conservation (i.e. $pz_{sum} = pz_{H^+} + pz_{Cl^+} = -(pz_{e1} + pz_{e2})$, in which direction our apparatus has the best momentum resolution). The sum momentums of the fragment ions can be used to reveal the instantaneous vector and strength of the rotating laser field at the instant of the ionization.

Figure 4.3(a) shows the KER dependent ion sum momentum distributions of the HCl (1,1) channel along the *z* axis for the emitted ionic fragments within a cone of 45° with respect to the *y* axis. Three distinct peaks around 0 and ±1.8 a.u. are identified in pz_{sum} distribution, which indicate different emission properties of the sequentially released two electrons in dissociative double ionization. The distribution around $pz_{sum} = 0$ a.u. is recognized as the events when the two electrons are ejected to the opposite directions, i.e., the first (second) electron tunnel from the +*y* (-*y*) site or the first (second) electron tunnel from the -*y* (+*y*) site. The two side peaks centered at $pz_{sum} = \pm 1.8$ a.u. are mainly contributed by events where both electrons are released from the same directions (both electron tunnel from the +*y* (-*y*) site for $pz_{sum} = -$ (+) 1.8 a.u), as shown in the sketches of Fig. 4.3(a)).

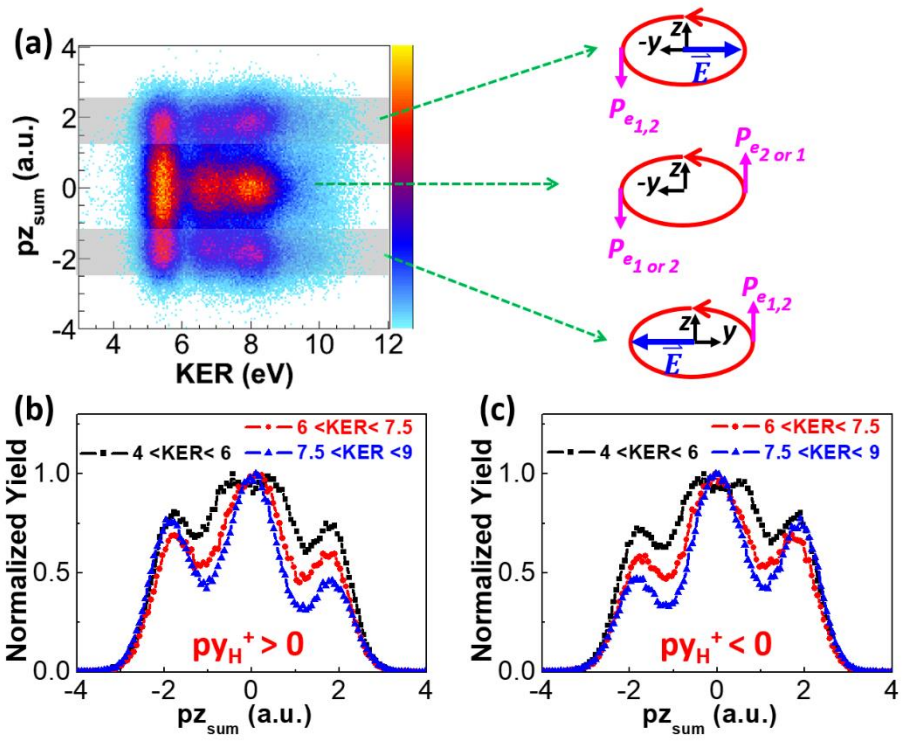

Figure 4. 3 (a) The KER-dependent ion sum momentum distributions and the sketches of four different emission properties of the two ionized electrons. The projections over different KER range are shown for the H^+ emits to the (b) $+y$ direction and (c) $-y$ direction, respectively.

As shown in Figs. 4.3(c) and (d), the KER-integrated ion sum momentum display asymmetric distributions when the ejected H^+ ions is distinguished to the $+y$ or the $-y$ directions. The asymmetric pz_{sum} spectra indicate that the HCl molecule is preferred to be ionized when the laser field vector points from H to Cl, which is not consistent with the expectation by a tunneling model associated with the laser induced Stark shifts of the HCl and HCl^+. As shown in Fig. 4.4 (a), the HOMO of HCl is π-orbital which is homogeneously distribution around the H and the Cl nuclei, while the HOMO-1 (σ-orbital) exhibits asymmetric distributions, and more electron density is located around H site, so that the electron is preferred to be released when the laser filed vector point from H to Cl. In Figs. 4.3(c) and (d), comparing to that of the two lower KER regions (<7.5 eV), the larger asymmetry of pz_{sum} distribution is observed for the high KER range (7.5-9 eV), which indicates a possible contribution from the HOMO-1 in the double ionization process for the high KER range.

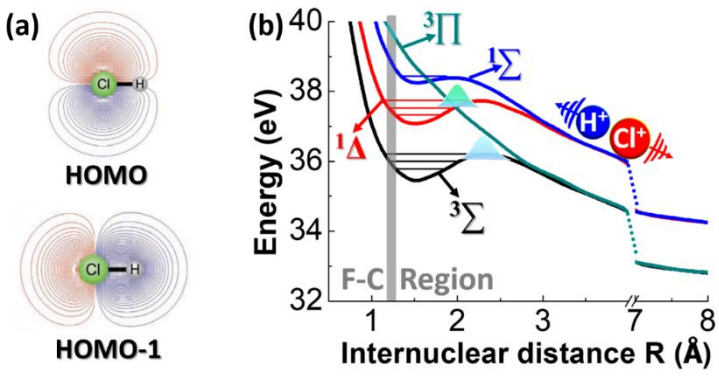

Figure 4. 4 (a) The profiles of HOMO and HOMO-1 of HCl molecule adopted from [194]. (b) Relevant potential energy curves of the HCl^{2+}, adopted from [195].

According to the momentum angular distributions, the asymmetric ion sum-momentum distributions of ionic fragments and the relevant potential energy curves of the HCl^{2+} as shown in Fig. 4.4(b), the three peaks in the KER spectrum of the HCl (1,1) channel are expected to access via three different pathways. The KER range between 4-6 eV (Peak I) and 6-7.5 eV (Peak II) with broader momentum angular distributions and smaller asymmetry in the ion sum momentum distributions are produced by removing two electrons from the HOMO and the nuclear wave packet (NWP) is launched on the ground state $^3\Sigma$ of the HCl^{2+}, then the NWP is excited to the $^3\Pi$ repulsive state by absorbing one and two extra photons, respectively. For the KER beyond 8.2 eV (Peak III) with a relatively narrow angular distributions and a larger asymmetries in the ion sum momentum distributions, the two individual electrons are most probably removed from the HOMO and the HOMO-1, respectively, accompanying with the NWP being ignited directly to the higher energy regions on the repulsive $^3\Pi$ state. Note that the two released electrons from HOMO-1 will contradict the KER distributions of the present measurements.

4.2.2 Distinct asymmetries of denitrogenation and deoxygenation channels in doubly ionized N_2O molecule

The Coulomb exploded double ionization of N_2O molecules in linearly and

elliptically polarized femtosecond laser pulses with duration 25 fs and wavelength centered at 790 nm is experimentally investigated. Two different dissociative ionization channels, i.e. $N_2O \rightarrow NO^+ + N^+ + 2e^-$ (labeled as denitrogenation channel) and $N_2O \rightarrow N_2^+ + O^+ + 2e^-$ (labeled as deoxygenation channel) are produced. The intensities of the linearly polarized and elliptically polarized laser fields are same and estimated to be about 6.0×10^{14} W/cm^2, the corresponding Keldysh parameter is calculated to be about 0.43 and thus in the tunneling regime. The denitrogenation and deoxygenation channels accessed via various pathways are discussed based on the measured momentum angular distributions and asymmetric ion sum momentum.

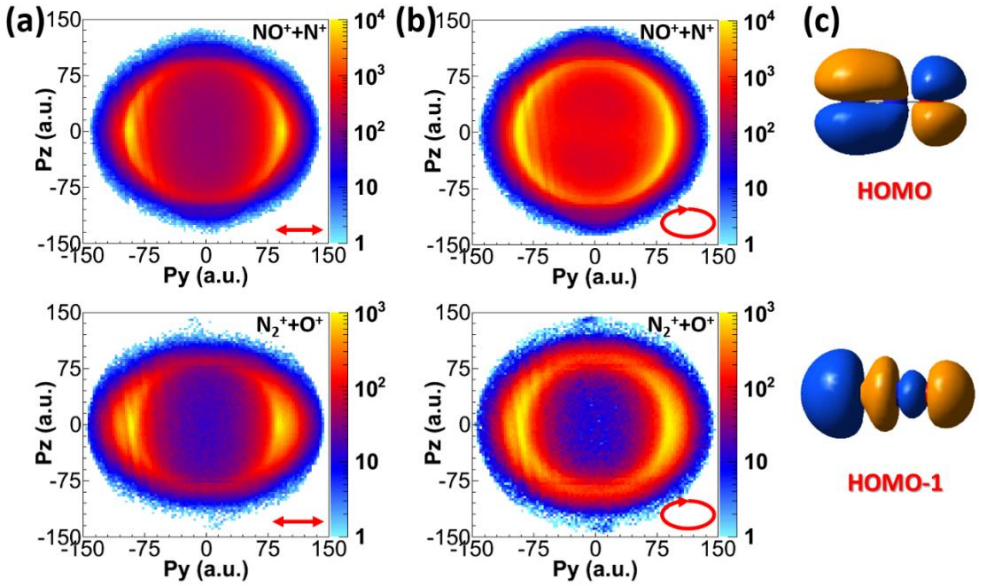

Figure 4. 5 (a), (b) Momentum distributions of the denitrogenation and deoxygenation channels driven by a linearly polarized (a) and elliptically polarized (b) laser field. The red arrow represent the polarization of the laser field. (c) The profiles of the HOMO and HOMO-1of N_2O, where the nuclei N-N-O lie from the left to right sides.

Figure 4.5(a) shows the momentum distributions of the denitrogenation and deoxygenation channels in the *y*-*z* plane driven by a linearly polarized laser field, where the angular distribution of denitrogenation channel is relatively broader than that of the deoxygenation channel. The concentrated distributions along the laser polarization suggest that the N_2O molecule is preferred to be broken when the molecular bond is aligned in the polarization of laser filed. In the following, the directional breaking of

N_2O molecules as a function of the instantaneous vector of a counter-clockwise rotating elliptically polarized femtosecond laser pulse ($\varepsilon \sim 0.86$) is investigated. As mentioned before, the sum momentum of sequential released two electrons is mapped on the sum momentum spectrum of the correlated fragment ions, e.g., $pz_{sum} = pz_{ion1} + pz_{ion2} = -(pz_{e1} + pz_{e2})$ along *z* axis.

The molecule aligned parallel to the major axis of the elliptically polarized laser field is predominantly ionized and dissociated according to the momentum distributions in Fig. 4.5(b). Therefore, the fragments emitting within a conical angle of 30º with respect to the major polarization axis of the elliptically polarized laser field is selected to study in the following. The measured KER dependent ion sum momentum spectra along *z* axis (pz_{sum}) of the denitrogenation and deoxygenation channels are displayed in Figs. 4.6(a) and (d), respectively. The red solid curves and blue filled squares in the plots represent the (pz_{sum} integrated) KER spectrum and (KER integrated) pz_{sum} distributions, respectively. Asymmetric distributions of pz_{sum} are observed when the condition of fragment ions N^+ or O^+ flying to $+y$ or $-y$ is applied, which are displayed in Figs. 4.6(b)-(c) and (e)-(f) (blue or red filled squares) for the denitrogenation and deoxygenation channels at different KER ranges, respectively. The asymmetric pz_{sum} spectra of two Coulomb exploded double ionization channels indicate that the N_2O molecule is preferred to be ionized when the laser field points from N to O, which agrees with previous results using a phase-controlled two-color femtosecond laser pulse [196] or a CEP controlled few-cycle laser pulse [197].

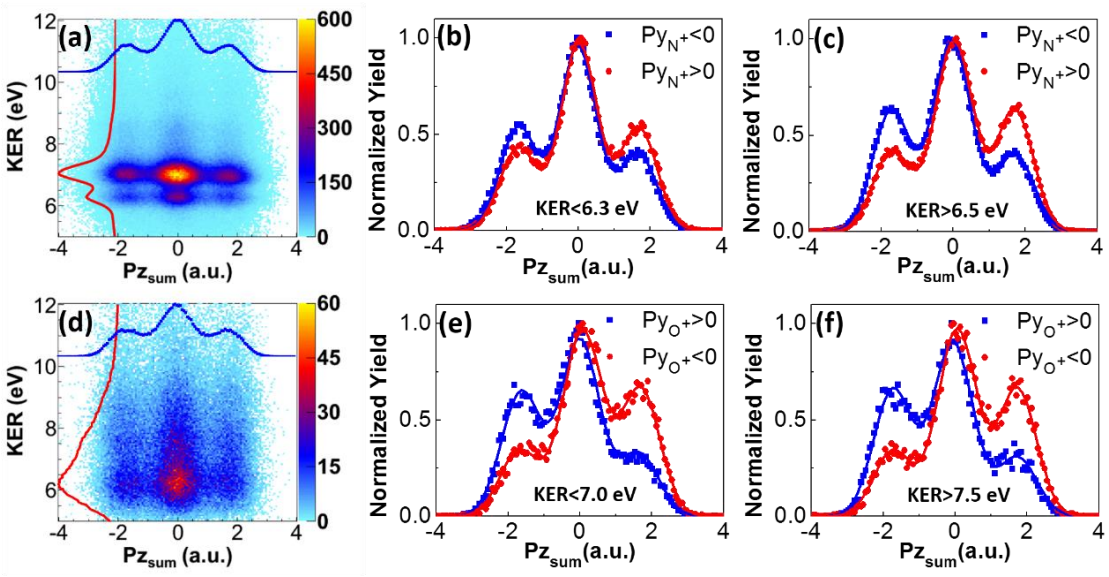

Figure 4. 6 (a), (d) The KER dependent ion sum momentum (pz_{sum}) distributions of the denitrogenation (a) and deoxygenation (d) channels, respectively. (b-c), (e-f) The pz_{sum} distributions integrated over different KER ranges of the denitrogenation (b-c) and deoxygenation (e-f) channels (blue or red filled square) by gating the emission of the fragments N^+ and O^+ to +*y* or -*y* directions, respectively. The blue or red solid curves in (b)-(c) and (e)-(f) represent the fitting curves of the measured data.

To get quantitative insights of the asymmetric dissociative double ionization of N_2O molecules, the ion sum momentum spectra are numerically fitted by considering the convolution of the momenta of two sequentially released electrons, as shown in Figs. 4.6(b)-(c) (denitrogenation channel) and (e)-(f) (deoxygenation channel) (solid curves). The Gaussian distribution of the released electron momentum centered at pz_{ek} is expressed as [75, 91],

$$\frac{A_k}{\sigma_k\sqrt{2\pi}} \times \exp[\frac{-0.5(pz-pz_{ek})^2}{\sigma_k^2}] \quad (4\text{-}1)$$

where k = 1 or 2 represent the first or second electron. The pz_{ek} are the magnitudes of the momentum of the released first (k = 1) or second (k = 2) electrons along *z* direction, reflecting the strength of the laser field at the ionization instants. The convolution of the ion sum momentum is given by,

$$\frac{1}{\sqrt{2\pi}} \sum_{i,j=+,-} \frac{A_{12ij}}{\sigma_{12ij}} \times \exp[\frac{-0.5(pz_{sum}-pz_{sumij})^2}{\sigma_{12ij}^2}] \quad (4\text{-}2)$$

in which $A_{12ij} = A_{1i} \times A_{2j}$, $\sigma_{12ij}^2 = \sigma_{1i}^2 + \sigma_{2j}^2$, and $pz_{sumij} = -(ipz_{e1} + jpz_{e2})$.

For the denitrogenation channel, distinct asymmetries in pz_{sum} spectra are observed for the low KER (< 6.3 eV) and high KER (> 6.5 eV) regions. For the low KER region, the numerical fits return pz_{e1} = 0.82 a.u, pz_{e2} = 0.84 a.u, $A_{1\pm}/A_{1\mp}$ = 1.09, and $A_{2\pm}/A_{2\mp}$ = 1.37. Here $A_{k\pm}$ are the ionized probabilities of the first (k = 1) or second (k = 2) electrons when the laser field vector points to N to O (A_{k+}) or from O to N (A_{k-}), respectively. Therefore the ratio of $A_{k\pm}/A_{k\mp}$ reflect the asymmetry of the ionization of the first (k = 1) or second (k = 2) electrons by the strong laser field vector parallel or anti-parallel to the molecular orientation. For the high KER region, the numerical fit returns pz_{e1} = 0.78 a.u, pz_{e2} = 0.93 a.u, $A_{1\pm}/A_{1\mp}$ = 1.05, and $A_{2\pm}/A_{2\mp}$ = 1.51. However, for the deoxygenation channel, the asymmetry of the pz_{sum} spectra are very similar for different KER ranges. The numerical fits return pz_{e1} = 0.76 a.u, pz_{e2} = 0.93 a.u, $A_{1\pm}/A_{1\mp}$ = 1.02, and $A_{2\pm}/A_{2\mp}$ = 1.97 for the low KER (< 7.0 eV) region, and pz_{e1} = 0.78 a.u, pz_{e2} = 0.95 a.u, $A_{1\pm}/A_{1\mp}$ = 1.02, and $A_{2\pm}/A_{2\mp}$ = 1.98 for the high KER (> 7.5 eV) region.

As discussed before, the profile of the molecular orbital plays important roles in the laser field vector dependent molecular bond breaking. The HOMO and HOMO-1 of N_2O molecule are plotted in Fig. 4.5(c) and the electron density is mainly concentrated around the N atoms, which consistent with the fact that the N_2O molecule is preferred to be ionized when the laser field points from N to O. Meanwhile, the different potential energy of the excited states of N_2O^{2+} have a strong influence on the accessibility of denitrogenation and deoxygenation channels, as shown in Fig. 4.7. The potential energy curves of the lowest states correlated to the denitrogenation channel are very shallow and thus more likely to dissociate as compared to that correlated to the deoxygenation which is preferred to be accessed by higher excited states. It agrees with the observation that the yield of the denitrogenation channel is 5.6 times of the deoxygenation channel. The lowest electronic states $^3\Sigma^-$ and $^1\Delta$ are populated by removing two electrons from HOMO, and the $^3\Pi$ and $^1\Pi$ states are excited by individually removing two electrons from the HOMO and HOMO-1, respectively. Part of the photon ionization created NWP

on the $^3\Sigma^-$ and $^1\Delta$ states have sufficient energy to dissociate to NO^+ and N^+ fragments, forming the high and low KER region of the denitrogenation channel, respectively. For instance, the KER of 7.1eV is expected when the molecule start to dissociate from the equilibrium distance of the molecular bond ($R_{N\text{-}N}$ = 2.09 a.u.) with a potential energy of 35.9 eV on the $^3\Sigma^-$ state with a dissociation limit of 28.8 eV, which agrees well with the measured KER value of 7.0 eV.

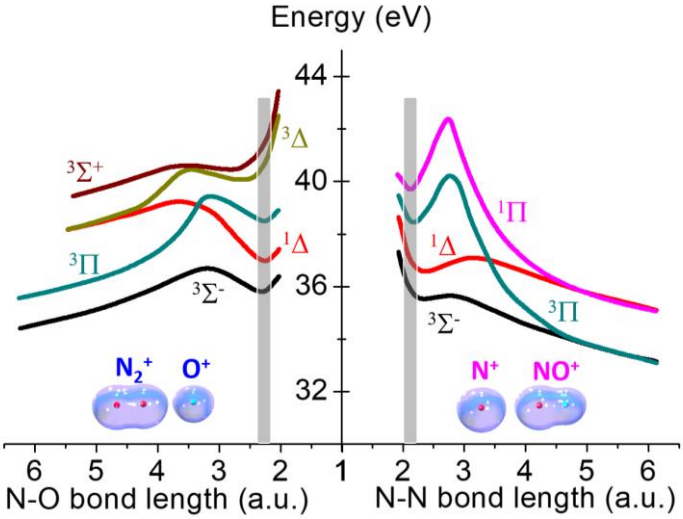

Figure 4. 7 (b) Relevant potential energy curves of the N_2O^{2+}, adopted from [198]. The gray band indicates the Frack-Condon vertical transition range for the photoionization of N_2O molecule.

Although both low and high KER regions in the denitrogenation channel are achieved by removing two electrons from HOMO, their asymmetric degree of pz_{sum} spectra are different. For the low KER region, the strength of drift momenta of the first and second electrons are almost same which indicate they are released by laser fields with similar intensities, i.e., either within a tiny time window or at different time with one in the rising edge and the other in the falling edge of the laser pulse. However, for the high KER region, the drift momentum of the second electron is much larger than that of the first electron, which indicates that the second electron is released by a higher laser field strength.

Since the low KER region is absent in few-cycle laser pulses experiment where the molecular bond cannot be stretched in the time of interaction with laser field [197], we conclude that the first and second electrons are released in the rising and falling edges

of the multicycle laser pulse, respectively. After the first ionization step, the molecular bond is stretched, which rearrange the distribution of the remaining electrons. For instance the mechanism of electron localization assisted enhanced ionization will boost the ionization rate at the critical internuclear distance of the stretched molecule by releasing the electron from the up-field core [84-92]. The released second electron in denitrogenation channel is preferred to be ionized when the laser field points from O to N in the mechanism of electron localization-assisted enhanced ionization, which is opposite to the expected asymmetry governed by the molecular orbital profile. As a result, the observed asymmetry of the low KER region is smaller than that of the high KER region. The N-N bond of the N_2O^+ is stretched after the first ionization and then transited to the $^1\Delta$ state at around $R_{N\text{-}N}$ = 3.2 a.u. and afterwards dissociated with an expected KER of 6.2 eV, which agrees well with the measured value of 6.2 eV. Therefore, it is not just the profile of the molecular orbital, the electron-localization assisted enhanced ionization of stretched molecular ion also plays a role in the laser field vector dependent directional dissociation of molecules.

According to the potential energy curves, the pathway towards the deoxygenation channel is most likely to be achieved by removing one HOMO and one HOMO-1 electrons, and then a NWP is populated on the bound state of N_2O^{2+}, e.g. $^3\Pi$ state. It afterwards is photon-coupled to the different repulsive states (e.g. $^3\Delta$ or $^3\Sigma^+$ states) with different dissociation limits, which leads to a widespread KER spectrum of the deoxygenation channel. The numerical fitting results of the pz_{sum} spectra agree with this expectation, the first electron released from HOMO is almost symmetric with respect to the laser field vector and molecular orientation; while the second electron released from HOMO-1 is preferred when the laser field points from N to O. Meanwhile, the observed border angular momentum distributions of the denitrogenation than that of the deoxygenation in linearly polarized laser field are attributed to the released electrons from different molecular orbitals, e.g. the HOMO and HOMO-1 are four-lobed and bat-

shape respectively, as displayed in Fig. 4.5(c).

4.3 Transient valence charge localization in molecular dissociative ionization

In the molecular bonding theory, the valence electrons are delocalized among the composing atoms, providing the bond thereby stabilizing the system. The inner-shell electrons of individual atoms are, on the other hand, tightly bound to the atoms themselves, which are therefore considered localized. With recent progress in the advanced light sources, probing inner-shell charge (or electron hole) localization of molecule becomes accessible by using the synchrotron radiation [199-204]. However, the transient charge localization upon electron tunneling by an intense femtosecond laser field from a valence molecular shell, which is itself primarily delocalized, has not been observed due to its complicated nature and the associated difficulty in singling out its effect to the system.

The asymmetrical transient valence charge localization in the dissociative single ionization of HCl ($HCl \rightarrow H^+ + Cl + e^-$, denoted as HCl(1,0) channel) is explored by using an intense elliptically polarized near infrared femtosecond laser pulse with duration of 25 fs and central wavelength of 790 nm. The transient charge localization is encoded in the momentum of the outgoing ionic fragments acquired from strong laser field, and the asymmetry is revealed by carefully examining the electron tunneling-site distinguished momentum angular distribution of the ejected H^+ fragment. The peak intensity and ellipticity of laser field are measured to be 3.0×10^{14} W/cm^2 and 0.72, with its major and minor polarization along the *y* and *z* axes, respectively. For the present laser parameters and an ionization potential I_p = 16.6 eV of HOMO-1 of HCl molecule, the Keldysh parameter is calculated to be 0.85, indicating the ionization occurs in the tunneling regime. The LEP or REP (left- or right-handed elliptical polarization) laser fields with the same ellipticity and intensity are produced by rotating a half wave plate

(HWP) in front of a quarter wave plate (QWP) with major axis along the *y* axis, as shown in Fig. 4.8. Switching the helicity of the incident laser pulse every two minutes ensures identical experimental conditions for the LEP and REP laser fields, which allows us to exclude any systematic error from the measurement and cross check the measured results.

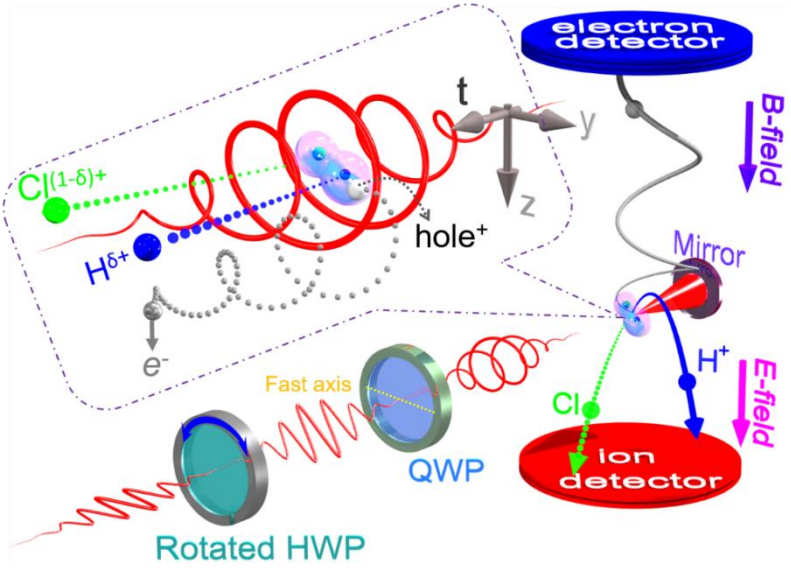

Figure 4. 8 Schematic diagram of the experimental setup. The inset shows schematic traces of the outgoing nuclear fragments and the freed electron. The created hole$^+$, represented by a white ball, is shared by two outgoing nuclear fragments, whose charges evolve as $H^{\delta+}$ and $Cl^{(1-\delta)+}$ with time ($0 \leq \delta \leq 1$).

4.3.1 Recoil momentum of released photoelectron

The momentum conservation in molecular dissociative processes is determined by the center of mass of the ejected electron and nuclear fragments keeping at rest ensured by the neutral state of the parent molecule. While the electron is released from the molecule, the produced ion acquires a momentum via accumulating the impulse from the strong laser field, and can be formulated as,

$$\boldsymbol{p}_{\mathrm{ion}} = \int Z_{\mathrm{ion}}(t)\boldsymbol{E}(t)dt \tag{4-3}$$

where the transient ionic charge $Z_{\mathrm{ion}}(t)$ naturally sets in, with its effect enlarge by the coupling to the laser electric field $\boldsymbol{E}(t)$ and manifest in the obtained momentum $\boldsymbol{p}_{\mathrm{ion}}$. Therefore, the electron tunneling ionization induced asymmetrical transient valence

charge localization is imprinted on the momentum of the outgoing ionic fragments obtained from the strong laser field during the molecular dissociation process.

4.3.2 Asymmetric momentum angular distribution of ejected protons

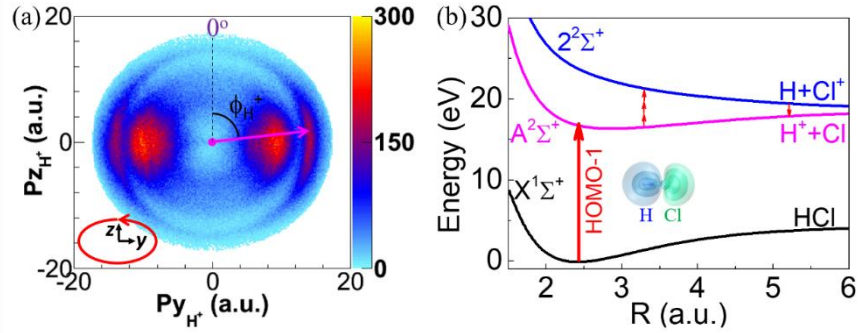

Figure 4. 9 (a) The measured momentum distribution of the H^+ fragment from HCl(1,0) channel. ϕ_{H^+} is the emission angle of H^+ with respect to the +*z* axis. (b) Relevant potential energy curves of HCl and HCl^+, adapted from [194].

Figure 4.9(a) shows the measured momentum distributions of the H^+ fragments of the HCl (1, 0) channel in *y*–*z* plane excited by a LEP laser field, two distinct rings are observed. The H^+ fragments originating from the dissociative single ionization of H_2 in the chamber have almost the same momentum and thus overlap with that of the inner ring of the HCl (1,0) channel. Therefore, only the outer momentum ring is selected to unambiguously represent the HCl(1,0) channel in the following. As illustrated in Fig. 4.9(b), the outer momentum ring of the HCl (1,0) channel is most likely produced in the following approach: by removing one HOMO-1 electron, a NWP is created on the bound $A^2\Sigma^+$ state of HCl^+. It afterwards couples to the repulsive $2^2\Sigma^+$ state via three-photon absorption and then couples back to the $A^2\Sigma^+$ state via one photon emission and dissociates into H^+ and Cl fragments with a final momentum around 14 a.u. for each.

The HCl molecule is favored to be ionized when the molecular bond is aligned along the major polarization axis (*y* axis) of the elliptically polarized laser field, and the final momentum of the released electron or momentum acquired by the ionic fragments from the laser field are mainly along the minor polarization axis (*z* axis). It should be

noted that the radial momentum along the *y* axis of the nuclear fragment is largely caused by the molecular bond breakup. Conversely, the shift or asymmetry in the momentum distribution along the *z* axis is a signature of the momentum of nuclear fragments acquired from the laser field, where the information of transient charge localization is embedded according to Eq. (4-3). As a result, the amount of transient ionic charge of the electron tunneling site dependent can be quantified by analyzing the angular distribution of H^+ in *y*-*z* plane, i.e. ϕ_{H^+} as defined in Fig. 4.9(a).

Figure 4.10(a) displays the measured (open circles) angular distributions of the ejected H^+ fragments from the HCl(1,0) channel driven by a LEP laser field when the correlated photoelectron ends up with a final momentum along +*z* (blue case) or -*z* (orange case) as illustrated in the inset sketches. Taking the orange case as an example, the photoelectron carrying a final momentum along -*z* is released from the -*y* site when the laser electric field vector points to +*y*. The momentum acquired by H^+ (P_{rec}) from the laser field is along +*z* axis governed by the momentum conservation of the molecular system. The measured H^+ with ϕ_{H^+} around -90° (-*y* axis) or +90° (+*y* axis) stands for the cases where the electron is released with the tunneling exit near the H or Cl site, respectively, depending on the orientation of the HCl molecule.

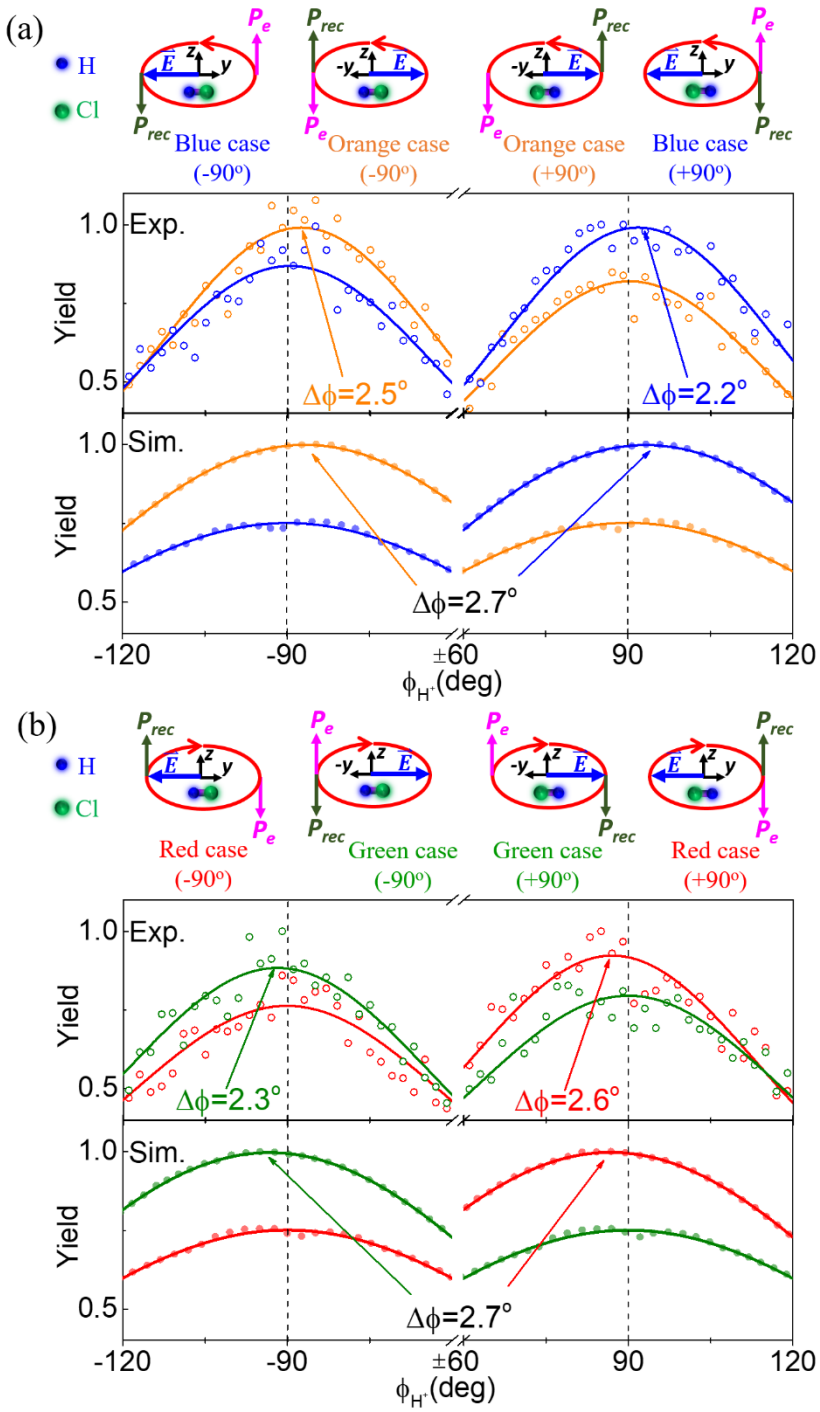

Figure 4. 10 (a) The open circles (Gaussian fitted with solid curves) are measured angular distributions of the H^+ fragments when the electron is released from two different sites driven by the LEP field, as illustrated in the individual sketches. Δϕ is the offset angle of the peak position of the fitted curves with respect to the *y* axis (±90°). The solid circles (fitted with solid curves) are the corresponding classical simulation results. (b) Same to (a) but driven by REP laser field.

Two features can be clearly observed in Fig. 4.10(a) for the orange case. On the one hand, the yield is higher around ϕ_{H^+} = -90° than that around ϕ_{H^+} = +90°, indicating that the electron is preferentially released by laser field vector pointing from H to Cl,

which agree with previous measurements. On the other hand and more interestingly, the angular distribution is asymmetric with respect to the emission direction of ϕ_{H^+} = -90°. Referring to the black dashed line located at ±90° (along the *y* axis), the peak position of the ϕ_{H^+} distribution is clearly right shifted with respect to the -*y* axis (ϕ_{H^+} = -90°), while it is almost symmetrically aligned with the +*y* axis (ϕ_{H^+} = +90°). This asymmetry indicates that the acquisition of momentum from laser field by the ejected H^+ is more efficient when the photoelectron is released with a tunneling exit near the H site of HCl. According to Eq. (4-3), the observed results indicate that there is a fraction of the positive charge that is transiently localized at the H side when the electron is freed with an exit near the H site of HCl; while almost no positive charge is transiently localized around H as the electron is released with an exit near Cl site of HCl.

Likewise, as displayed in Fig. 4.10(a), the momentum acquired by the H^+ fragments from the laser field shows the similar electron tunneling site dependence for the blue case, in which the angular distribution is right-shifted around ϕ_{H^+} = +90° as compared to the symmetric distribution around ϕ_{H^+} = -90°. These features, as shown in Fig. 4.10(b), are also well-reproduced when the helicity of elliptically polarized laser pulses is switched to REP, where the angular distribution of the H^+ is left shifted when the electron is tunneled out with an exit near H site of HCl, i.e. the green case around ϕ_{H^+} = -90° and red case around ϕ_{H^+} = +90°, which enable us to cross check our results and excludes any systematic error from the measurement and data analysis.

4.3.3 Asymmetric transient valence charge localization

The Gaussian fits (solid lines) are performed to the measured data in Figs. 4.10 and obtain the most probable emission direction of ϕ_{H^+m}. In the measurement, the peak strength of momentum of photoelectron in *z* direction is estimated to be 0.8 a.u. and the peak strength of momentum of H^+ fragment along *y* is about 14 a.u., thus the induced rotating angle of H^+ with respect to ϕ_{H^+} = ±90° (*y* axis) should be less than 3.3°. The

measured average offset angle of the H^+ with respect to $\phi_{H^+} = \pm 90°$ is $\Delta\phi = ||\phi_{H^+m}|-90°| = (2.4\pm0.3)°$ when the photoelectron is released with the tunneling exit near the H site of HCl, indicating approximately (72 ± 9)% of the laser field induced momentum is acquired by the H^+ fragment. It is much larger than the value according to the conventional scenario of mass-dominated momentum recoil, where the recoil or laser induced momentum is given to the center-of-mass of the nuclei and merely 1/36 of the momentum will afterwards be deposited to the H^+ fragment, that is why the HCl molecule with a big mass difference between H and Cl is chosen as the target to explore the asymmetric transient valence charge localization.

To support our experimental findings, a classical dynamics simulation of the fragmentation process incorporating a transient charge on the respective fragments is carried out. The results of the classical dynamics simulation, averaged over molecular orientation in the laser polarization plane and intensity variation due to the focal volume effect, are shown in Fig. 4.10 as solid circles and fitted with solid curves. The simulation clearly supports the experimental observation of an asymmetric angular distribution of the ejected H^+ depending on the electron tunneling site. When the electron tunnels out with an exit near H, an initial optical-field-induced transient charge generated by tunneling ionization, which is subject to subsequent rearrangements, is localized at H. Such transient concentration of positive charge on H leads to a substantial laser induced momentum on the H^+ fragment, resulting in an offset angle of 2.7°, close to the experimental value of about 2.4°. On the other hand, when the electron tunnels out from the Cl side of HCl, the optical-field-induced transient charge is initially localized on Cl. Although the positive charge will move to the H side as the dissociation process goes on, substantial concentration of positive charge on H only occurs at the trailing edge of the laser pulse where the laser field strength is low, leading to minimal role in this case. Therefore, it is the initial transient charge localization, when the laser field is on, that plays a crucial role in inducing the asymmetric rotation of the ionic fragments.

4.4 Conclusions

In summary, the electron tunneling site sensitive ultrafast dynamic in molecular dissociative ionization processes were explored. First, the laser field vector dependent dissociative double ionization of the diatomic heteronuclear molecule HCl and more complex triatomic molecule N_2O were studied by employing the angular streaking technique. The instantaneous asymmetry of the molecular bond breaking was revealed by tracing the sum momentum spectra of the ionic fragments. Various pathways involving several excited states created by removing electrons from different molecular orbitals were uncovered. Our results demonstrate that the molecular orientation dependent dissociative double ionization of HCl molecule was mainly governed by the shapes of molecular orbitals, while for more complex molecule N_2O, not only the profiles of molecular orbitals, but also the electron localization-assisted enhanced ionization played an important role.

Second, the asymmetric transient charge localization induced by strong field tunneling ionization, depending on the electron tunneling site in the molecular frame, was observed by tracking the asymmetric momentum distributions of the ionic fragments. When the electron tunneled out with an exit near H which digs a transient hole on this site, as shown in Fig. 4.8, a positive transient charge was localized on H site of HCl, leading to a much larger laser induced momentum on the H^+ fragment. The classical simulation results incorporating a transient charge localization supported our experimental observations. Our work revealed the crucial role of the transient valence charge localization in strong laser field tunneling ionization of molecules and will stimulate extensive investigations of tunneling-site-sensitive correlated electron-nuclear motion in various molecules.

Chapter 5 Molecular alignment and rotational echo stimulated by strong laser fields

In this chapter, the ultrafast rotational dynamics of molecules are explored by using the molecular alignment and the rotational alignment echoes generated by nonresonant intense femtosecond laser pulses. In the first section, the field-free molecular alignment kicked by a linearly polarized intense femtosecond laser pulse are presented. Subsequently, the molecular rotational alignment echoes stimulated by a pair of time delayed linearly polarized laser pulses are described in the section 5.2. Finally, the ultrafast rotational dynamics of asymmetry-top acetone molecule in strong laser fields are investigated based on the molecular alignment, rotational alignment echoes and third-harmonic generations in the section 5.3.

Note that most of the theoretical calculations presented in this chapter have been performed by J.-M. Hartmann, L. H. Coudert, and O. Faucher, the details of theoretical calculations are briefly described.

5.1 Field-free molecular alignment produced by one laser pulse

When exposed to a linearly polarized laser field, the linear molecule such as N_2O or CO_2 can be rapidly aligned to the polarization due to the applied torque on the laser induced dipole moment $\boldsymbol{p}$ ($\boldsymbol{p} = \alpha\boldsymbol{E}$ where α is the polarizability of the molecule and $\boldsymbol{E}$ is the laser field vector). The interaction potential energy is given by $U = -\frac{E^2}{2}(\alpha_\perp + \Delta\alpha\cos^2\theta)$, where θ is the angle between the molecular axis and the laser polarization. The total interaction Hamiltonian is expressed as $H = H_0 - \frac{1}{4}E^2\Delta\alpha\cos^2\theta$, where $H_0 = BJ^2 - DJ^4$ is the rotational Hamiltonian, in which B is the molecular rotational constant and D is the centrifugal distortion constant. The impulsive excitation of several Raman transitions by a femtosecond laser pulse produces a coherent

superposition of rotational Eigenstates, i.e. a rotational wave packet, which free evolution leads to a recurring alternation of alignment and anti-alignment transients called alignment revivals. By solving the time dependent Schrödinger equation [100, 107, 109, 110], the rotational Eigen energies $E = hcBJ(J + 1) - hc[DJ(J + 1)]^2 \approx hcBJ(J + 1)$ and the rotational wave packet $\psi(t) = \sum_{J,M} A_{J,M}(t)e^{-iEt}|J, M>$ are obtained, where h is Planck's constant and $A_{J,M}$ is a complex coefficient which connects the eigenstates . Note that only $\Delta J = 0, \pm 2$ and $\Delta M = 0$ transitions are allowed in nonresonant excitation for linear molecules [100, 106].

The degree of molecular alignment is featured by $\langle\cos^2\theta\rangle = \langle\psi(t)|\cos^2\theta|\psi(t)\rangle$, where $\langle\cos^2\theta\rangle = \frac{1}{3}$ is associated to the isotropic distribution of molecular axes; $\langle\cos^2\theta\rangle > \frac{1}{3}$ indicates that the molecular axes are distributed close to the polarization of the laser field and called alignment; $\langle\cos^2\theta\rangle < \frac{1}{3}$ denotes that the molecular axes are in a plane perpendicular to the laser field and named anti-alignment.

According to the rotational Eigen energies, the rotational period of the alignment revivals is given by $T = 1/(2Bc)$, in which $B = h/(8\pi^2 cI)$ and where I is the molecular moment of inertia [107, 108]. Note that the rotational period is fixed by the rotational constant B which is determined by the intrinsic properties of the molecule. The non-adiabatic alignment is thus interesting since the aligned molecules can be formed under field-free conditions. In this thesis, the molecular alignment refer to the non-adiabatic alignment due to the duration of laser pulse, 100 fs, which is much smaller than the rotational period of the studied molecules, like CO_2, N_2O, C_2H_6, and acetone.

The experimental measurements of the aligned molecules are performed by using a time resolved birefringence balanced detection. As discussed in the chapter 2, the measured signals by the balanced detection are proportional to the induced birefringence Δn and reflect the molecular alignment degree, i.e., $S \propto (\langle\cos^2\theta\rangle - \frac{1}{3})$. Taking the CO_2 molecules at 0.15 bar (room temperature) as an example, stimulated by $Pump_1$ of intensity 12 TW/cm^2, the rotational revivals of molecular alignment are

clearly observed and reproduced well in quantum simulation by solving the time dependent Schrödinger equation, as displayed in Fig. 5.1. Note that the collisional decay of the rotational revivals of CO_2 is weak under the present pressure. As can be see, the molecules align shortly after the interaction with the strong laser pulse at zero time delay. Subsequently, the coherent rotational wavepacket undergoes dephasing and rephasing leading to revivals at *T/2* and *T*, with T = 42.7 ps is the rotational period of CO_2. Moreover, revivals at the fractional periods $T/4$ and $3T/4$ are also observed, attributed to the different statistical weighing factors between the even and odd states of the symmetric molecule, which is determined by the nuclear spin statistics [205, 206]. The relative weight between even and odd J states is 1:0 for CO_2 (O=C=O).

Two features should be noted, first, the measured signal at zero time delay is attributed to both the instantaneous response of bound electrons [207, 208] and the delayed response of molecular alignment. Second, the increased background signal after the zero time delay is caused by the molecular permanent alignment, in which the laser molecule interaction promotes the initial thermal population of rotational states to higher J states but does not change M. Thus the molecules are preferentially excited to $|M| < J$ states for a certain J level [209].

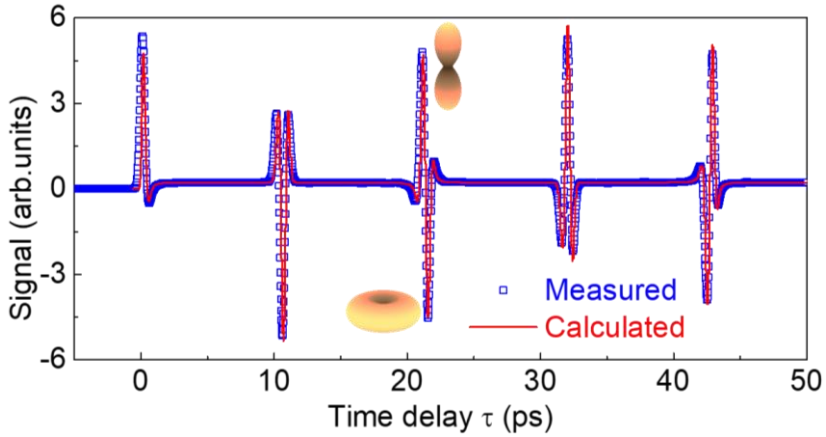

Figure 5. 1 Measured alignment trace of CO_2 molecules and the corresponding quantum simulations performed in collision-free conditions. The 3D pictures illustrate the angular distribution of the molecular axis for aligned and anti-aligned states, respectively.

5.2 Rotational alignment echoes produced by two laser pulses

The molecular rotational alignment echoes can be achieved in gas molecules by using a pair of time delayed nonresonant intense femtosecond laser pulses. Figure 5.2 shows the measured molecular rotational alignment echo trace of N_2O molecules at low pressure (0.2 bar) kicked by $Pump_1$ (13 TW/cm^2) and $Pump_2$ (6 TW/cm^2) with delay τ_{12} = 3.6 ps. As can be seen, the first ultrashort laser pulse ($Pump_1$) creates a superposition of rotational coherences resulting in an alignment. The second ultrashort laser pulse ($Pump_2$), delayed by τ_{12}, is then applied in order to rephase most of the coherences of the system at the time $2\tau_{12}$. As a result, a first echo, second echo, and imaginary echo are produced at 3.6 ps, 7.2 ps, and 13 ps, respectively. In many systems, it is usual to explain the echo phenomenon by invoking the time-reversal mechanism [124], formally, the application of the second pulse reverses the course of time, so that the phase accumulated by the system during the first interval τ_{12} is compensated by the one accumulated during the second interval.

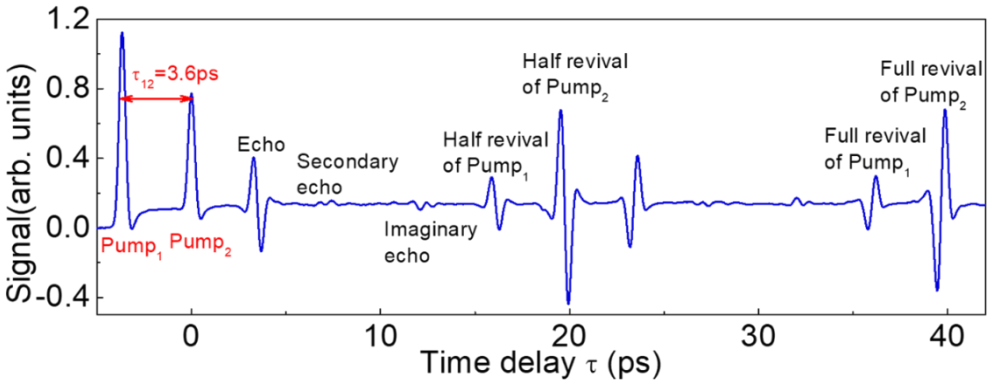

Figure 5. 2 Measured molecular rotational alignment echo trace of N_2O molecules. The first echo is formed at $2\tau_{12}$, with the secondary echo observable at $3\tau_{12}$, and the imaginary echo produced at $T/2$-τ_{12} (equivalent features also appear at times shifted by $T/2$), here, T = 40.4 ps is the molecular rotational period of N_2O.

In addition to rotational alignments echoes, the molecular alignment corresponding to the half and full revivals created by the pumps are observed. In contrast to the molecular rotational alignment revivals whose temporal positions are fixed, the

rotational alignment echoes provide much more flexibility as its time of appearance is adjustable. Therefore, the field-free alignment of molecules can be achieved in a few picoseconds, which is much earlier than the first molecular rotational alignment revival.

5.3 Rotational dynamics of asymmetry-top acetone molecule

In this section, the ultrafast rotational dynamics of asymmetry-top acetone molecules is investigated by using nonresonant intense femtosecond laser pulses. The field-free rotational alignment revivals induced by $Pump_1$ are observed and the weak alignment degree caused by three different reasons are uncovered. The field-free alignment degree is enhanced by employing rotational alignment echoes and fractional rotational alignment echoes are observed for the first time in birefringence measurements. The analysis of the experimental results with numerical simulations based on quantum and classical models allow the determination of the collisional decay time constant of pure acetone in gas phase. Finally, the nonlinear process of third-harmonic generation from a circularly-polarized fundamental laser pulse is demonstrated as an application of aligned acetone molecules.

5.3.1 Molecular symmetry

In the investigation of ultrafast molecular rotational dynamics, the molecules are generally divided into linear, symmetric-top, and asymmetric-top molecules based on the relationship between the three moments of inertia of the molecules (*Ixx*, *Iyy*, and *Izz*), where *x*, *y*, *z* represent the body fixed frame of the molecule [210]:

Ixx = *Iyy* = *Izz* for spherical molecules such as SF_6;

Izz = 0 and *Ixx* = *Iyy* for linear molecules such as CO_2, and N_2O;

Izz < *Iyy* = *Ixx* for prolate symmetric-top molecules such as NH_3, C_2H_6;

Izz = *Iyy* < *Ixx* for oblate symmetric-top molecules such as benzene;

Izz < *Iyy* < *Ixx* for asymmetric-top molecules such as acetone as shown in Fig. 5.3.

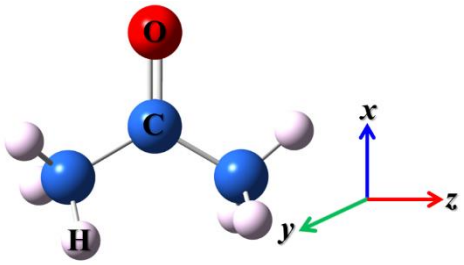

Figure 5. 3 The C_{2v} configuration used in this thesis. The body fixed *xyz* axis system is attached to the molecule using the I^r representation [211]. For clarity its origin is not drawn at the molecular center of mass.

The nonresonant intense femtosecond laser pulse has been successfully demonstrated as a powerful tool to achieve significant field-free alignment of linear molecules thanks to their highly symmetrical structure. However, the achievement of alignment for non-linear molecules is a much more challenging task, especially in the case of asymmetric-top molecules with three nondegenerate moments of inertia (*Ixx*, *Iyy*, and *Izz*). In this case, the complex rotational Hamiltonian is given by $H_0 = AJ_a^2 + BJ_b^2 + CJ_c^2$, where $A = h/(8\pi^2 cIzz)$, $B = h/(8\pi^2 cIxx)$, and $C = h/(8\pi^2 cIyy)$ [155, 212]. As compared to linear molecules, the rotational energy levels of asymmetric-top molecule are irregularly spaced. Moreover, the selection rules for $\Delta J = 0, \pm 1, \pm 2$, $\Delta K = 0, \pm 2$, $\Delta M = 0$, where K and M are the projections of the angular momentum along the molecular z axis and the laboratory Z axis, respectively, are allowed for asymmetric-top molecules [213, 214], leading to a much richer spectrum of excited rotational states than the one achieved for a linear molecule. In the past few years, several works have experimentally and theoretically observed the molecular alignment of near symmetric-top molecules with Ray's parameter $\kappa = (2B-A-C)/(A-C)$ close to ±1 (with $\kappa = -1$ and +1 for prolate and oblate symmetric-top molecules, respectively [215]) such as SO_2 ($\kappa = 0.942$) [155, 216-219] and C_2H_4 ($\kappa = 0.914$) [212, 220].

The field-free alignment of asymmetric-top acetone ($\kappa = 0.37$) gas molecules are more difficult to align than the previous category due to an increased lack of regularity of their rotational spectrum. As shown in Fig. 5.3, the polarizability tensor α is diagonal with components α_{xx}, α_{yy}, and α_{zz} equal to 46.82, 34.16, and 45.63 a_0^3 [221],

respectively. The molecular rotational constants of *A*, *B*, and *C* are 0.339424, 0.283865, and 0.163773 cm^{-1} [222], respectively.

5.3.2 Molecular alignment of acetone

The refractive index difference in gas sample induced by the aligned asymmetry-top acetone molecule is expressed as [212],

$$\Delta n = \frac{3N}{4n_0\varepsilon_0}\sum_{i=x,y,z}[\alpha_{ii}(\langle\Phi_{Zi}^2\rangle - \frac{1}{3})\,] \propto \sum_{i=x,y,z}[\alpha_{ii}(\langle\Phi_{Zi}^2\rangle - \frac{1}{3})\,] \qquad (5\text{-}1)$$

where Φ_{Zi}^2 represents the time evolution of the expectation values of the three direction cosines squared. The measured signal *S* by using the time resolved birefringence balanced detection is given by [219],

$$S \propto \sum_{i=x,y,z}[\alpha_{ii}(\langle\cos^2\theta_{Zi}\rangle - \frac{1}{3})\,] \qquad (5\text{-}2)$$

In order to confirm the intensity of the pump laser pulse and to calibrate the measured signal to Bohr units, first, the measurement of molecular alignment is performed in CO_2 molecules at 0.15 bar exposed to $Pump_1$ of intensity 12 TW/cm^2. The measured and the corresponding collision-free quantum simulation results are displayed in Fig. 5.4. The quantum simulation signal,$S = \sum_{i=x,y,z}[\alpha_{ii}(\langle\Phi_{Zi}^2\rangle - \frac{1}{3})\,]$, is in Bohr units. The measured signal $S \propto \sum_{i=x,y,z}[\alpha_{ii}(\langle\cos^2\theta_{Zi}\rangle - \frac{1}{3})\,]$ is scaled by matching the measured signal to the quantum simulation and finally depicted in Bohr units. The measured rotational revivals of CO_2 molecules are proportional to *I* (intensity of the pump laser field), whereas the molecular permanent alignment scales like I^2. Both are very well reproduced by the quantum model, which confirm the estimated intensity of $Pump_1$.

Next, the measurements and calculations substituting the CO_2 with acetone and keeping the same experimental conditions are performed, as shown in Fig. 5.4. The rotational alignment revivals of acetone at 27 and 54 ps are clearly observed. The weakness of the signal can be explained by three different reasons. First, the laser induced alignment of acetone is relatively inefficient due to its large asymmetry as

compared to the CO_2 molecule. Although the difference between the largest and smallest polarizability components is comparable for both two molecules, the collision-free quantum calculations predict an amplitude of the second revival of acetone about 7 times weaker as compared to the third revival of CO_2, which indicate that the weak alignment efficiency of acetone resulting from its large asymmetry. Alignment revivals is closely linked to the molecules ability to rephase their rotational coherences once stimulated by the pump laser pulse. The incommensurability of the rotational energies of asymmetric-top molecules is reflected in the time domain by quickly decreasing quantum alignment revivals.

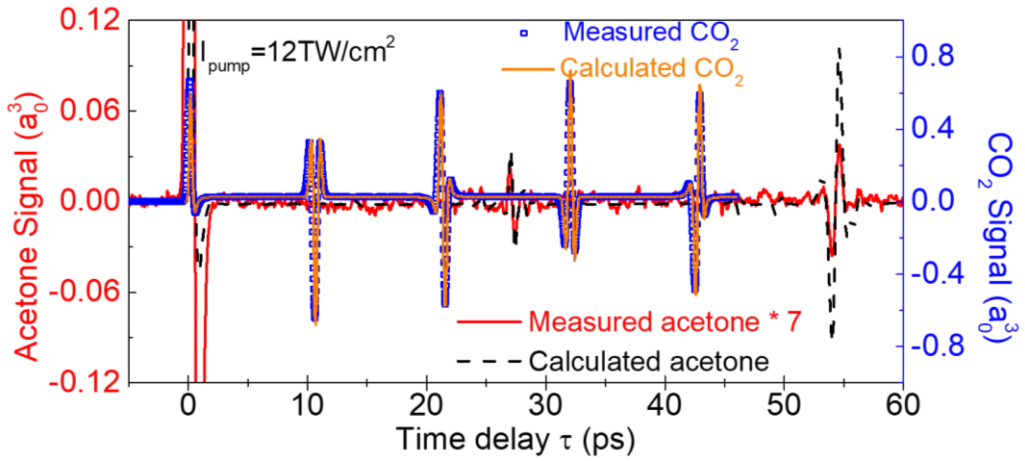

Figure 5. 4 Measured alignment traces of acetone and CO_2 gas at 0.15 bar at room temperature, and the corresponding quantum simulations of acetone and CO_2 performed in collision-free conditions.

Second, the collisional decay time constant τ_R of acetone is small (i.e., the decay rate γ is large) due to the strong and long range dipole-dipole interaction involved in collisions between acetone molecules [223, 224], reducing the amplitude of the revivals that occurred at relatively long time delays. This is evidenced by comparing the amplitudes of the first and second alignment revivals of acetone in both the experiment and the simulation performed in collision free conditions. The collisional decay rate of pure acetone at a given density is estimated by using formula,

$$\gamma = -\frac{1}{\tau_{12}} \ln\left(\frac{R_{exp.}}{R_{th.}}\right) \tag{5-3}$$

in which R is the alignment amplitude ratio of the second to the first alignment revivals in experiment and theory, and τ_{12} defines the time interval between the first and second

revivals. As shown in Fig. 5.5, the collisional decay rates γ for four different gas densities d are measured and fitted by the linear formula $\gamma = \gamma_0 * d$ in order to extract the collisional decay time constant $\tau_R = 1/\gamma_0 = 5.4 \pm 0.4$ ps. amagat. Note that the classical molecular dynamics simulations of 9 ps. amagat is in reasonable agreement with this measured value considering the simplicity of the acetone-acetone potential. The decay time constant of pure acetone is significantly smaller than that of pure CO_2 (about 65 ps. amagat) [154, 156]. Besides mass effects, this is mainly caused by the much longer range and stronger anisotropic forces involved in acetone-acetone collisions [223, 224].

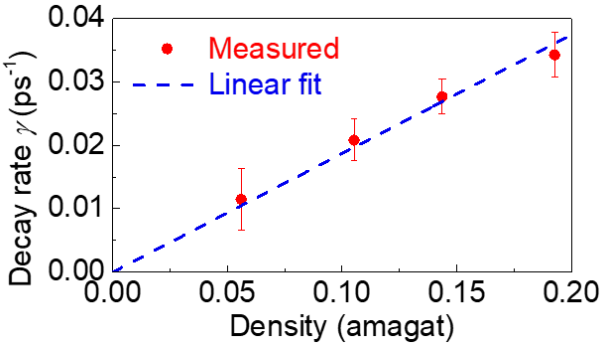

Figure 5. 5 Measured collisional decay rate of the rotational alignment revivals of acetone as a function of the gas density. The density normalized decay time constant is obtained from the linear fit applied to the measured data.

The experimental ratio of the second revival of acetone to the third revival of CO_2 is 121, which is much larger than the value of 29 predicted by the quantum simulations including the measured collisional decay rate. This discrepancy might be attributed to the molecular dissociation induced by the strong pump laser pulse, which is supported by the energy dependence of the alignment signal measured in CO_2 (third revival) and acetone (second revival) under the same experimental conditions, as displayed in Fig. 5.6. The quantum simulations for both molecules show that the amplitude of the revivals is proportional to the intensity of pump laser field in the present energy regime. While this is experimentally confirmed for CO_2, the amplitudes of the revivals of acetone show a clear saturation effect. It is known that the single-photon excitation of the S_1 state of acetone at a wavelength close to 266 nm leads to an efficient C-C

molecular bond broken [225-227]. We believe that the competitive effect, a significant reduction of the ground state population of acetone due to three-photon resonant excitation of the S_1 state by the pump laser at 800 nm, strongly affects the field-free alignment process.

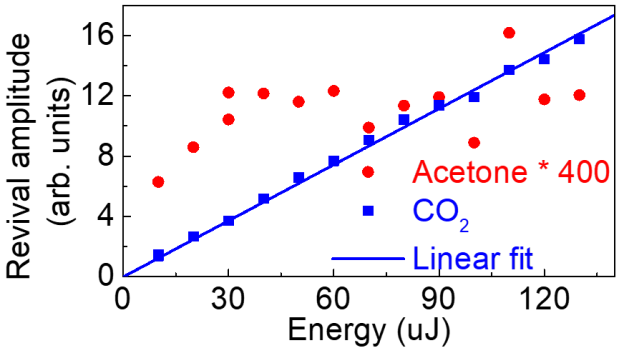

Figure 5. 6 Laser energy dependence of the revivals amplitude of CO_2 and acetone measured under the same experimental conditions (0.15 bar). Linear fit (blue line) of the measured CO_2 revivals.

5.3.3 Rotational alignment echoes of acetone

The rotational alignment echoes by adding $Pump_2$ at time τ_{12} after $Pump_1$ are employed to achieve field-free alignment at shorter time delay. The measured rotational alignment echo traces for τ_{12} at 4.93 and 6.11 ps are shown in Fig. 5.7(a), the gas pressure and the intensity of $Pump_1$ being similar to the previous measurements. Four molecular rotational alignment echoes are clearly observed, the first and the second order alignment echoes generated at τ_{12} and $2\tau_{12}$, respectively, and fractional echoes located at $1/2\tau_{12}$ and $3/2\tau_{12}$ after $Pump_2$. The observed features are well reproduced by both classical and quantum theoretical models for τ_{12} at 4.93 ps in Fig. 5.7(b), which indicates that the rotational alignment echo is a classical phenomenon. As can be seen, the amplitude of the first echo for τ_{12} at 4.93 ps is about twice the amplitude of the second revival observed in the molecular alignment trace shown in Fig. 5.4. Interestingly, fractional echoes have been only observed in linear molecules optically probed through harmonic generations sensitive to higher order $\langle \cos^{2n}\theta \rangle$, $n > 1$ [125]. It is the first time that fractional echoes are observed in a birefringence measurements.

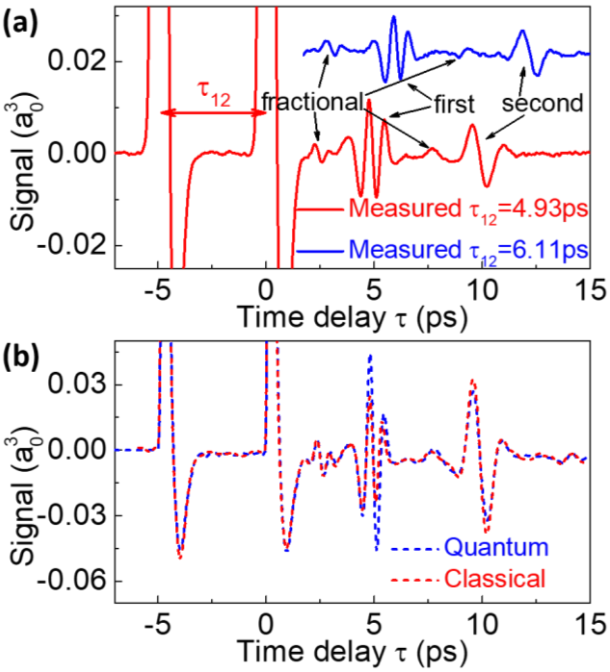

Figure 5. 7 (a) Measured rotational alignment echo traces of acetone gas at 0.15 bar stimulated by $Pump_1$ (12 TW/cm^2) and $Pump_2$ (12 TW/cm^2) with delays τ_{12} at 4.93 and 6.11 ps (upshifted), respectively. The first and second echo, as well as the fractional echoes, are indicated by arrows. (b) Quantum and classical simulation results performed in collision-free condition for τ_{12} at 4.93 ps.

The occurrence of fractional echoes in acetone can be explained from the excitation channel contributing to a rephasing echo. The transitions $J \rightarrow J+1$ and $J+2 \rightarrow J$ with associated Raman frequencies $\omega_{J+1,J} = (B+C)(J+1)$ and $\omega_{J,J+2} = -(B+C)(2J+3)$, respectively, are allowed for asymmetric-top molecules. The pathway to access the rotational alignment echoes involves the excitation of the system by the $Pump_1$ which accumulates a phase $\phi_1 = \omega_{J+1,J} \times \tau_{12}$ at the time where $Pump_2$ interacts with the system. $Pump_2$ formally reverses the course of time with an accumulated phase $\phi_2 = \omega_{J,J+2} \times T$ after a time T. In the high J-limit, $\omega_{J,J+2} \approx -2\omega_{J+1,J}$, which is consistent with a rephasing of the system, $\phi_2 \approx -\phi_1$ at time $T = \tau_{12}/2$ after $Pump_2$ and hence the formation of the fractional echo. In the case of a linear molecule, the fractional echoes are not observed in the birefringence measurements due to the fact that $\Delta J = \pm 1$ transitions are forbidden.

5.3.4 Circularly polarized third-harmonic generation

The third-harmonic generation from a circularly-polarized fundamental laser pulse

is forbidden in randomly oriented gas molecules [228]. However, it has been demonstrated that the third-harmonic generation, as well as high order harmonic generation from a circularly-polarized fundamental laser pulse, can be achieved in aligned molecules [229-231], thanks to the axial symmetry breaking of the molecule + field system. In this thesis, the third-harmonic generation from a circularly-polarized fundamental radiation is observed in aligned acetone molecules achieved by rotational echoes. The experiment setup is described in Fig. 5.8. The wavelength of the probe beam is set to 800 nm and is circularly-polarized. The third-harmonic generation is detected by a photomultiplier tube, combining dichroic mirrors and a band-pass filter in order to remove the fundamental radiations after the interaction region.

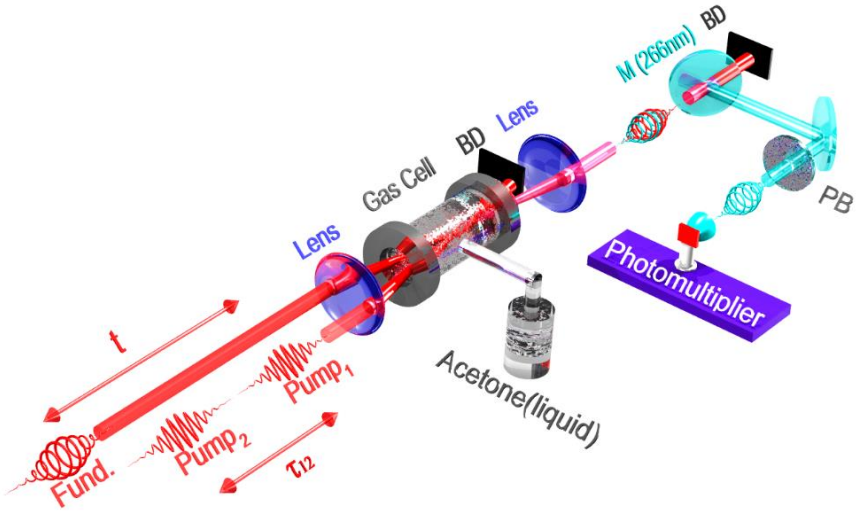

Figure 5. 8 Third-harmonic generation and measurement setup. BD: beam dump, PB: pass-band filter (250-280 nm).

Rotational echo assisted third-harmonic generation at two different delays τ_{12} is displayed in Figs. 5.9. Note that no third-harmonic generation can be detected when the acetone molecule is aligned by one laser pulse. This results from the collisional dissipation that is faster by a factor two for the third-harmonic generation signal, proportional to the intensity of the third-harmonic field, compared to the birefringence signal, proportional to the laser field amplitude. As shown in Figs. 5.9, the rotational alignment echoes allow us to overcome this limitation by aligning the molecule at short time delay. The measured third-harmonic generation signal are very well reproduced

by the quantum and classical simulations, as shown in Figs. 5.9.

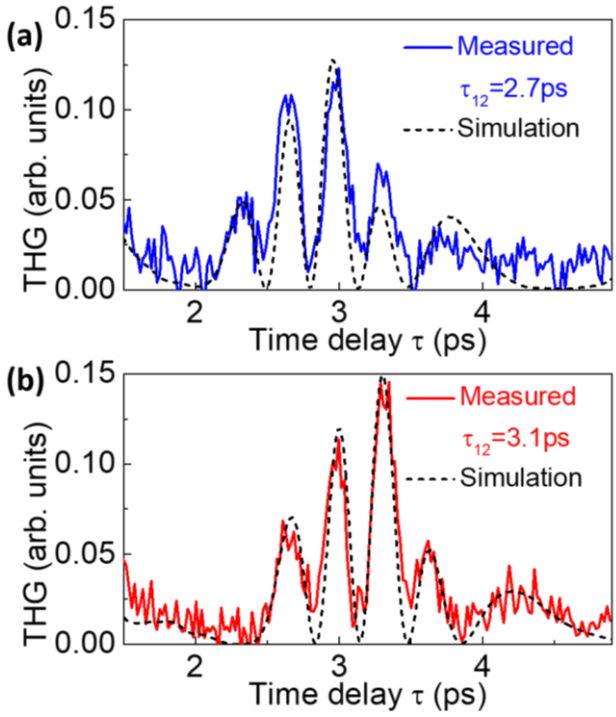

Figure 5. 9 Rotational alignment echo traces observed in the third-harmonic generations of aligned acetone gas at 0.1 bar stimulated by $Pump_1$ and $Pump_2$ with delays at τ_{12} = 2.7 ps (a) and 3.1 ps (b), respectively. The corresponding numerical classical simulations are also displayed. Note that classical and quantum (not shown) results are indistinguishable for the scale of the present figure.

5.4 Conclusions

In this chapter, the ultrafast rotational dynamics of asymmetric-top acetone molecule in gas phase in strong laser field were explored. First, stimulated by a single femtosecond laser pulse, the alignment revivals of acetone were observed. According to the measured and calculated molecular alignment signals, three different reasons were uncovered to explain the weak efficiency of the field-free alignment of acetone: the very small asymmetry parameter of the molecule, the fast collisional dissipation of acetone, and a resonant multiphoton dissociation process competing with the alignment one. Second, the field-free alignment of acetone was improved by employing the rotational echoes stimulated by a pair of time delayed laser pulses. We reported the first observation of fractional alignment echoes by a birefringence detection, which is

attributed to the nonlinearity of the molecule. Among the possible applications, the third-harmonic radiation from a circularly-polarized fundamental laser pulse was generated in a sample of aligned acetone molecules. The experimental findings were fully supported and reproduced by classical molecular dynamics simulations and quantum calculations.

Chapter 6 Ultrafast collisional dissipation probed by rotational alignment echo

The subject of this chapter is the investigation of ultrafast collisional relaxation of rotational molecules in dissipative gas media by using laser induced molecular alignment and rotational alignment echoes. In the first section, the rotational alignment revivals is regarded as a tool to explore the ultrafast collisional dissipation at low gas density (pressure). Subsequently, taking the linear CO_2 and symmetry-top C_2H_6 molecules as research targets, the collisional dissipation at high gas density (pressure) are successfully investigated by using the molecular rotational alignment echoes in the section 6.2 and 6.3 [232, 233]. Finally, in the section 6.4, nonsecular dynamics in collisional processes are uncovered by measuring the decay time constants of molecular rotational alignment echoes at short times [234].

Note that the theoretical calculations in this chapter have been done by J.-M. Hartmann and C. Boulet, which are only briefly described here and more details about classical and quantum simulations can be found in [232-235].

6.1 Collision in low density gas media measured by molecular alignment

In the past few years, the molecular rotational alignment have been successfully employed to investigate the collisional relaxation [115-123]. Taking the N_2O(4%)-He(96%) gas mixture at 2 bar (1.83 amagat, 1 amagat = 2.69×10^{25} molecules/m^3) as an example, the molecular alignment trace of N_2O molecules induced by $Pump_1$ is recorded by probing the transient birefringence of medium and displayed in Fig. 6.1(a). The decreased amplitude of the rotational alignment revivals with increasing the time delay between pump and probe laser pulses, reflecting the collisional relaxation of the

system, is clearly observed. The amplitudes of revivals from peak to dip are fitted by the exponential function $A\exp^{-\frac{1}{\tau_R}\times d\times t} = A\exp^{-\gamma(d)\times t}$, where A defines the amplitude of the signal, t represents the time between the pump and probe, $\gamma(d)$ is the decay rate at gas density d, and τ_R is the density-normalize decay time constant. Generally, the density dependence of $\gamma(d)$ is measured for different gas densities and fitted by a linear law $\gamma(d) = d/\tau_R$ to obtain τ_R. However, this strategy fails at high densities since rotational alignment revivals cannot be observed anymore, as shown in Fig. 6.1(b) for the density at 33.64 amagat (36 bar). Note that the decreased "background" after zero time delay is attributed to the dissipative molecular permanent alignment [117, 154], , which indicates a strong propensity of inelastic collisions to conserve the angular momentum orientation as explained in Sec.1.6. .

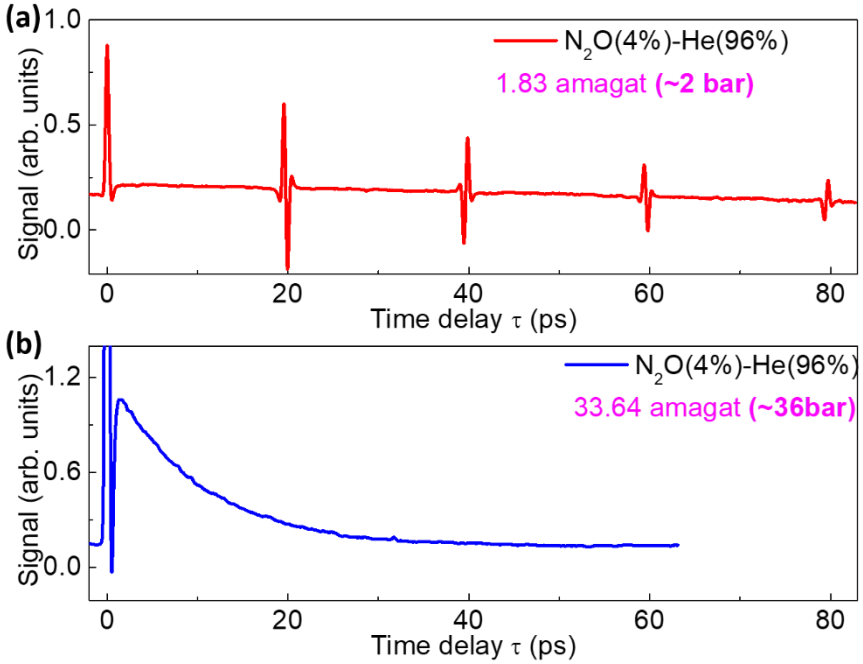

Figure 6. 1 (a) Measured molecular alignment trace of N_2O molecules in N_2O(4%)-He(96%) gas mixtures at 2 bar. (b) Similar to (a) but for 36 bar.

6.2 Echo as a tool to access collisional dissipation in high density media

As mentioned before, the field-free alignment of molecules can be achieved in a few picoseconds by employing the rotational alignment echoes, which is much earlier than the first molecular rotational alignment revival. It can hence be used to probe the

relaxation of the molecule occurring on a very short time scale. Based on the rotational alignment echoes, the ultrafast collisional dissipation of CO_2 molecules in pure gas and mixtures with helium at high pressures are successfully investigated in the few picoseconds [232]. The theoretical predictions, carried using purely classical molecular dynamics simulations (CMDS), reproduce well the observed features.

6.2.1 Optimization of the laser intensity of the second laser pulse

The measured temporal traces of molecular rotational alignment echoes created by two successive nonresonant ultrashort laser pulses ($Pump_1$ of 20 TW/cm^2 and $Pump_2$ of 5 TW/cm^2) in pure CO_2 gas at 0.02 bar for several delay τ_{12} are shown in Fig. 6.2(a). As can be seen, the amplitudes of the alignment echoes (S_{echo}) increase with increasing the time delay between two pumps (τ_{12}) in this weak collision condition. This feature is attributed to the fact that rotational alignment echoes are generated in a multilevel system where the interference between many quantum pathways leads to a partial rephasing of the coherences excited by the first pump laser pulse [128], which explains the maximum echo amplitude depends on the intensity of $Pump_2$ for the fixed delay τ_{12} [232].

A way to limit the experimental biases possibly resulting from the entanglement between $Pump_2$ and τ_{12} is to find a compromised intensity of $Pump_2$ for which S_{echo} varies little over a limited range of τ_{12}. In the experiment, S_{echo} at τ_{12} = 2.4 ps is maximized by adjusting the intensity of $Pump_2$ to 13 TW/cm^2. As shown in Fig. 6.2(b), a series of temporal traces of molecular rotational alignment echoes created by $Pump_1$ of 20 TW/cm^2 and $Pump_2$ of 13 TW/cm^2 are recorded for different τ_{12}, S_{echo} is almost constant with less than 10% variations when τ_{12} is tuned between 1.8 and 3.6 ps. This range of τ_{12} and the intensities of $Pump_1$ and $Pump_2$ are kept to explore the ultrafast collisional dissipation of the rotational CO_2 molecules in pure CO_2 gases and CO_2(4%)-He(96%) gas mixtures at high pressures. The high concentration of helium with large

ionization potential allows overcoming the nonlinear propagation effects that will take place in high density gas.

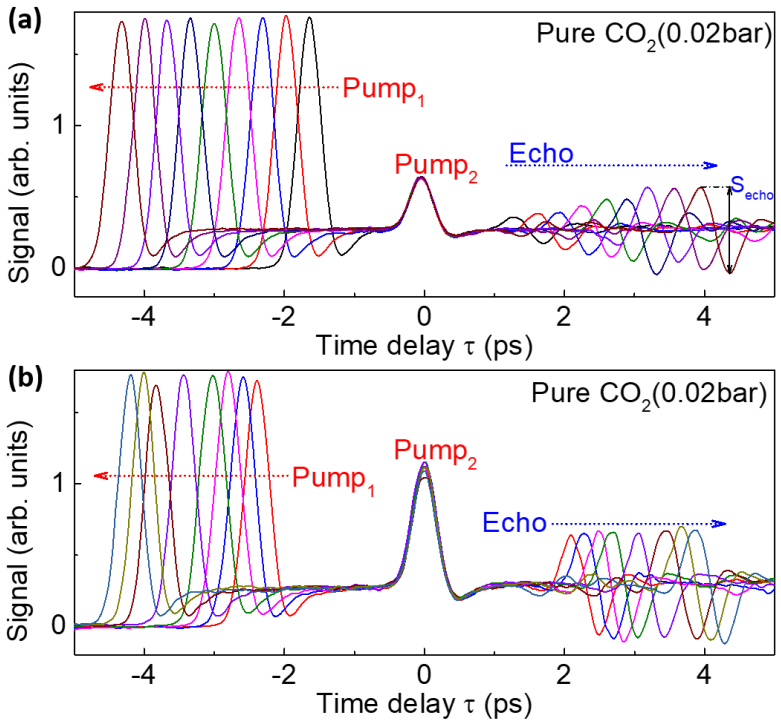

Figure 6. 2 (a) Measured rotational alignment echo traces of CO_2 gas at 0.02 bar stimulated by $Pump_1$ of 20 TW/cm^2 and $Pump_2$ of 5 TW/cm^2 for several delays of τ_{12}. The amplitude S_{echo} is defined as the peak to dip. (b) Similar to (a) but the echo amplitude is optimized by setting $Pump_2$ to 13 TW/cm^2.

6.2.2 Echo traces for different time delays at a given gas density

The measured molecular rotational alignment echo traces of CO_2 molecules in CO_2(4%)-He(96%) gas mixtures at pressure of 43 bar for several delay τ_{12} are shown in Fig. 6.3(a). The decrease of the amplitude of the rotational alignment echoes when increasing the delay between the two pump laser pulses, reflecting the collisional dissipation of the system, are clearly observed. The corresponding S_{echo} are plotted in Fig. 6.3(b), which is fitted by an exponential function $A\exp^{-\gamma(d)\times t}$ for $t = 2\tau_{12}$ and the collisional decay rate $\gamma(d)$is obtained. As can be seen in Fig. 6.3(b), the experimental data and the fitted curve are in good agreement.

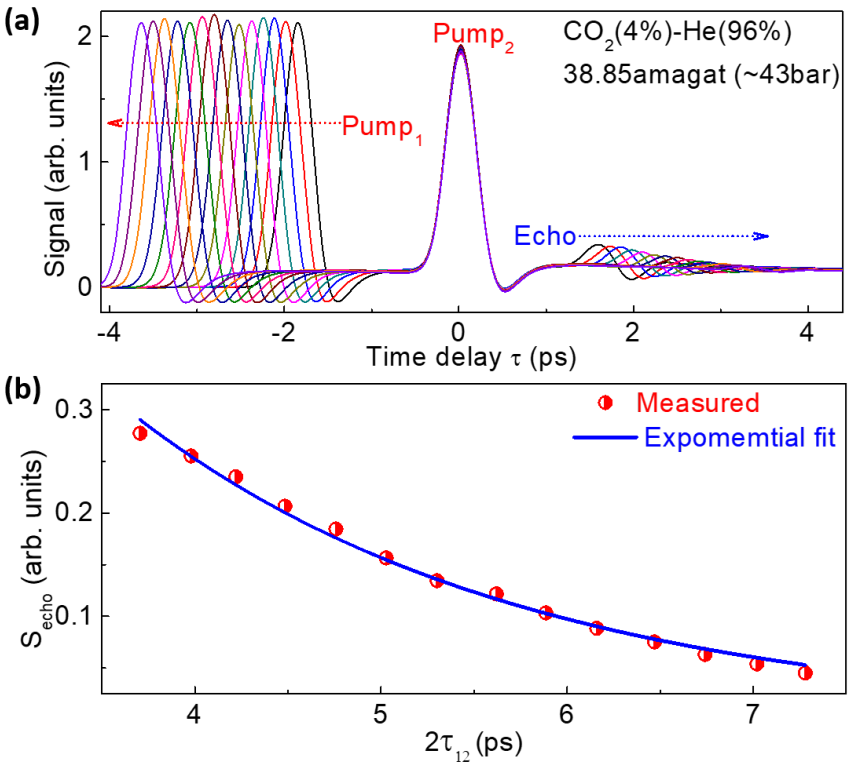

Figure 6. 3 (a) Measured rotational alignment echo traces of CO_2 molecules in CO_2(4%)-He(96%) gas mixtures at 43 bar. (b) Measured S_{echo} extracted from (a) as a function of time delay $2\tau_{12}$, and the exponential fit of the data.

6.2.3 Decay rate of pure CO_2 and CO_2(4%)-He(96%) gas mixture at different densities

The collisional decay rate $\gamma(d)$ of the rotational alignment echoes of CO_2 molecules at different gas densities corresponding to total pressures ranging from 8 to 50 bar are measured and displayed in Fig. 6.4(a). It should be noted that the binary collision mainly occurs in this pressure range, and thus the $\gamma(d)$ should be proportional to the density. The linear fit $\gamma(d) = \gamma_0 * d$ is applied for the measured data and the normalized decay time constant of $\tau_E = \gamma_0^{-1}$ is retrieved and reported in TABLE I. The experimental observation is well reproduced by the classical molecular dynamics simulations [232] as shown in Fig. 6.4(a) and the τ_E predicted by the theory is summarized in TABLE I.

For comparison, the decay time constant of the rotational alignment revivals of CO_2 molecules induced by $Pump_1$ in CO_2(4%)-He(96%) gas mixture is measured at low

pressure. The procedure to extract the related decay time constant is similar to that explained above, the corresponding results are shown in TABLE I. The good match between the experimental values, which are both well reproduced by the classical model, reveal that the decay rates of the rotational alignment revivals and rotational alignment echoes are comparable.

Moreover, the density dependent ultrafast collisional decay rates of rotational CO_2 in pure CO_2 at high gas pressure are measured by employing the rotational alignment echoes and displayed in Fig. 6.4(b), together with the classical simulations. The decay time constant is obtained by applying a linear fit to the measured data and the retrieved results are reported in TABLE I. The decay time constant of rotational alignment revivals of CO_2 in pure CO_2 dense gas is measured at low pressure and summarized in TABLE I. As can be seen, the agreement between classical predictions and measurements agree with each other.

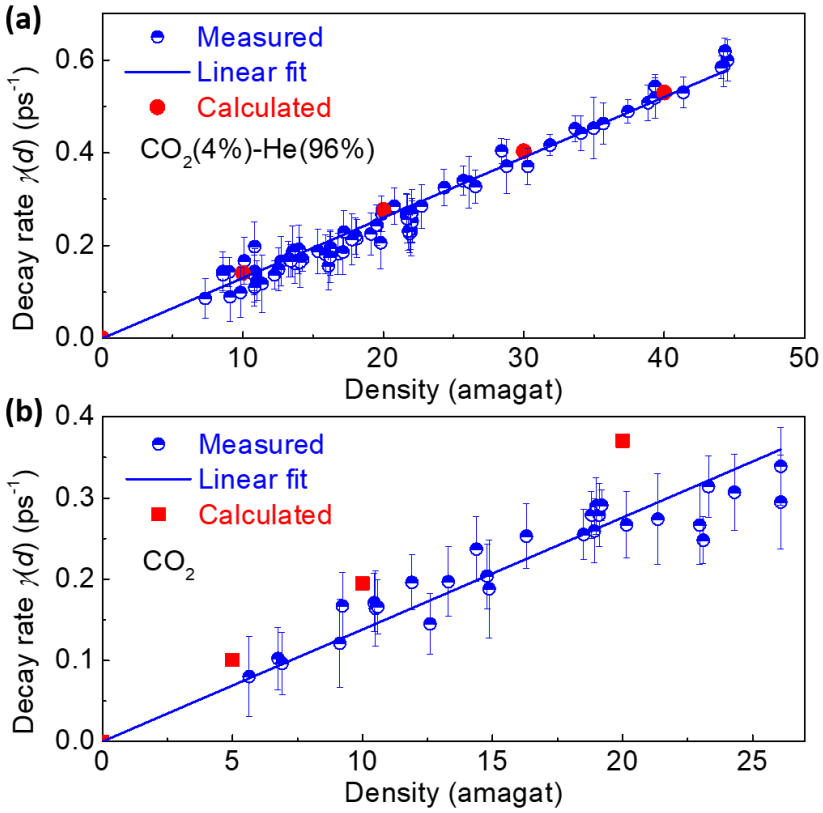

Figure 6. 4 (a) Measured and calculated decay rate *γ(d)* of the rotational alignment echoes as a function of the density of CO_2(4%)-He(96%) gas mixture. A linear fit is applied to the measured data. (b) Same as (a) but for pure CO_2 gas.

TABLE I Measured and calculated normalized collisional decay time constants in ps. amagat units for infinitely diluted CO_2(4%)-He(96%) gas mixture and pure CO_2 gas. For the measured values, the uncertainties correspond to three standard deviations [236].

		Experiment	CMDS model
CO_2(4%)-He(96%)	Revivals	83±8	81.0 [156]
	Echo	77±4	74±7
Pure CO_2	Revivals	68±7	57.0 [156]
	Echo	73±7	53±2

6.3 Collisional dissipation of symmetry-top molecule in high density media

Taking the ethane (C_2H_6) as a prototype, the approach using rotational alignment echoes to study the ultrafast rotational dissipation of symmetric-top molecules in pure gas and mixtures with He at high pressure are investigated in this section.

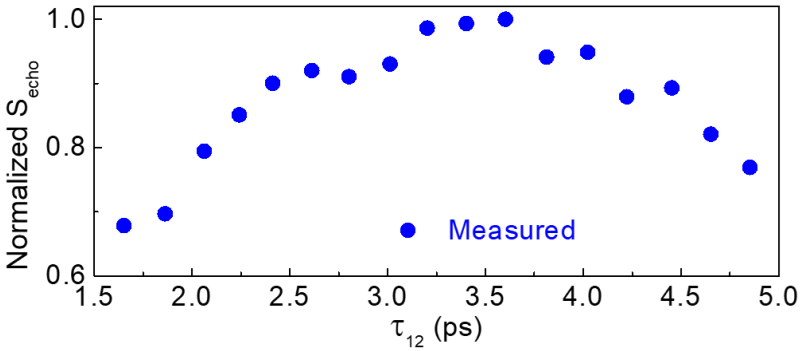

Figure 6. 5 Measured normalized amplitude of the S_{echo} of C_2H_6 in pure C_2H_6 at 0.2 bar for different τ_{12}. The intensities of $Pump_1$ and $Pump_2$ in the measurement are set to 40 and 28 TW/cm^2, respectively.

According to previous studies, a compromised intensity of $Pump_2$ leading to the alignment echo amplitude S_{echo} varies little over a limited range of τ_{12} should be firstly set to. The maximum S_{echo} is optimized for τ_{12} at 3.6 ps by changing the intensity of $Pump_2$ to 28 TW/cm^2 in pure C_2H_6 at 0.2 bar. As shown in Fig. 6.5, the measured S_{echo} are almost constant with less than 10% variations when τ_{12} is tuned from 2.5 to 4.5 ps

under this experimental condition. This range of τ_{12} and the intensities of $Pump_1$ and $Pump_2$ are retained to explore the collisional dissipation of rotationally excited C_2H_6 in pure C_2H_6 gases and C_2H_6(10%)-He(90%) gas mixtures for total pressures up to 14 and 19 bar, respectively.

Figure 6.6(a) presents the measured molecular rotational alignment echo traces of C_2H_6 molecules in C_2H_6(10%)-He(90%) gas mixture at 17 bar (~15.4 amagat) for various τ_{12}. As expected, the collisional dissipation induces the reduction of the strength of rotational alignment echoes with increasing τ_{12}, which is confirmed by the CMDS simulations [233]. Fig. 6.6(b) displays the echo amplitude extracted from Fig. 6.6(a) as a function of $2\tau_{12}$ together the fitted function $A\exp^{-\gamma(d)\times 2\tau_{12}}$ used to extract the value of decay rate $\gamma(d)$.

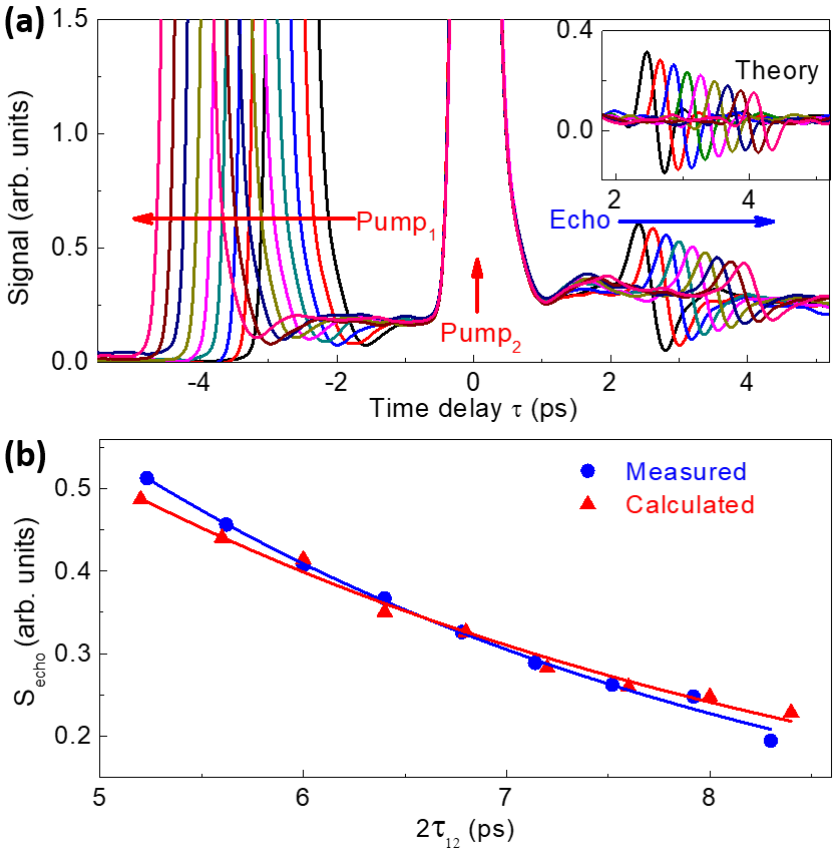

Figure 6. 6 (a) Measured rotational alignment echo traces of C_2H_6 molecules in C_2H_6(10%)-He(90%) gas mixtures at a pressure of 17 bar. The results of CMDS calculations performed in the same experimental conditions are displayed in the inset. (b) Measured and calculated S_{echo} extracted from (a) as a function of $2\tau_{12}$ and the exponential fits of the data.

As displayed in Figs. 6.7(a) and (b), the density dependent $\gamma(d)$ are measured and then fitted by a linear function $\gamma(d) = \gamma_0 * d$ for both C_2H_6(10%)-He(90%) gas mixture and pure C_2H_6, respectively. The decay time constants of the rotational alignment echoes are obtained according to the formula $\tau_E = \gamma_0^{-1}$, and the corresponding results are summarized in TABLE II. For comparison with the experimental data, the calculated decay rates of C_2H_6 in C_2H_6(10%)-He(90%) gas mixture and pure C_2H_6 at different densities are shown in Figs. 6.7(a) and (b) , respectively. The τ_E predicted by the theory is reported in TABLE II.

The decay time constant of the alignment revivals of C_2H_6 molecules are measured in C_2H_6(10%)-He(90%) gas mixtures and pure C_2H_6 gas at low gas pressure. The procedure to extract the decay time constant of rotational alignment revivals is similar to that explained above for the determination of CO_2 molecules, and the results are reported in TABLE II. The classical molecular dynamics simulations reproduce well the observed values [233]. As can be seen, the decay time constant of C_2H_6 in C_2H_6-He gas mixture is larger than that of the pure C_2H_6, indicating that collisions with He induce slower decays, as observed and predicted previously for CO_2 gas. This is caused by the interaction potential of C_2H_6-He (resp. CO_2-He) that is at much shorter range and with much shallower well when compared to the C_2H_6-C_2H_6 (resp. CO_2-CO_2).

Despite the fact that the symmetric-top C_2H_6 molecule has an extra rotational degree of freedom as compared to a linear molecule such as CO_2, the results show that the rotational dissipation of C_2H_6 barely involves more complex collisional relaxation due to characteristics of the C_2H_6-C_2H_6 and C_2H_6-He interactions. Indeed, the C_2H_6-C_2H_6 intermolecular potential is almost insensitive to rotations of the molecules around their C-C bond [237], therefore the collisional dissipation in pure ethane are very close to those occurring in a gas of linear molecules. For C_2H_6 diluted in He, the situation is the same, since the forces applied to the H atoms by a nearby He are very weak as a result of the very shallow H-He potential well [157].

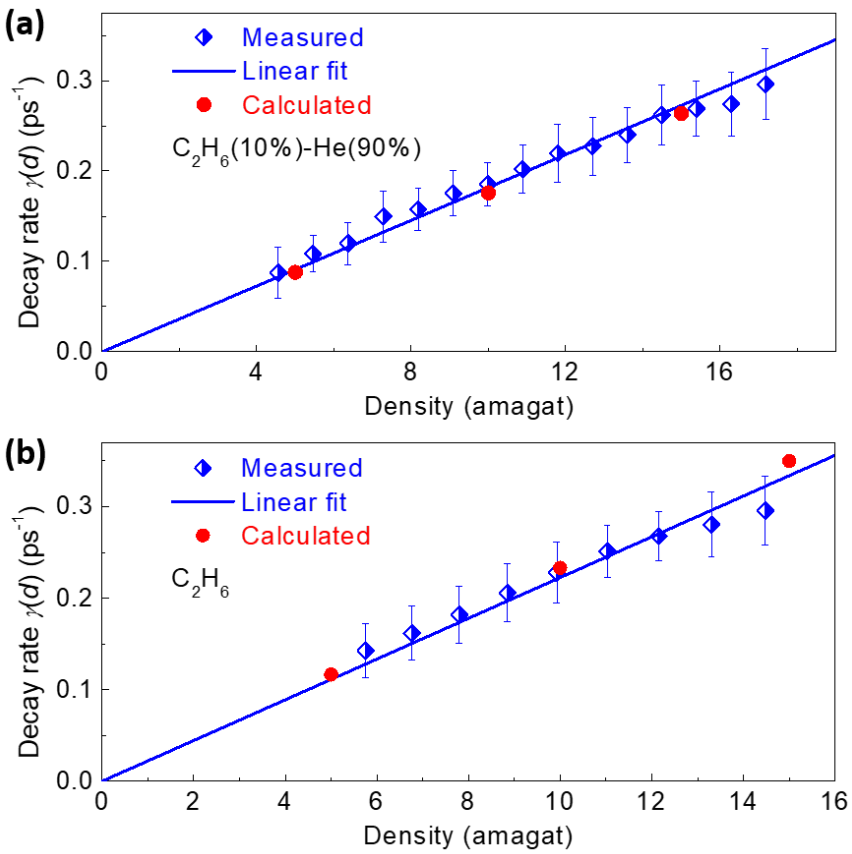

Figure 6. 7 (a) Measured and calculated collisional decay rate $\gamma(d)$ of the rotational alignment echoes as a function of the density of C_2H_6(10%)-He(90%) gas mixture and the linear fit applied to the experimental data. (b) Same as (a) but for pure C_2H_6 gas.

TABLE II Measured and calculated normalized collisional decay time constants in ps. amagat units for infinitely diluted C_2H_6(10%)-He(90%) gas mixture and pure C_2H_6 gas. For the measured values, the uncertainties correspond to two standard deviations [236].

		Experiment	CMDS model
C_2H_6(10%)-He(90%)	Revivals	58.0±9.4	63.0
	Echo	56.3±2.0	59.0
Pure C_2H_6	Revivals	44.7±5.6	44.9 [157]
	Echo	44.9±2.2	42.9

6.4 Nonsecular dynamics in ultrafast collisional processes

Nonsecular effects in collisional decoherence occurring at short time scales (a few

picoseconds) are difficult to track in the experimental measurements due to the observable signals in short time are often hard to access. The molecular rotational alignment echoes stimulated by two successive femtosecond laser pulses are well suited for interrogating the ultrafast dynamics of the system at early times, since its time of appearance can be tuned by adjusting the delay between two pump laser pulses. In this section, taking the thermal collisions induced rotational relaxation of N_2O molecules in N_2O(4%)-He(96%) gas mixture as a research system, the breakdown of the secular approximation is observed. The significant variation of the collisional relaxation of the gas media with the time of appearance of the rotational alignment echoes is clearly observed and well reproduced by the nonsecular quantum master equation [234].

6.4.1 Echo traces at different gas densities for a given time delay

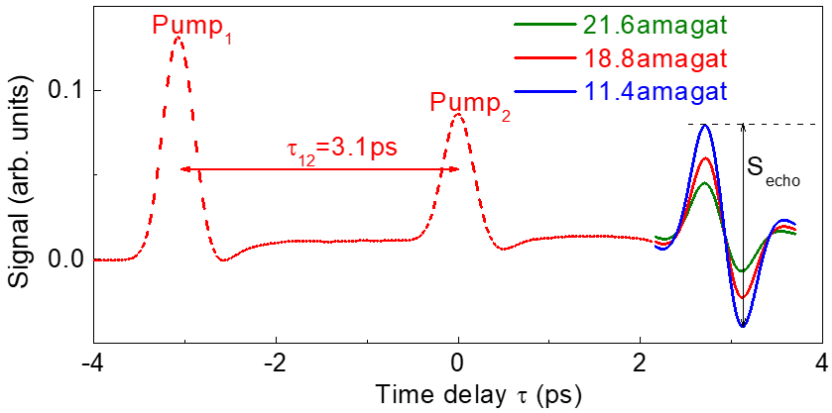

Figure 6. 8 Density-normalized molecular alignment echo traces of N_2O molecules diluted in He at various densities for τ_{12} = 3.1 ps. The intensities of $Pump_1$ and $Pump_2$ are 20 and 13 TW/cm^2, respectively.

The measured density-normalized molecular alignment echo traces of N_2O molecules in N_2O(4%)-He(96%) gas mixture at a fixed delay τ_{12} = 3.1 ps for three different gas densities *d* are recorded and displayed in Fig. 6.8. Note that the density-normalized alignment echo trace is obtained by dividing the measured alignment echo trace by the density *d*, because the measured S_{echo} is proportional to the density, therefore the variation of amplitudes of alignment echoes at different densities is mainly caused by collision. The collision induced decay of the density-normalized amplitudes

of the alignment echoes with increasing density at a fixed τ_{12} are clearly observed in Fig. 6.8, and the density-normalized decay time constant τ_E are obtained by applying a fitting function $A\exp^{-\frac{1}{\tau_E}\times d\times 2\tau_{12}}$ to S_{echo}.

6.4.2 Decay time constant of N_2O(4%)-He(96%) gas mixture at different time delays between the two pump laser pulses

For each delay τ_{12}, the density-normalized alignment echo traces for various gas densities *d* (at least 8 different pressures) are measured and analyzed by using the procedure described above. Note that all traces are measured at high pressure (from 7 to 25 bar) of N_2O(4%)-He(96%) gas mixture. The measured decay time constant τ_E at different time of the appearance of rotational alignment echo, together with the secular and nonsecular quantum simulation results, are shown in Fig. 6.9. The experiments show that the dissipation of the rotational alignment echoes is faster when the delay τ_{12} is large, which is in contrast with the secular model predicting time delay independent results. However, a very good agreement between measurements and calculations is obtained when the nonsecular approximation is employed.

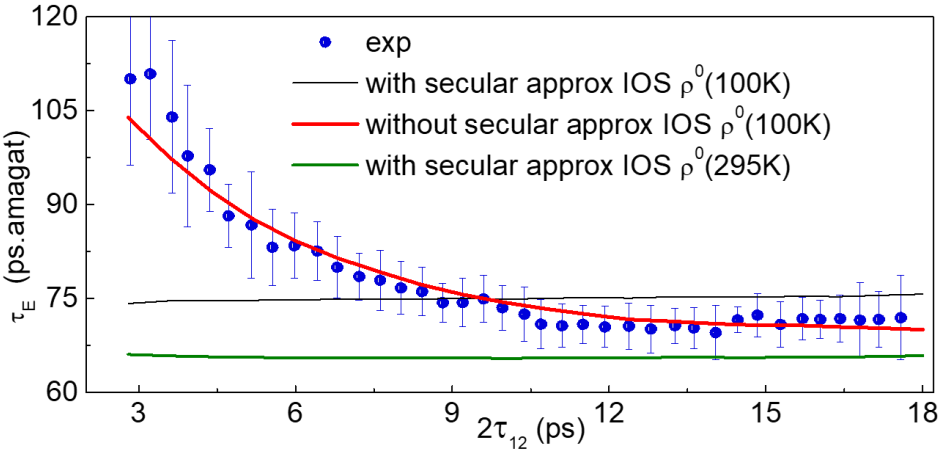

Figure 6. 9 The blue circles with error bars are the measured decay time constants τ_E of the rotational alignment echoes of N_2O molecules in N_2O(4%)-He(96%) gas mixtures at different τ_{12}. The solid lines denote the results of simulations. The green and black solid lines are obtained using the secular approximation with initial N_2O rotational populations corresponding to temperatures of T =100 K and 295 K, respectively. The red solid line represents the results obtained, for populations associated with T = 100 K, using the nonsecular equations.

6.4.3 Nonsecular model and predictions

The quantum simulation of the rotational alignment echo in the presence of collisional dissipation are performed in order to explain the different decoherence dynamics observed at short and long time [234]. Starting from thermal equilibrium before the laser pulses, where the density operator **ρ** is Boltzmannian and diagonal with respect to the rotational quantum numbers *J* and *M*, the evolution of the molecular system after the laser pulse is tracked by the Liouville-von Neumann equation [151, 158, 159],

$$\frac{d\rho(t)}{dt} = -\frac{2\pi\, i}{h}\,[H_0 + H_L(t), \rho(t)] + (\frac{d\rho(t)}{dt})_{coll} \qquad (6\text{-}1)$$

in which H_0 is the free rotational Hamiltonian, and $H_L(t) = -\frac{1}{4}E^2\Delta\alpha\cos^2\theta$ describes the nonresonant interaction of the molecule with the linearly polarized laser field.

In the following, we start with the Markovian approximation which assumes that all collisions are complete and un-correlated [158, 159], i.e., the memory effects associated with collisions that are ongoing at the time of the excitation or at the rotational alignment echo are neglected. This implicitly assumes that the relative number of ongoing collisions is very small and/or that they have an effect over a very short interval of time. For the N_2O(4%)-He(96%) gas mixture system, the N_2O-He accurate *ab initio* intermolecular potential has an almost negligible well [238]. The repulsive front is relevant (i.e., has values between 0 and 600 K) in the [R_0-ΔR, R_0] range of intermolecular distances where R_0 varies between 2.7 and 4.2 Å depending on the respective orientations of the molecular and intermolecular axes and ΔR is typically 0.5 Å. This means that the latter should be in the interval between the two spheres centered on the N_2O center of mass and typical radii 3.0 and 3.5 Å for a N_2O molecule to be colliding with a He atom, which corresponds to a very small volume (about 70 $Å^3$) containing very few He atoms. In addition, the mean relative speed of N_2O-He collisions at room temperature is 1300 $m.s^{-1}$, which indicates that the distance between

the two spheres (0.5 Å) is traveled in 0.038 ps. The above analysis show that non-Markovian effects are very weak in the present study, and the Markovian approximation is thus valid.

Based on a Markovian model of collisions and omitting radiative decays occurring on a much longer time scale, the matrix elements of the dissipation terms are given by,

$$\left(\frac{d\rho_{ij}(t)}{dt}\right)_{coll} = -d\sum_{i',j'}\Lambda_{ij,i'j'}\,\rho_{i'j'}(t) \qquad (6\text{-}2)$$

where *i* and *j* denote the rotational states $|J,M\rangle$ of the system and $\Lambda_{ij,i'j'}$ are the density-normalized relaxation matrix elements.

In the secular approximation, all elements of the relaxation matrix corresponding to transfers among coherences (nondiagonal terms of **ρ**) and between populations (diagonal elements of **ρ**) and coherences are neglected. Only the $\Lambda_{ij,ij}$ and $\Lambda_{ii,i'i'}$ terms are kept which are related to the rates of transfer between $|J,M\rangle$ and $|J',M'\rangle$ states, including inelastic (*J* changing) and elastic reorienting (*J* conserving, *M* changing) processes, as well as the pure dephasing of the coherence which describes the effect of elastic collisions that interrupt the phase of the molecule without quenching it. Therefore, the secular equation driving the decay of the coherences (i.e., for $i \neq j$) becomes,

$$\left(\frac{d\rho_{ij}(t)}{dt}\right)_{coll}^{secular} = -d\,\Lambda_{ij,ij}\,\rho_{ij}(t) \qquad (6\text{-}3)$$

The diagonal elements $\Lambda ij,ij$ have been estimated for N_2O-He at 295 K by using the infinite order sudden approximation (IOSA) [239]. The calculations show that all these terms are positive, practically independent on *i* and *j* and equal to 0.013 ps^{-1}. $amagat^{-1}$, which indicates that the decay time constant in secular approximation is independent on the time delay.

As can be seen by comparing the secular simulations to the experimental results displayed in Fig. 6.9, the agreement is only valid at long time (beyond about $2\tau_{12}$ = 10 ps). This observation seriously questioned the validity of the secular approximation during the early dynamics of the system.

In the nonsecular approximation, all collision induced transfers are involved in the calculation, the equation driving the decay of the coherences becomes,

$$\left(\frac{d\rho_{ij}(t)}{dt}\right)_{coll}^{nonsecular} = \left(\frac{d\rho_{ij}(t)}{dt}\right)_{coll}^{secular} - d\sum_{i',j'\neq i,j}\Lambda_{ij,i'j'}\,\rho_{i'j'}(t) \qquad (6\text{-}4)$$

The required relaxation matrix elements have been constructed by using the IOSA, where the consistency with the rates used previously within the secular approximation is demonstrated [115, 117, 154].

However, the nonsecular calculations at room temperature for *J* values of N_2O up to 60 are not tractable due to the computer limitations. Hence, the conditions of T = 100 K and *J* values up to 38 are carried in the nonsecular calculations. The results of this treatment, in which rates computed at 295 K but initial populations defined at 100 K, are displayed in Fig. 6.9 with a red solid line. Note that comparing the secular results at 100 K and 300 K show that limiting computations to T = 100 K and J_{Max} = 38 only slightly affects the prediction.

As can be seen in Fig. 6.9, the agreement is very satisfactory for the nonsecular simulations and experimental results. It is experimentally and theoretically demonstrate that nonsecular effects resulting from the transfers among coherences as well as between populations and coherences created by the laser pulse reduce the density induced decay of the alignment rotational echo of N_2O molecules in N_2O-He gas mixtures at short times. As time goes by, the transfers between coherences become negligible [234], resulting in a decrease of the decay time constant toward the secular plateau, in perfect agreement with the measurements.

6.5 Conclusions

In this chapter, the ultrafast collisional dynamics of molecules were explored by using molecular rotational alignment echoes.

First, the ultrafast collisional relaxations of linear CO_2 and symmetric-top C_2H_6 molecules in pure and diluted in He were successfully investigated up to a high pressure

range for which alignment revivals were unobservable. The measured decay time constant of the rotational alignment echoes, as that of the quantum alignment revivals, were well reproduced by the classical simulations. Our results indicated that rotational alignment echoes enabled the observation of extremely fast collisional dissipation at a few picosecond timescale for linear and symmetric-top molecules, and potentially in asymmetric-top molecules.

Second, the molecular rotational alignment echoes allowed to track the collision induced ultrafast decoherence of a system very soon after its radiative excitation. The observation of collisional transfers among coherences as well as between populations and coherences occurring in the nonsecular regime and leading to a slowing down of the decoherence of the system lasting for a few picoseconds was uncovered by measuring the time dependent decay time constant of the rotational alignment echoes of N_2O molecules in N_2O-He gas mixtures.

Chapter 7 Summary and Outlook

7.1 Summary

By using intense femtosecond laser pulses and advanced precision measurement techniques, this thesis focused on the laser induced molecular ionization and rotation dynamics. The main contents were summarized below.

1. Dissociative Rydberg excitation of molecule in strong laser field

First, the dissociative frustrated multiple ionization of HCl molecules in intense near infrared femtosecond laser pulses were experimentally observed, in which processes the tunneling ionized electrons were recaptured by the outgoing nuclei of the breaking molecule. The generated excited nuclear fragments, depending on their principle quantum numbers, were directly identified by employing PIPICO spectrum, or singly ionized by the weak DC-field of the spectrometer and be distinguished in the PEPICO spectrum. The similar nuclear KER spectrum of the dissociative Rydberg excitation channel and the corresponding dissociative ionization channel indicated that the electron recapture occurs at the end of the laser pulse.

Second, the multiphoton resonant excitation assisted dissociative Rydberg fragmentation of O_2 molecule in ultraviolet femtosecond laser fields was clearly distinguished in PEPICO spectrum and analyzed by using the electron-nuclear energy correlation. The similar peaks of the sum KER spectrum of the released electron and nuclear fragments were observed in the Rydberg excitation and dissociative single ionization channels. The analyzed results showed that the absorbed photon energy above threshold was mostly deposited to the nuclear fragments in the Rydberg excitation channel. While the released electrons absorbed part of photon energy in the corresponding dissociative ionization channel, resulting in a smaller nuclear kinetic energy as compared the Rydberg excitation channel.

2. Tunneling-site-sensitive ultrafast dynamics of molecule in strong laser field

First, the laser field vector dependent dissociative double ionization of HCl and N_2O molecules were experimentally explored by employing the angular streaking technique. The instantaneous asymmetry of the molecular bond breaking was revealed by gating on the ejected direction of the ionic fragments and tracing their sum momentum spectra. Different pathways towards the dissociative double ionization channels, involving various bound and repulsive electronic states and molecular orbitals, were uncovered. Our results demonstrated that the molecular orientation dependent dissociative double ionization of HCl molecule were mainly governed by the shapes of the molecular orbitals, and for more complex molecule N_2O, the electron localization-assisted enhanced ionization also played an important role.

Second, the strong laser field tunneling ionization induced asymmetric transient valence charge localization was studied in the dissociative single ionization of HCl molecule. The asymmetric transient charge localization, decided by the electron tunneling site in the molecular frame, was encoded in the asymmetric momentum acquired by the outgoing proton fragments from the laser field. By carefully examining the momentum angular distributions of outgoing protons, our results showed that the ejected protons were easier to obtain the momentum from laser field when the photoelectron was released with an exit near the hydrogen site of molecule, which was consistent with the fact that the initial charge was mainly localized on the hydrogen site.

3. Molecular rotational alignment and echo stimulated by strong laser fields

The field-free alignment of acetone gas molecules was successfully achieved in this thesis, which was the most asymmetric-top molecule ever aligned by a femtosecond laser pulse. The weak transient alignment revivals in the measurement was caused by three different reasons: the large asymmetry, the small collisional decay time constant and the multiphoton resonant dissociation of the acetone molecule. The field-free alignment of acetone was improved by employing rotational alignment echoes. As

compared to a linear molecule, fractional echoes were observed in the sensitive birefringence measurement, which was attributed to the nonlinearity of the studied system. Moreover, the third-harmonic radiation from a circularly polarized fundamental laser pulse was generated in aligned acetone molecules.

4. Ultrafast collisional dissipation probed by rotational alignment echo

First, the ultrafast collisional dissipation of linear CO_2 and symmetric-top C_2H_6 molecules in pure and mixture with He at high pressure were successfully studied by employing the molecular rotational alignment echoes in a few picosecond timescale. The reduced strength of the alignment echoes when increasing the time delay between the two pumps at a given density, reflecting the collisional relaxation of the system, were observed. The decay rates at different densities were measured and the decay time constant was obtained by applying a linear fit to the measured decay rates. The measured decay time constant of the rotational alignment echoes in dissipative media were well reproduced by the classical simulations.

Second, the nonsecular dynamics in ultrafast relaxation induced by thermal collisions were successfully revealed in N_2O molecules diluted in helium mixtures by using rotational alignment echoes. The decay time constant of rotational alignment echoes of N_2O molecules at a fixed time delay were determined by measuring the reduction of the amplitude of density-normalized rotational alignment echoes with increasing the gas density. A significant variation of the collisional decay time constant with the time of appearance of the rotational alignment echoes was observed, featuring a decoherence process that was well reproduced by the nonsecular model, which indicated that the transfers among coherences as well as between populations and coherences in the nonsecular regime reduce the decoherence rate of the system during the few first picoseconds of its evolution.

7.2 Outlook

Molecules are one of the basic units of matter, it is of great significance to explore their ionization, excitation, dissociation, and rotation in strong laser field. In present studies, the electron-nucleus correlation provides a new perspective for studying the intramolecular ultrafast processes, and the laser induced field-free molecular alignment is recognized as an important tool for studying the interactions between atoms and/or molecules.

Despite decades of exploration, there are still many interesting phenomenon in the study of molecular dynamics driven by strong lasers, which need to be further explored. For example, on the one hand, the current research on strong laser field induced molecular ionization, excitation, dissociation, and rotation mainly focuses on simple linear molecules. However, most applications in physics and chemistry involve nonlinear molecules with more electronic states, more degrees of freedom of nuclear motion, and more complex electron-nucleus correlation [240, 241]. Based on waveform-controlled ultrafast strong laser pulses and advanced detection technology, the ultrafast dynamics of complex molecular systems will be explored in the future.

On the other hand, in previous research works related to the present studies, most of the studied targets are gaseous molecules, while liquid such as water [242], acetone even liquid nitrogen [243] are rarely explored. Based on ultrafast strong laser pulses and the time resolved birefringence balanced detection, the ultrafast molecular collisional dynamics in liquid systems could be investigated. Moreover, the studies of ultrafast collisional dissipation in this thesis are limited to Markovian systems and it will be also very interesting to explore non-Markovian dynamics.

Bibliography

[1] A. Einstein, Uber einen die Erzeugung and Verwandlung des Lichtes betreffenden heuristischen Gesichtspunkt, Annalen der Physik, **322**, 132 (1905).

[2] T.H. Maiman, Stimulated Optical Radiation in Ruby, Nature, **187**, 493 (1960).

[3] F.J. McClung, R.W. Hellwarth, Giant Optical Pulsations from Ruby, Journal of Applied Physics, **33**, 828 (1962).

[4] L.E. Hargrove, R.L. Fork, M.A. Pollack, Locking of He–Ne Laser modes induced by synchronous intracavity modulation, Applied Physics Letters, **5**, 4 (1964).

[5] A.J. DeMaria, D.A. Stetser, H. Heynau, Self Mode-Locking of Laser with Saturable Absorbers, Applied Physics Letters, **8**, 174 (1966).

[6] R. Fork, B. Greene, C. Shank, Generation of optical pulses shorter than 0.1 psec by colliding pulse mode-locking, IEEE Journal of Quantum Electronics, **17**, 2406 (1981).

[7] D. Strickland, G. Mourou, Compression of amplified chirped optical pulses, Optics Communications, **55**, 447 (1985).

[8] D.E. Spence, P.N. Kean, W. Sibbett, 60-fsec pulse generation from a self-mode-locked Ti:sapphire laser, Opt. Lett., **16**, 42 (1991).

[9] https://www.nobelprize.org/prizes/chemistry/1999/zewail/facts/.

[10] L.V. Keldysh, Ionization in the field of a strong electromagnetic wave, Sov. Phys. JETP, **20**, (1965).

[11] P. Agostini, F. Fabre, G. Mainfray, G. Petite, N.K. Rahman, Free-Free Transitions Following Six-Photon Ionization of Xenon Atoms, Physical review letters, **42**, 1127 (1979).

[12] N.B.D.a.V.P.K. M. V. Ammosov, Tunnel ionization of complex atoms and of atomic ions in an alternating electromagnetic field, Sov. Phys. JETP, **64**, (1986).

[13] M.P. de Boer, H.G. Muller, Observation of large populations in excited states after short-pulse multiphoton ionization, Physical review letters, **68**, 2747 (1992).

[14] R.R. Jones, D.W. Schumacher, P.H. Bucksbaum, Population trapping in Kr and Xe in intense laser fields, Physical Review A, **47**, R49 (1993).

[15] K.C. Kulander, K.J. Schafer, J.L. Krause, Dynamic stabilization of hydrogen in an intense, high-frequency, pulsed laser field, Physical review letters, **66**, 2601 (1991).

[16] A. Talebpour, C.Y. Chien, S.L. Chin, Population trapping in rare gases, Journal of Physics B: Atomic, Molecular and Optical Physics, **29**, 5725 (1996).

[17] E. Wells, I. Ben-Itzhak, R.R. Jones, Ionization of Atoms by the Spatial Gradient of the Pondermotive Potential in a Focused Laser Beam, Physical review letters, **93**, 023001 (2004).

[18] F. Morales, M. Richter, S. Patchkovskii, O. Smirnova, Imaging the Kramers–Henneberger atom, Proceedings of the National Academy of Sciences, **108**, 16906 (2011).

[19] T. Nubbemeyer, K. Gorling, A. Saenz, U. Eichmann, W. Sandner, Strong-Field Tunneling without Ionization, Physical review letters, **101**, 233001 (2008).

[20] K.N. Shomsky, Z.S. Smith, S.L. Haan, Frustrated nonsequential double ionization: A classical model, Physical Review A, **79**, 061402 (2009).

[21] N.I. Shvetsov-Shilovski, S.P. Goreslavski, S.V. Popruzhenko, W. Becker, Capture into rydberg states and momentum distributions of ionized electrons, Laser Physics, **19**, 1550 (2009).

[22] A.S. Landsman, A.N. Pfeiffer, C. Hofmann, M. Smolarski, C. Cirelli, U. Keller, Rydberg state creation by tunnel ionization, New Journal of Physics, **15**, 013001 (2013).

[23] M. Li, L. Qin, C. Wu, L.-Y. Peng, Q. Gong, Y. Liu, Rescattering and frustrated tunneling ionization of atoms in circularly polarized laser fields, Physical Review A, **89**, 013422 (2014).

[24] S. Larimian, S. Erattupuzha, C. Lemell, S. Yoshida, S. Nagele, R. Maurer, A. Baltuška, J. Burgdörfer, M. Kitzler, X. Xie, Coincidence spectroscopy of high-lying Rydberg states produced in strong laser fields, Physical Review A, **94**, 033401 (2016).

[25] Y. Zhao, Y. Zhou, J. Liang, Z. Zeng, Q. Ke, Y. Liu, M. Li, P. Lu, Frustrated tunneling ionization in the elliptically polarized strong laser fields, Opt. Express, **27**, 21689 (2019).

[26] L. Zhao, J. Dong, H. Lv, T. Yang, Y. Lian, M. Jin, H. Xu, D. Ding, S. Hu, J. Chen, Ellipticity dependence of neutral Rydberg excitation of atoms in strong laser fields, Physical Review A, **94**, 053403 (2016).

[27] H. Lv, W. Zuo, L. Zhao, H. Xu, M. Jin, D. Ding, S. Hu, J. Chen, Comparative study on atomic and molecular Rydberg-state excitation in strong infrared laser fields, Physical Review A, **93**, 033415 (2016).

[28] S. Larimian, C. Lemell, V. Stummer, J.-W. Geng, S. Roither, D. Kartashov, L. Zhang, M.-X. Wang, Q. Gong, L.-Y. Peng, S. Yoshida, J. Burgdörfer, A. Baltuška, M. Kitzler, X. Xie, Localizing high-lying Rydberg wave packets with two-color laser fields, Physical Review A, **96**, 021403 (2017).

[29] P.H. Bucksbaum, A. Zavriyev, H.G. Muller, D.W. Schumacher, Softening of the H_2^+ molecular bond in intense laser fields, Physical review letters, **64**, 1883 (1990).

[30] L.J. Frasinski, J.H. Posthumus, J. Plumridge, K. Codling, P.F. Taday, A.J. Langley, Manipulation of Bond Hardening in H_2^+ by Chirping of Intense Femtosecond Laser Pulses, Physical review letters, **83**, 3625 (1999).

[31] A. González-Castrillo, A. Palacios, H. Bachau, F. Martín, Clocking Ultrafast Wave Packet Dynamics in Molecules through UV-Induced Symmetry Breaking, Physical review letters, **108**, 063009 (2012).

[32] K. Lin, X. Gong, Q. Song, Q. Ji, W. Zhang, J. Ma, P. Lu, H. Pan, J. Ding, H. Zeng, J. Wu, Directional bond breaking by polarization-gated two-color ultrashort laser pulses, Journal of Physics B: Atomic, Molecular and Optical Physics, **49**, 025603 (2015).

[33] T. Rathje, A.M. Sayler, S. Zeng, P. Wustelt, H. Figger, B.D. Esry, G.G. Paulus, Coherent Control at Its Most Fundamental: Carrier-Envelope-Phase-Dependent Electron Localization in Photodissociation of a H_2^+ Molecular Ion Beam Target,

Physical review letters, **111**, 093002 (2013).

[34] B. Sheehy, B. Walker, L.F. DiMauro, Phase Control in the Two-Color Photodissociation of HD^+, Physical review letters, **74**, 4799 (1995).

[35] J. McKenna, A.M. Sayler, F. Anis, B. Gaire, N.G. Johnson, E. Parke, J.J. Hua, H. Mashiko, C.M. Nakamura, E. Moon, Z. Chang, K.D. Carnes, B.D. Esry, I. Ben-Itzhak, Enhancing High-Order Above-Threshold Dissociation of H_2^+ Beams with Few-Cycle Laser Pulses, Physical review letters, **100**, 133001 (2008).

[36] H. Ohmura, N. Saito, M. Tachiya, Selective Ionization of Oriented Nonpolar Molecules with Asymmetric Structure by Phase-Controlled Two-Color Laser Fields, Physical review letters, **96**, 173001 (2006).

[37] Q. Song, X. Gong, Q. Ji, K. Lin, H. Pan, J. Ding, H. Zeng, J. Wu, Directional deprotonation ionization of acetylene in asymmetric two-color laser fields, Journal of Physics B: Atomic, Molecular and Optical Physics, **48**, 094007 (2015).

[38] G. Yao, S.-I. Chu, Molecular-bond hardening and dynamics of molecular stabilization and trapping in intense laser pulses, Physical Review A, **48**, 485 (1993).

[39] I. Znakovskaya, P. von den Hoff, G. Marcus, S. Zherebtsov, B. Bergues, X. Gu, Y. Deng, M.J.J. Vrakking, R. Kienberger, F. Krausz, R. de Vivie-Riedle, M.F. Kling, Subcycle Controlled Charge-Directed Reactivity with Few-Cycle Midinfrared Pulses, Physical review letters, **108**, 063002 (2012).

[40] M.F. Kling, C. Siedschlag, A.J. Verhoef, J.I. Khan, M. Schultze, T. Uphues, Y. Ni, M. Uiberacker, M. Drescher, F. Krausz, M.J.J. Vrakking, Control of Electron Localization in Molecular Dissociation, Science, **312**, 246 (2006).

[41] B. Manschwetus, T. Nubbemeyer, K. Gorling, G. Steinmeyer, U. Eichmann, H. Rottke, W. Sandner, Strong Laser Field Fragmentation of H_2: Coulomb Explosion without Double Ionization, Physical review letters, **102**, 113002 (2009).

[42] A. Emmanouilidou, C. Lazarou, A. Staudte, U. Eichmann, Routes to formation of highly excited neutral atoms in the breakup of strongly driven H_2, Physical Review A,

85, 011402 (2012).

[43] H. Price, C. Lazarou, A. Emmanouilidou, Toolkit for semiclassical computations for strongly driven molecules: Frustrated ionization of H_2 driven by elliptical laser fields, Physical Review A, **90**, 053419 (2014).

[44] J. Wu, A. Vredenborg, B. Ulrich, L.P.H. Schmidt, M. Meckel, S. Voss, H. Sann, H. Kim, T. Jahnke, R. Dörner, Multiple Recapture of Electrons in Multiple Ionization of the Argon Dimer by a Strong Laser Field, Physical review letters, **107**, 043003 (2011).

[45] T. Nubbemeyer, U. Eichmann, W. Sandner, Excited neutral atomic fragments in the strong-field dissociation of N_2 molecules, Journal of Physics B: Atomic, Molecular and Optical Physics, **42**, 134010 (2009).

[46] J. McKenna, S. Zeng, J.J. Hua, A.M. Sayler, M. Zohrabi, N.G. Johnson, B. Gaire, K.D. Carnes, B.D. Esry, I. Ben-Itzhak, Frustrated tunneling ionization during laser-induced D_2 fragmentation: Detection of excited metastable D* atoms, Physical Review A, **84**, 043425 (2011).

[47] A. Chen, M.F. Kling, A. Emmanouilidou, Controlling electron-electron correlation in frustrated double ionization of triatomic molecules with orthogonally polarized two-color laser fields, Physical Review A, **96**, 033404 (2017).

[48] A. Chen, H. Price, A. Staudte, A. Emmanouilidou, Frustrated double ionization in two-electron triatomic molecules, Physical Review A, **94**, 043408 (2016).

[49] A. Emmanouilidou, C. Lazarou, Multiple electron trapping in the fragmentation of strongly driven molecules, New Journal of Physics, **14**, 115010 (2012).

[50] G.P. Katsoulis, R. Sarkar, A. Emmanouilidou, Enhancing frustrated double ionization with no electronic correlation in triatomic molecules using counter-rotating two-color circular laser fields, Physical Review A, **101**, 033403 (2020).

[51] X. Xie, C. Wu, H. Liu, M. Li, Y. Deng, Y. Liu, Q. Gong, C. Wu, Tunneling electron recaptured by an atomic ion or a molecular ion, Physical Review A, **88**, 065401 (2013).

[52] H. Hu, S. Larimian, S. Erattupuzha, J. Wen, A. Baltuška, M. Kitzler-Zeiler, X. Xie,

Laser-induced dissociative recombination of carbon dioxide, Physical Review Research, **1**, 033152 (2019).

[53] W. Zhang, X. Gong, H. Li, P. Lu, F. Sun, Q. Ji, K. Lin, J. Ma, H. Li, J. Qiang, F. He, J. Wu, Electron-nuclear correlated multiphoton-route to Rydberg fragments of molecules, Nature Communications, **10**, 757 (2019).

[54] W. Zhang, Z. Yu, X. Gong, J. Wang, P. Lu, H. Li, Q. Song, Q. Ji, K. Lin, J. Ma, H. Li, F. Sun, J. Qiang, H. Zeng, F. He, J. Wu, Visualizing and Steering Dissociative Frustrated Double Ionization of Hydrogen Molecules, Physical review letters, **119**, 253202 (2017).

[55] W. Zhang, P. Lu, X. Gong, H. Li, Q. Ji, K. Lin, J. Ma, H. Li, F. Sun, J. Qiang, F. Chen, J. Tong, J. Wu, Electron trapping in strong-field dissociative frustrated ionization of CO molecules, Physical Review A, **101**, 033401 (2020).

[56] P. Lu, W. Zhang, X. Gong, Q. Song, K. Lin, Q. Ji, J. Ma, F. He, H. Zeng, J. Wu, Electron-nuclear correlation in above-threshold double ionization of molecules, Physical Review A, **95**, 033404 (2017).

[57] C.B. Madsen, F. Anis, L.B. Madsen, B.D. Esry, Multiphoton Above Threshold Effects in Strong-Field Fragmentation, Physical review letters, **109**, 163003 (2012).

[58] R.E.F. Silva, F. Catoire, P. Rivière, H. Bachau, F. Martín, Correlated Electron and Nuclear Dynamics in Strong Field Photoionization of H_2^+, Physical review letters, **110**, 113001 (2013).

[59] Z. Wang, M. Li, Y. Zhou, Y. Li, P. Lan, P. Lu, Counterintuitive energy shifts in joint electron--nuclear-energy spectra of strong-field fragmentation of H_2^+, Physical Review A, **93**, 013418 (2016).

[60] J. Wu, M. Kunitski, M. Pitzer, F. Trinter, L.P.H. Schmidt, T. Jahnke, M. Magrakvelidze, C.B. Madsen, L.B. Madsen, U. Thumm, R. Dörner, Electron-Nuclear Energy Sharing in Above-Threshold Multiphoton Dissociative Ionization of H_2, Physical review letters, **111**, 023002 (2013).

[61] W. Zhang, Z. Li, P. Lu, X. Gong, Q. Song, Q. Ji, K. Lin, J. Ma, F. He, H. Zeng, J. Wu, Photon Energy Deposition in Strong-Field Single Ionization of Multielectron Molecules, Physical review letters, **117**, 103002 (2016).

[62] C. He, H. Liang, M.-M. Liu, L.-Y. Peng, Y. Liu, Laser-wavelength and intensity dependence of electron-nuclear energy sharing in dissociative ionization of H_2, Physical Review A, **101**, 053403 (2020).

[63] W. Zhang, P. Lu, J. Ma, H. Li, X. Gong, J. Wu, Correlated electron–nuclear dynamics of molecules in strong laser fields, Journal of Physics B: Atomic, Molecular and Optical Physics, **53**, 162001 (2020).

[64] X. Sun, M. Li, Y. Shao, M.-M. Liu, X. Xie, Y. Deng, C. Wu, Q. Gong, Y. Liu, Vibrationally resolved electron-nuclear energy sharing in above-threshold multiphoton dissociation of CO, Physical Review A, **94**, 013425 (2016).

[65] Z. Wang, M. Li, Y. Zhou, P. Lan, P. Lu, Correlated electron-nuclear dynamics in above-threshold multiphoton ionization of asymmetric molecule, Scientific Reports, **7**, 42585 (2017).

[66] P. Lu, J. Wang, H. Li, K. Lin, X. Gong, Q. Song, Q. Ji, W. Zhang, J. Ma, H. Li, H. Zeng, F. He, J. Wu, High-order above-threshold dissociation of molecules, Proceedings of the National Academy of Sciences, **115**, 2049 (2018).

[67] H. Li, D. Ray, S. De, I. Znakovskaya, W. Cao, G. Laurent, Z. Wang, M.F. Kling, A.T. Le, C.L. Cocke, Orientation dependence of the ionization of CO and NO in an intense femtosecond two-color laser field, Physical Review A, **84**, 043429 (2011).

[68] M. Abu-samha, L.B. Madsen, Photoelectron angular distributions from polar molecules probed by intense femtosecond lasers, Physical Review A, **82**, 043413 (2010).

[69] D. Dimitrovski, M. Abu-samha, L.B. Madsen, F. Filsinger, G. Meijer, J. Küpper, L. Holmegaard, L. Kalhøj, J.H. Nielsen, H. Stapelfeldt, Ionization of oriented carbonyl sulfide molecules by intense circularly polarized laser pulses, Physical Review A, **83**,

023405 (2011).

[70] D. Dimitrovski, C.P.J. Martiny, L.B. Madsen, Strong-field ionization of polar molecules: Stark-shift-corrected strong-field approximation, Physical Review A, **82**, 053404 (2010).

[71] L. Holmegaard, J.L. Hansen, L. Kalhøj, S. Louise Kragh, H. Stapelfeldt, F. Filsinger, J. Küpper, G. Meijer, D. Dimitrovski, M. Abu-samha, C.P.J. Martiny, L. Bojer Madsen, Photoelectron angular distributions from strong-field ionization of oriented molecules, Nature Physics, **6**, 428 (2010).

[72] D. Pavičić, K.F. Lee, D.M. Rayner, P.B. Corkum, D.M. Villeneuve, Direct Measurement of the Angular Dependence of Ionization for N_2, O_2, and CO_2 in Intense Laser Fields, Physical review letters, **98**, 243001 (2007).

[73] O.I. Tolstikhin, T. Morishita, L.B. Madsen, Theory of tunneling ionization of molecules: Weak-field asymptotics including dipole effects, Physical Review A, **84**, 053423 (2011).

[74] X.M. Tong, Z.X. Zhao, C.D. Lin, Theory of molecular tunneling ionization, Physical Review A, **66**, 033402 (2002).

[75] J. Wu, L.P.H. Schmidt, M. Kunitski, M. Meckel, S. Voss, H. Sann, H. Kim, T. Jahnke, A. Czasch, R. Dörner, Multiorbital Tunneling Ionization of the CO Molecule, Physical review letters, **108**, 183001 (2012).

[76] J. Wu, X. Gong, M. Kunitski, F.K. Amankona-Diawuo, L.P.H. Schmidt, T. Jahnke, A. Czasch, T. Seideman, R. Dörner, Strong Field Multiple Ionization as a Route to Electron Dynamics in a van der Waals Cluster, Physical review letters, **111**, 083003 (2013).

[77] M. Meckel, D. Comtois, D. Zeidler, A. Staudte, D. Pavičić, H.C. Bandulet, H. Pépin, J.C. Kieffer, R. Dörner, D.M. Villeneuve, P.B. Corkum, Laser-Induced Electron Tunneling and Diffraction, Science, **320**, 1478 (2008).

[78] J. Itatani, J. Levesque, D. Zeidler, H. Niikura, H. Pépin, J.C. Kieffer, P.B. Corkum,

D.M. Villeneuve, Tomographic imaging of molecular orbitals, Nature, **432**, 867 (2004).

[79] T. Kanai, S. Minemoto, H. Sakai, Quantum interference during high-order harmonic generation from aligned molecules, Nature, **435**, 470 (2005).

[80] B.K. McFarland, J.P. Farrell, P.H. Bucksbaum, M. Gühr, High Harmonic Generation from Multiple Orbitals in N_2, Science, **322**, 1232 (2008).

[81] R. Torres, N. Kajumba, J.G. Underwood, J.S. Robinson, S. Baker, J.W.G. Tisch, R. de Nalda, W.A. Bryan, R. Velotta, C. Altucci, I.C.E. Turcu, J.P. Marangos, Probing Orbital Structure of Polyatomic Molecules by High-Order Harmonic Generation, Physical review letters, **98**, 203007 (2007).

[82] C. Vozzi, M. Negro, F. Calegari, G. Sansone, M. Nisoli, S. De Silvestri, S. Stagira, Generalized molecular orbital tomography, Nature Physics, **7**, 822 (2011).

[83] I. Bocharova, R. Karimi, E.F. Penka, J.-P. Brichta, P. Lassonde, X. Fu, J.-C. Kieffer, A.D. Bandrauk, I. Litvinyuk, J. Sanderson, F. Légaré, Charge Resonance Enhanced Ionization of CO2 Probed by Laser Coulomb Explosion Imaging, Physical review letters, **107**, 063201 (2011).

[84] S. Bubin, M. Atkinson, K. Varga, X. Xie, S. Roither, D. Kartashov, A. Baltuška, M. Kitzler, Strong laser-pulse-driven ionization and Coulomb explosion of hydrocarbon molecules, Physical Review A, **86**, 043407 (2012).

[85] E. Constant, H. Stapelfeldt, P.B. Corkum, Observation of Enhanced Ionization of Molecular Ions in Intense Laser Fields, Physical review letters, **76**, 4140 (1996).

[86] L.J. Frasinski, K. Codling, P. Hatherly, J. Barr, I.N. Ross, W.T. Toner, Femtosecond dynamics of multielectron dissociative ionization by use of a picosecond laser, Physical review letters, **58**, 2424 (1987).

[87] G.L. Kamta, A.D. Bandrauk, Phase Dependence of Enhanced Ionization in Asymmetric Molecules, Physical review letters, **94**, 203003 (2005).

[88] E. Lötstedt, T. Kato, K. Yamanouchi, Enhanced ionization of acetylene in intense laser fields, Physical Review A, **85**, 041402 (2012).

[89] S. Roither, X. Xie, D. Kartashov, L. Zhang, M. Schöffler, H. Xu, A. Iwasaki, T. Okino, K. Yamanouchi, A. Baltuska, M. Kitzler, High Energy Proton Ejection from Hydrocarbon Molecules Driven by Highly Efficient Field Ionization, Physical review letters, **106**, 163001 (2011).

[90] M. Schmidt, D. Normand, C. Cornaggia, Laser-induced trapping of chlorine molecules with pico- and femtosecond pulses, Physical Review A, **50**, 5037 (1994).

[91] J. Wu, M. Meckel, L.P.H. Schmidt, M. Kunitski, S. Voss, H. Sann, H. Kim, T. Jahnke, A. Czasch, R. Dörner, Probing the tunnelling site of electrons in strong field enhanced ionization of molecules, Nature Communications, **3**, 1113 (2012).

[92] T. Zuo, A.D. Bandrauk, Charge-resonance-enhanced ionization of diatomic molecular ions by intense lasers, Physical Review A, **52**, R2511 (1995).

[93] V. Aquilanti, D. Ascenzi, D. Cappelletti, F. Pirani, Velocity dependence of collisional alignment of oxygen molecules in gaseous expansions, Nature, **371**, 399 (1994).

[94] F. Pirani, D. Cappelletti, M. Bartolomei, V. Aquilanti, M. Scotoni, M. Vescovi, D. Ascenzi, D. Bassi, Orientation of Benzene in Supersonic Expansions, Probed by IR-Laser Absorption and by Molecular Beam Scattering, Physical review letters, **86**, 5035 (2001).

[95] D.P. Pullman, B. Friedrich, D.R. Herschbach, Facile alignment of molecular rotation in supersonic beams, The Journal of chemical physics, **93**, 3224 (1990).

[96] D.A. Baugh, D. Young Kim, V.A. Cho, L.C. Pipes, J.C. Petteway, C.D. Fuglesang, Production of a pure, single ro-vibrational quantum-state molecular beam, Chemical Physics Letters, **219**, 207 (1994).

[97] V.A. Cho, R.B. Bernstein, Tight focusing of beams of polar polyatomic molecules via the electrostatic hexapole lens, The Journal of Physical Chemistry, **95**, 8129 (1991).

[98] B. Friedrich, D.R. Herschbach, Spatial orientation of molecules in strong electric fields and evidence for pendular states, Nature, **353**, 412 (1991).

[99] M. Wu, R.J. Bemish, R.E. Miller, Photodissociation of molecules oriented by dc electric fields: Determining photofragment angular distributions, The Journal of chemical physics, **101**, 9447 (1994).

[100] B. Friedrich, D. Herschbach, Alignment and Trapping of Molecules in Intense Laser Fields, Physical review letters, **74**, 4623 (1995).

[101] Y. Ohshima, H. Hasegawa, Coherent rotational excitation by intense nonresonant laser fields, International Reviews in Physical Chemistry, **29**, 619 (2010).

[102] H. Sakai, C.P. Safvan, J.J. Larsen, K.M. Hilligso/e, K. Hald, H. Stapelfeldt, Controlling the alignment of neutral molecules by a strong laser field, The Journal of chemical physics, **110**, 10235 (1999).

[103] T. Seideman, Rotational excitation and molecular alignment in intense laser fields, The Journal of chemical physics, **103**, 7887 (1995).

[104] H. Stapelfeldt, T. Seideman, Colloquium: Aligning molecules with strong laser pulses, Reviews of Modern Physics, **75**, 543 (2003).

[105] J.G. Underwood, M. Spanner, M.Y. Ivanov, J. Mottershead, B.J. Sussman, A. Stolow, Switched Wave Packets: A Route to Nonperturbative Quantum Control, Physical review letters, **90**, 223001 (2003).

[106] B. Friedrich, D. Herschbach, Polarization of Molecules Induced by Intense Nonresonant Laser Fields, The Journal of Physical Chemistry, **99**, 15686 (1995).

[107] T. Seideman, Revival Structure of Aligned Rotational Wave Packets, Physical review letters, **83**, 4971 (1999).

[108] T. Seideman, On the dynamics of rotationally broad, spatially aligned wave packets, The Journal of chemical physics, **115**, 5965 (2001).

[109] V. Renard, M. Renard, S. Guérin, Y.T. Pashayan, B. Lavorel, O. Faucher, H.R. Jauslin, Postpulse Molecular Alignment Measured by a Weak Field Polarization Technique, Physical review letters, **90**, 153601 (2003).

[110] V. Renard, M. Renard, A. Rouzée, S. Guérin, H.R. Jauslin, B. Lavorel, O. Faucher,

Nonintrusive monitoring and quantitative analysis of strong laser-field-induced impulsive alignment, Physical Review A, **70**, 033420 (2004).

[111] C.B. Madsen, A.S. Mouritzen, T.K. Kjeldsen, L.B. Madsen, Effects of orientation and alignment in high-order harmonic generation and above-threshold ionization, Physical Review A, **76**, 035401 (2007).

[112] R. Velotta, N. Hay, M.B. Mason, M. Castillejo, J.P. Marangos, High-Order Harmonic Generation in Aligned Molecules, Physical review letters, **87**, 183901 (2001).

[113] H. Zhang, C. Jing, J. Yao, G. Li, B. Zeng, W. Chu, J. Ni, H. Xie, H. Xu, S.L. Chin, K. Yamanouchi, Y. Cheng, Z. Xu, Rotational Coherence Encoded in an ``Air-Laser'' Spectrum of Nitrogen Molecular Ions in an Intense Laser Field, Physical Review X, **3**, 041009 (2013).

[114] H. Xu, E. Lötstedt, T. Ando, A. Iwasaki, K. Yamanouchi, Alignment-dependent population inversion in N_2^+ in intense few-cycle laser fields, Physical Review A, **96**, 041401 (2017).

[115] S. Ramakrishna, T. Seideman, Intense Laser Alignment in Dissipative Media as a Route to Solvent Dynamics, Physical review letters, **95**, 113001 (2005).

[116] S. Ramakrishna, T. Seideman, Dissipative dynamics of laser induced nonadiabatic molecular alignment, The Journal of chemical physics, **124**, 034101 (2006).

[117] J.M. Hartmann, C. Boulet, Quantum and classical approaches for rotational relaxation and nonresonant laser alignment of linear molecules: A comparison for CO2 gas in the nonadiabatic regime, The Journal of chemical physics, **136**, 184302 (2012).

[118] N. Owschimikow, F. Königsmann, J. Maurer, P. Giese, A. Ott, B. Schmidt, N. Schwentner, Cross sections for rotational decoherence of perturbed nitrogen measured via decay of laser-induced alignment, The Journal of chemical physics, **133**, 044311 (2010).

[119] T. Vieillard, F. Chaussard, D. Sugny, B. Lavorel, O. Faucher, Field-free molecular

alignment of CO_2 mixtures in presence of collisional relaxation, Journal of Raman Spectroscopy, **39**, 694 (2008).

[120] S. Ramakrishna, T. Seideman, Coherence spectroscopy in dissipative media: A Liouville space pathway approach, The Journal of chemical physics, **122**, 084502 (2005).

[121] A. Pelzer, S. Ramakrishna, T. Seideman, Optimal control of molecular alignment in dissipative media, The Journal of chemical physics, **126**, 034503 (2007).

[122] A. Pelzer, S. Ramakrishna, T. Seideman, Optimal control of rotational motions in dissipative media, The Journal of chemical physics, **129**, 134301 (2008).

[123] B. Shepperson, A.S. Chatterley, L. Christiansen, A.A. Søndergaard, H. Stapelfeldt, Observation of rotational revivals for iodine molecules in helium droplets using a near-adiabatic laser pulse, Physical Review A, **97**, 013427 (2018).

[124] G. Karras, E. Hertz, F. Billard, B. Lavorel, J.M. Hartmann, O. Faucher, E. Gershnabel, Y. Prior, I.S. Averbukh, Orientation and Alignment Echoes, Physical review letters, **114**, 153601 (2015).

[125] G. Karras, E. Hertz, F. Billard, B. Lavorel, G. Siour, J.M. Hartmann, O. Faucher, E. Gershnabel, Y. Prior, I.S. Averbukh, Experimental observation of fractional echoes, Physical Review A, **94**, 033404 (2016).

[126] K. Lin, P. Lu, J. Ma, X. Gong, Q. Song, Q. Ji, W. Zhang, H. Zeng, J. Wu, G. Karras, G. Siour, J.-M. Hartmann, O. Faucher, E. Gershnabel, Y. Prior, I.S. Averbukh, Echoes in Space and Time, Physical Review X, **6**, 041056 (2016).

[127] J. Lu, Y. Zhang, H.Y. Hwang, B.K. Ofori-Okai, S. Fleischer, K.A. Nelson, Nonlinear two-dimensional terahertz photon echo and rotational spectroscopy in the gas phase, Proceedings of the National Academy of Sciences, **113**, 11800 (2016).

[128] D. Rosenberg, R. Damari, S. Fleischer, Echo Spectroscopy in Multilevel Quantum-Mechanical Rotors, Physical review letters, **121**, 234101 (2018).

[129] D. Rosenberg, R. Damari, S. Kallush, S. Fleischer, Rotational Echoes: Rephasing

of Centrifugal Distortion in Laser-Induced Molecular Alignment, The Journal of Physical Chemistry Letters, **8**, 5128 (2017).

[130] D. Rosenberg, S. Fleischer, Intrinsic calibration of laser-induced molecular alignment using rotational echoes, Physical Review Research, **2**, 023351 (2020).

[131] B. Wang, L. He, Y. He, Y. Zhang, R. Shao, P. Lan, P. Lu, All-optical measurement of high-order fractional molecular echoes by high-order harmonic generation, Opt. Express, **27**, 30172 (2019).

[132] L. Xu, I. Tutunnikov, L. Zhou, K. Lin, J. Qiang, P. Lu, Y. Prior, I.S. Averbukh, J. Wu, Echoes in unidirectionally rotating molecules, Physical Review A, **102**, 043116 (2020).

[133] I.S. Averbukh, N.F. Perelman, Fractional revivals: Universality in the long-term evolution of quantum wave packets beyond the correspondence principle dynamics, Physics Letters A, **139**, 449 (1989).

[134] J. Ortigoso, M. Rodríguez, M. Gupta, B. Friedrich, Time evolution of pendular states created by the interaction of molecular polarizability with a pulsed nonresonant laser field, The Journal of chemical physics, **110**, 3870 (1999).

[135] F. Rosca-Pruna, M.J.J. Vrakking, Experimental Observation of Revival Structures in Picosecond Laser-Induced Alignment of I_2, Physical review letters, **87**, 153902 (2001).

[136] N. Xu, C. Wu, J. Huang, Z. Wu, Q. Liang, H. Yang, Q. Gong, Field-free alignment of molecules at room temperature, Opt. Express, **14**, 4992 (2006).

[137] K. Yoshii, G. Miyaji, K. Miyazaki, Measurement of molecular rotational temperature in a supersonic gas jet with high-order harmonic generation, Opt. Lett., **34**, 1651 (2009).

[138] I.S. Averbukh, R. Arvieu, Angular Focusing, Squeezing, and Rainbow Formation in a Strongly Driven Quantum Rotor, Physical review letters, **87**, 163601 (2001).

[139] M. Leibscher, I.S. Averbukh, H. Rabitz, Molecular Alignment by Trains of Short

Laser Pulses, Physical review letters, **90**, 213001 (2003).

[140] E.L. Hahn, Spin Echoes, Physical Review, **80**, 580 (1950).

[141] N.A. Kurnit, I.D. Abella, S.R. Hartmann, Observation of a Photon Echo, Physical review letters, **13**, 567 (1964).

[142] R.W. Gould, T.M. O'Neil, J.H. Malmberg, Plasma Wave Echo, Physical review letters, **19**, 219 (1967).

[143] A. Bulatov, A. Kuklov, B.E. Vugmeister, H. Rabitz, Echo in optical lattices: Stimulated revival of breathing oscillations, Physical Review A, **57**, 3788 (1998).

[144] M. Herrera, T.M. Antonsen, E. Ott, S. Fishman, Echoes and revival echoes in systems of anharmonically confined atoms, Physical Review A, **86**, 023613 (2012).

[145] L.K. Spentzouris, J.F. Ostiguy, P.L. Colestock, Direct Measurement of Diffusion Rates in High Energy Synchrotrons Using Longitudinal Beam Echoes, Physical review letters, **76**, 620 (1996).

[146] R.W. Brown, Y.-C. N. Cheng, E. M. Haacke, M. R.Thompson, a.R. Venkatesan, Magnetic Resonance Imaging: Physical Principles and Sequence Design (Wiley-Blackwell, New York, 2014). 2014.

[147] E. Hemsing, G. Stupakov, D. Xiang, A. Zholents, Beam by design: Laser manipulation of electrons in modern accelerators, Reviews of Modern Physics, **86**, 897 (2014).

[148] G. Stupakov, Using the Beam-Echo Effect for Generation of Short-Wavelength Radiation, Physical review letters, **102**, 074801 (2009).

[149] D. Xiang, E. Colby, M. Dunning, S. Gilevich, C. Hast, K. Jobe, D. McCormick, J. Nelson, T.O. Raubenheimer, K. Soong, G. Stupakov, Z. Szalata, D. Walz, S. Weathersby, M. Woodley, P.L. Pernet, Demonstration of the Echo-Enabled Harmonic Generation Technique for Short-Wavelength Seeded Free Electron Lasers, Physical review letters, **105**, 114801 (2010).

[150] Z.T. Zhao, D. Wang, J.H. Chen, Z.H. Chen, H.X. Deng, J.G. Ding, C. Feng, Q.

Gu, M.M. Huang, T.H. Lan, Y.B. Leng, D.G. Li, G.Q. Lin, B. Liu, E. Prat, X.T. Wang, Z.S. Wang, K.R. Ye, L.Y. Yu, H.O. Zhang, J.Q. Zhang, M. Zhang, M. Zhang, T. Zhang, S.P. Zhong, Q.G. Zhou, First lasing of an echo-enabled harmonic generation free-electron laser, Nature Photonics, **6**, 360 (2012).

[151] V. May, O. Kuhn, Charge and Energy Transfer Dynamics in Molecular Systems, 2011.

[152] J.O. Hirschfelder, C.F. Curtiss, R.B. Bird, Molecular Theory of Gases and Liquids, 1964.

[153] H. Zhang, F. Billard, X. Yu, O. Faucher, B. Lavorel, Dissipation dynamics of field-free molecular alignment for symmetric-top molecules: Ethane (C2H6), The Journal of chemical physics, **148**, 124303 (2018).

[154] T. Vieillard, F. Chaussard, F. Billard, D. Sugny, O. Faucher, S. Ivanov, J.M. Hartmann, C. Boulet, B. Lavorel, Field-free molecular alignment for probing collisional relaxation dynamics, Physical Review A, **87**, 023409 (2013).

[155] I.F. Tenney, M. Artamonov, T. Seideman, P.H. Bucksbaum, Collisional decoherence and rotational quasirevivals in asymmetric-top molecules, Physical Review A, **93**, 013421 (2016).

[156] J.M. Hartmann, C. Boulet, T. Vieillard, F. Chaussard, F. Billard, O. Faucher, B. Lavorel, Dissipation of alignment in CO_2 gas: A comparison between ab initio predictions and experiments, The Journal of chemical physics, **139**, 024306 (2013).

[157] J.M. Hartmann, C. Boulet, H. Zhang, F. Billard, O. Faucher, B. Lavorel, Collisional dissipation of the laser-induced alignment of ethane gas: A requantized classical model, The Journal of chemical physics, **149**, 154301 (2018).

[158] J. Bretón, A. Hardisson, F. Mauricio, S. Velasco, Relaxation of quantum systems weakly coupled to a bath. I. Total-time-ordering-cumulant and partial-time-ordering-cumulant non-Markovian theories, Physical Review A, **30**, 542 (1984).

[159] R. Kosloff, Quantum thermodynamics and open-systems modeling, The Journal

of chemical physics, **150**, 204105 (2019).

[160] B.A. Stickler, B. Schrinski, K. Hornberger, Rotational Friction and Diffusion of Quantum Rotors, Physical review letters, **121**, 040401 (2018).

[161] K. Walter, B.A. Stickler, K. Hornberger, Collisional decoherence of polar molecules, Physical Review A, **93**, 063612 (2016).

[162] D.J. Jones, S.A. Diddams, J.K. Ranka, A. Stentz, R.S. Windeler, J.L. Hall, S.T. Cundiff, Carrier-Envelope Phase Control of Femtosecond Mode-Locked Lasers and Direct Optical Frequency Synthesis, Science, **288**, 635 (2000).

[163] https://www.nobelprize.org/prizes/physics/2018/summary/.

[164] R. Dörner, V. Mergel, O. Jagutzki, L. Spielberger, J. Ullrich, R. Moshammer, H. Schmidt-Böcking, Cold Target Recoil Ion Momentum Spectroscopy: a 'momentum microscope' to view atomic collision dynamics, Physics Reports, **330**, 95 (2000).

[165] J. Ullrich, R. Moshammer, A. Dorn, R. D rner, L.P.H. Schmidt, H. Schmidt-B cking, Recoil-ion and electron momentum spectroscopy: reaction-microscopes, Reports on Progress in Physics, **66**, 1463 (2003).

[166] A.T.J.B. Eppink, D.H. Parker, Velocity map imaging of ions and electrons using electrostatic lenses: Application in photoelectron and photofragment ion imaging of molecular oxygen, Review of Scientific Instruments, **68**, 3477 (1997).

[167] M.J.J. Vrakking, An iterative procedure for the inversion of two-dimensional ion/photoelectron imaging experiments, Review of Scientific Instruments, **72**, 4084 (2001).

[168] E. Narevicius, C.G. Parthey, A. Libson, J. Narevicius, I. Chavez, U. Even, M.G. Raizen, An atomic coilgun: using pulsed magnetic fields to slow a supersonic beam, New Journal of Physics, **9**, 358 (2007).

[169] http://roentdek.com/.

[170] B. Lavorel, P. Babilotte, G. Karras, F. Billard, E. Hertz, O. Faucher, Measurement of dichroism in aligned molecules, Physical Review A, **94**, 043422 (2016).

[171] P. Peng, Y. Bai, N. Li, P. Liu, Measurement of field-free molecular alignment by balanced weak field polarization technique, AIP Advances, **5**, 127205 (2015).

[172] G. Giraud, C.M. Gordon, I.R. Dunkin, K. Wynne, The effects of anion and cation substitution on the ultrafast solvent dynamics of ionic liquids: A time-resolved optical Kerr-effect spectroscopic study, The Journal of chemical physics, **119**, 464 (2003).

[173] R.A. Bartels, T.C. Weinacht, N. Wagner, M. Baertschy, C.H. Greene, M.M. Murnane, H.C. Kapteyn, Phase Modulation of Ultrashort Light Pulses using Molecular Rotational Wave Packets, Physical review letters, **88**, 013903 (2001).

[174] V. Loriot, P. Tzallas, E.P. Benis, E. Hertz, B. Lavorel, D. Charalambidis, O. Faucher, Laser-induced field-free alignment of the OCS molecule, Journal of Physics B: Atomic, Molecular and Optical Physics, **40**, 2503 (2007).

[175] S. Varma, Y.H. Chen, H.M. Milchberg, Trapping and Destruction of Long-Range High-Intensity Optical Filaments by Molecular Quantum Wakes in Air, Physical review letters, **101**, 205001 (2008).

[176] V. Renard, O. Faucher, B. Lavorel, Measurement of laser-induced alignment of molecules by cross defocusing, Opt. Lett., **30**, 70 (2005).

[177] N. Xu, C. Wu, Y. Gao, Nonintrusive measurement of field-free molecular alignment, Applied Physics B, **97**, 635 (2009).

[178] https://www.thinksrs.com/downloads/pdfs/manuals/SR810m.pdf.

[179] F. Sun, W. Zhang, P. Lu, Q. Song, K. Lin, Q. Ji, J. Ma, H. Li, J. Qiang, X. Gong, H. Li, J. Wu, Dissociative frustrated double ionization of N_2Ar dimers in strong laser fields, Journal of Physics B: Atomic, Molecular and Optical Physics, **53**, 035601 (2020).

[180] W. Zhang, H. Li, X. Gong, P. Lu, Q. Song, Q. Ji, K. Lin, J. Ma, H. Li, F. Sun, J. Qiang, H. Zeng, J. Wu, Tracking the electron recapture in dissociative frustrated double ionization of D_2, Physical Review A, **98**, 013419 (2018).

[181] S. Larimian, S. Erattupuzha, A. Baltuška, M. Kitzler-Zeiler, X. Xie, Frustrated double ionization of argon atoms in strong laser fields, Physical Review Research, **2**,

013021 (2020).

[182] F. Sun, X. Chen, W. Zhang, J. Qiang, H. Li, P. Lu, X. Gong, Q. Ji, K. Lin, H. Li, J. Tong, F. Chen, C. Ruiz, J. Wu, F. He, Longitudinal photon-momentum transfer in strong-field double ionization of argon atoms, Physical Review A, **101**, 021402 (2020).

[183] J. Ma, H. Li, K. Lin, Q. Ji, W. Zhang, H. Li, F. Sun, J. Qiang, P. Lu, X. Gong, J. Wu, Dissociative frustrated multiple ionization of hydrogen chloride in intense femtosecond laser fields, Physical Review A, **99**, 023414 (2019).

[184] F. Penent, P. Lablanquie, R.I. Hall, M. Žitnik, K. Bučar, S. Stranges, R. Richter, M. Alagia, P. Hammond, J.G. Lambourne, Observation of Triplet Doubly Excited States in Single Photon Excitation from Ground State Helium, Physical review letters, **86**, 2758 (2001).

[185] F.A. Ilkov, J.E. Decker, S.L. Chin, Ionization of atoms in the tunnelling regime with experimental evidence using Hg atoms, Journal of Physics B: Atomic, Molecular and Optical Physics, **25**, 4005 (1992).

[186] J. Ma, H. Li, K. Lin, Q. Song, Q. Ji, W. Zhang, H. Li, F. Sun, J. Qiang, P. Lu, X. Gong, H. Zeng, J. Wu, Prompt and delayed Coulomb explosion of doubly ionized hydrogen chloride molecules in intense femtosecond laser fields, Physical Review A, **97**, 063407 (2018).

[187] J. Ma, W. Zhang, K. Lin, Q. Ji, H. Li, F. Sun, J. Qiang, F. Chen, J. Tong, P. Lu, H. Li, X. Gong, J. Wu, Strong-field dissociative Rydberg excitation of oxygen molecules: Electron-nuclear correlation, Physical Review A, **100**, 063413 (2019).

[188] A. Hishikawa, S. Liu, A. Iwasaki, K. Yamanouchi, Light-induced multiple electronic-state coupling of O_2^+ in intense laser fields, The Journal of chemical physics, **114**, 9856 (2001).

[189] H. Liu, S.-F. Zhao, M. Li, Y. Deng, C. Wu, X.-X. Zhou, Q. Gong, Y. Liu, Molecular-frame photoelectron angular distributions of strong-field tunneling from inner orbitals, Physical Review A, **88**, 061401 (2013).

[190] P. Eckle, A.N. Pfeiffer, C. Cirelli, A. Staudte, R. Dörner, H.G. Muller, M. Büttiker, U. Keller, Attosecond Ionization and Tunneling Delay Time Measurements in Helium, Science, **322**, 1525 (2008).

[191] A.N. Pfeiffer, C. Cirelli, M. Smolarski, R. Dörner, U. Keller, Timing the release in sequential double ionization, Nature Physics, **7**, 428 (2011).

[192] L.D.A. Siebbeles, M. Glass-Maujean, O.S. Vasyutinskii, J.A. Beswick, O. Roncero, Vector properties in photodissociation: Quantum treatment of the correlation between the spatial anisotropy and the angular momentum polarization of the fragments, The Journal of chemical physics, **100**, 3610 (1994).

[193] Junyang Ma, Kang Lin, Qinying Ji, Wenbin Zhang, Hanxiao Li, Fenghao Sun, Junjie Qiang, Peifen Lu, Hui Li, Xiaochun Gong, J. Wu, Coulomb exploded directional double ionization of N_2O molecules in multicycle femtosecond laser pulses, Chinese Physics B, **28**, 93301 (2019).

[194] M. Moix Teixidor, F. Pirani, P. Candori, S. Falcinelli, F. Vecchiocattivi, Predicted structure and energetics of HCl_2^+, Chemical Physics Letters, **379**, 139 (2003).

[195] H. Akagi, T. Otobe, A. Staudte, A. Shiner, F. Turner, R. Dörner, D.M. Villeneuve, P.B. Corkum, Laser Tunnel Ionization from Multiple Orbitals in HCl, Science, **325**, 1364 (2009).

[196] N. Kotsina, S. Kaziannis, S. Danakas, C. Kosmidis, Selective ionization/dissociation of oriented N_2O molecules by asymmetric fs laser field, The Journal of chemical physics, **139**, 104313 (2013).

[197] M. Kübel, A.S. Alnaser, B. Bergues, T. Pischke, J. Schmidt, Y. Deng, C. Jendrzejewski, J. Ullrich, G.G. Paulus, A.M. Azzeer, U. Kleineberg, R. Moshammer, M.F. Kling, Strong-field control of the dissociative ionization of N_2O with near-single-cycle pulses, New Journal of Physics, **16**, 065017 (2014).

[198] S. Taylor, J.H.D. Eland, M. Hochlaf, Fluorescence and metastability of N_2O^{2+}: Theory and experiment, The Journal of chemical physics, **124**, 204319 (2006).

[199] M. Drescher, M. Hentschel, R. Kienberger, M. Uiberacker, V. Yakovlev, A. Scrinzi, T. Westerwalbesloh, U. Kleineberg, U. Heinzmann, F. Krausz, Time-resolved atomic inner-shell spectroscopy, Nature, **419**, 803 (2002).

[200] L. Fang, M. Hoener, O. Gessner, F. Tarantelli, S.T. Pratt, O. Kornilov, C. Buth, M. Gühr, E.P. Kanter, C. Bostedt, J.D. Bozek, P.H. Bucksbaum, M. Chen, R. Coffee, J. Cryan, M. Glownia, E. Kukk, S.R. Leone, N. Berrah, Double Core-Hole Production in N2: Beating the Auger Clock, Physical review letters, **105**, 083005 (2010).

[201] G. Goldsztejn, T. Marchenko, R. Püttner, L. Journel, R. Guillemin, S. Carniato, P. Selles, O. Travnikova, D. Céolin, A.F. Lago, R. Feifel, P. Lablanquie, M.N. Piancastelli, F. Penent, M. Simon, Double-Core-Hole States in Neon: Lifetime, Post-Collision Interaction, and Spectral Assignment, Physical review letters, **117**, 133001 (2016).

[202] A. Perry-Sassmannshausen, T. Buhr, A. Borovik, M. Martins, S. Reinwardt, S. Ricz, S.O. Stock, F. Trinter, A. Müller, S. Fritzsche, S. Schippers, Multiple Photodetachment of Carbon Anions via Single and Double Core-Hole Creation, Physical review letters, **124**, 083203 (2020).

[203] N. Rohringer, D. Ryan, R.A. London, M. Purvis, F. Albert, J. Dunn, J.D. Bozek, C. Bostedt, A. Graf, R. Hill, S.P. Hau-Riege, J.J. Rocca, Atomic inner-shell X-ray laser at 1.46 nanometres pumped by an X-ray free-electron laser, Nature, **481**, 488 (2012).

[204] H. Sann, C. Schober, A. Mhamdi, F. Trinter, C. Müller, S.K. Semenov, M. Stener, M. Waitz, T. Bauer, R. Wallauer, C. Goihl, J. Titze, F. Afaneh, L.P.H. Schmidt, M. Kunitski, H. Schmidt-Böcking, P.V. Demekhin, N.A. Cherepkov, M.S. Schöffler, T. Jahnke, R. Dörner, Delocalization of a Vacancy across Two Neon Atoms Bound by the van der Waals Force, Physical review letters, **117**, 263001 (2016).

[205] S. Fleischer, I.S. Averbukh, Y. Prior, Selective Alignment of Molecular Spin Isomers, Physical review letters, **99**, 093002 (2007).

[206] S. Fleischer, Y. Khodorkovsky, Y. Prior, I. Sh Averbukh, Controlling the sense of

molecular rotation, New Journal of Physics, **11**, 105039 (2009).

[207] C.H. Lin, J.P. Heritage, T.K. Gustafson, R.Y. Chiao, J.P. McTague, Birefringence arising from the reorientation of the polarizability anisotropy of molecules in collisionless gases, Physical Review A, **13**, 813 (1976).

[208] M. Reichert, P. Zhao, J.M. Reed, T.R. Ensley, D.J. Hagan, E.W. Van Stryland, Beam deflection measurement of bound-electronic and rotational nonlinear refraction in molecular gases, Opt. Express, **23**, 22224 (2015).

[209] M.Z. Hoque, M. Lapert, E. Hertz, F. Billard, D. Sugny, B. Lavorel, O. Faucher, Observation of laser-induced field-free permanent planar alignment of molecules, Physical Review A, **84**, 013409 (2011).

[210] C.P. Koch, M. Lemeshko, D. Sugny, Quantum control of molecular rotation, Reviews of Modern Physics, **91**, 035005 (2019).

[211] P.R. Bunker, Molecular Symmetry and Spectroscopy, 1st ed. (Academic Press, New York, 1979).

[212] A. Rouzée, S. Guérin, O. Faucher, B. Lavorel, Field-free molecular alignment of asymmetric top molecules using elliptically polarized laser pulses, Physical Review A, **77**, 043412 (2008).

[213] A.R. Edmonds, Angular Momentum in Quantum Mechanics, 3rd ed. (Princeton University Press, Princeton, NJ, 1974).

[214] R.N. Zare, Angular Momentum: Understanding Spatial Aspects in Chemistry and Physics (Wiley, New York, 1988).

[215] M. Artamonov, T. Seideman, Optimal-control approach to field-free three-dimensional alignment of polyatomic molecules, Physical Review A, **82**, 023413 (2010).

[216] K.F. Lee, D.M. Villeneuve, P.B. Corkum, A. Stolow, J.G. Underwood, Field-Free Three-Dimensional Alignment of Polyatomic Molecules, Physical review letters, **97**, 173001 (2006).

[217] L.S. Spector, M. Artamonov, S. Miyabe, T. Martinez, T. Seideman, M. Guehr, P.H. Bucksbaum, Axis-dependence of molecular high harmonic emission in three dimensions, Nature Communications, **5**, 3190 (2014).

[218] M. Yoshida, N. Takemoto, Y. Ohtsuki, Three-dimensional alignment of asymmetric-top molecules induced by polarization-shaped optimal laser pulses, Physical Review A, **98**, 053434 (2018).

[219] R. Damari, S. Kallush, S. Fleischer, Rotational Control of Asymmetric Molecules: Dipole- versus Polarizability-Driven Rotational Dynamics, Physical review letters, **117**, 103001 (2016).

[220] T. Grohmann, M. Leibscher, Nuclear spin selective alignment of ethylene and analogues, The Journal of chemical physics, **134**, 204316 (2011).

[221] L.F. Pašteka, M. Melicherčík, P. Neogrády, M. Urban, CASPT2 and CCSD(T) calculations of dipole moments and polarizabilities of acetone in excited states, Molecular Physics, **110**, 2219 (2012).

[222] V.V. Ilyushin, J.T. Hougen, A fitting program for molecules with two equivalent methyl tops and C2v point-group symmetry at equilibrium: Application to existing microwave, millimeter, and sub-millimeter wave measurements of acetone, Journal of Molecular Spectroscopy, **289**, 41 (2013).

[223] M. T. von Ratzsch, C. Wohlforth, A. U. Credo, Jarmuschewitsch, U. Nehmer, Dipolmomente und polarisierbarkeiten polarer stoffe ans statischen dkmessungen, Z. Phys. Chem. 257, 161, (1976).

[224] O. Dorosh, Z. Kisiel, Electric dipole moments of acetone and of acetic acid measured in supersonic expansion, Acta Phys. Pol. A 112, S95, (2007).

[225] S.K. Kim, S. Pedersen, A.H. Zewail, Direct femtosecond observation of the transient intermediate in the α-cleavage reaction of $(CH3)_2CO$ to $2CH_3$+CO: Resolving the issue of concertedness, The Journal of chemical physics, **103**, 477 (1995).

[226] J.C. Owrutsky, A.P. Baronavski, Ultrafast photodissociation dynamics of the S1

and S2 states of acetone, The Journal of chemical physics, **110**, 11206 (1999).

[227] N. Rusteika, K.B. Møller, T.I. Sølling, New insights on the photodynamics of acetone excited with 253−288nm femtosecond pulses, Chemical Physics Letters, **461**, 193 (2008).

[228] J.F. Reintjes, Nonlinear Optical Parametric Processes in Liquids and Gases, Vol. 1 (Academic Press, Orlando, 1984) p. 466.

[229] O. Faucher, E. Prost, E. Hertz, F. Billard, B. Lavorel, A.A. Milner, V.A. Milner, J. Zyss, I.S. Averbukh, Rotational Doppler effect in harmonic generation from spinning molecules, Physical Review A, **94**, 051402 (2016).

[230] J. Houzet, E. Hertz, F. Billard, B. Lavorel, O. Faucher, Molecular alignment allows low-order harmonic generation by circular light in a gas, Physical Review A, **88**, 023859 (2013).

[231] E. Prost, H. Zhang, E. Hertz, F. Billard, B. Lavorel, P. Bejot, J. Zyss, I.S. Averbukh, O. Faucher, Third-order-harmonic generation in coherently spinning molecules, Physical Review A, **96**, 043418 (2017).

[232] H. Zhang, B. Lavorel, F. Billard, J.M. Hartmann, E. Hertz, O. Faucher, J. Ma, J. Wu, E. Gershnabel, Y. Prior, I.S. Averbukh, Rotational Echoes as a Tool for Investigating Ultrafast Collisional Dynamics of Molecules, Physical review letters, **122**, 193401 (2019).

[233] J. Ma, H. Zhang, B. Lavorel, F. Billard, J. Wu, C. Boulet, J.M. Hartmann, O. Faucher, Ultrafast collisional dissipation of symmetric-top molecules probed by rotational alignment echoes, Physical Review A, **101**, 043417 (2020).

[234] J. Ma, H. Zhang, B. Lavorel, F. Billard, E. Hertz, J. Wu, C. Boulet, J.-M. Hartmann, O. Faucher, Observing collisions beyond the secular approximation limit, Nature Communications, **10**, 5780 (2019).

[235] J.M. Hartmann, J. Ma, T. Delahaye, F. Billard, E. Hertz, J. Wu, B. Lavorel, C. Boulet, O. Faucher, Molecular alignment echoes probing collision-induced rotational-

speed changes, Physical Review Research, **2**, 023247 (2020).

[236] J.R. Taylor, An Introduction to Error Analysis: The Study of Uncertainties in Physical Measurements, 2nd ed. , 1997.

[237] R. Hellmann, Reference Values for the Second Virial Coefficient and Three Dilute Gas Transport Properties of Ethane from a State-of-the-Art Intermolecular Potential Energy Surface, Journal of Chemical & Engineering Data, **63**, 470 (2018).

[238] L. Wang, D. Xie, R. Roy, P.N. Roy, A new four-dimensional ab initio potential energy surface for N2O-He and vibrational band origin shifts for the N_2O-He(N) clusters with N = 1-40, Journal of Chemical Physics, **137**, 2586 (2012).

[239] R.B. Bernstein, Atom-molecule theory: A Guide for the Experimentalist (Plenum Press, New York, 1979).

[240] C.S. Anstöter, B.F.E. Curchod, J.R.R. Verlet, Geometric and electronic structure probed along the isomerisation coordinate of a photoactive yellow protein chromophore, Nature Communications, **11**, 2827 (2020).

[241] H. Akagi, T. Otobe, R. Itakura, Deformation of an inner valence molecular orbital in ethanol by an intense laser field, Science Advances, **5**, eaaw1885 (2019).

[242] J. Nishitani, Y.-i. Yamamoto, C.W. West, S. Karashima, T. Suzuki, Binding energy of solvated electrons and retrieval of true UV photoelectron spectra of liquids, Science Advances, **5**, eaaw6896 (2019).

[243] A.V. Balakin, J.-L. Coutaz, V.A. Makarov, I.A. Kotelnikov, Y. Peng, P.M. Solyankin, Y. Zhu, A.P. Shkurinov, Terahertz wave generation from liquid nitrogen, Photon. Res., **7**, 678 (2019).

List of Publications

1. **J. Ma**, H. Zhang, B. Lavorel, F. Billard, E. Hertz, J. Wu, C. Boulet, J. Hartmann, and O. Faucher, “Observing collisions beyond the secular approximation limits”, **Nature Communications** 10, 5780 (2019).

2. **J. Ma**, H. Zhang, B. Lavorel, F. Billard, J. Wu, C. Boulet, J. Hartmann, and O. Faucher, “Ultrafast collisional dissipation of symmetric-top molecules probed by rotational alignment echoes”, **Phys. Rev. A** 101, 043417 (2020).

3. **J. Ma**, H. Li, K. Lin, Q. Ji, W. Zhang, H. Li, F. Sun, J. Qiang, P. Lu, X. Gong, and J. Wu, “Dissociative frustrated multiple ionization of hydrogen chloride in intense femtosecond laser fields”, **Phys. Rev. A** 99, 023414 (2019).

4. **J. Ma**, W. Zhang, K. Lin, Q. Ji, H. Li, F. Sun, J. Qiang, F. Chen, J. Tong, P. Lu, H. Li, X. Gong, and J. Wu, “Strong-field dissociative Rydberg excitation of oxygen molecules: Electron-nuclear correlation”, **Phys. Rev. A** 100, 063413 (2019).

5. **J. Ma**, H. Li, K. Lin, Q. Song, Q. Ji, W. Zhang, H. Li, F. Sun, J. Qiang, P. Lu, X. Gong, H. Zeng and J. Wu, “Prompt and delayed Coulomb explosion of doubly ionized hydrogen chloride molecules in intense femtosecond laser fields”, **Phys. Rev. A** 97, 063407 (2018).

6. **J. Ma**, K. Lin, Q. Ji, W. Zhang, H. Li, F. Sun, J. Qiang, P. Lu, H. Li, X. Gong, and J. Wu, “Coulomb exploded directional double ionization of N_2O molecules in multicycle femtosecond laser pulses”, **Chin. Phys. B** 28, 093301 (2019).

7. **J. Ma**, H. Ni, C. Lu, W. Zhang, P. Lu, O. Faucher, and J. Wu, “Transient valence charge localization in strong-field dissociative ionization of HCl molecules”, submit to **Phys. Rev. Lett.** (in review).

8. **J. Ma**, L. H. Coudert, F. Billard, M. Bournazel, B. Lavore, J. Wu, G. Maroulis, J.-M. Hartmann, and O. Faucher, “Echo-assisted impulsive alignment of room-temperature acetone molecules”, submit to **Phys. Rev. Research** (in review).

9. J. Hartmann, **J. Ma**, T. Delahaye, F. Billard, E. Hertz, J. Wu, B. Lavorel, C. Boulet, and O. Faucher, "Molecular alignment echoes probing collision-induced rotational-speed changes", **Phys. Rev. Research** 2, 023247 (2020).

10. K. Lin, I. Tutunnikov, **J. Ma**, J. Qiang, L. Zhou, O. Faucher, Y. Prior, I. Averbukh, and J. Wu, "Spatiotemporal rotational dynamics of laser-driven molecules", **Advanced Photonics** 2, 024002 (2020)

11. H. Zhang, B. Lavorel, F. Billard, J.-M. Hartmann, E. Hertz, O. Faucher, **J. Ma**, J. Wu, E. Gershnabel, Y. Prior, and I. Sh. Averbukh, "Rotational Echoes as a Tool for Investigating Ultrafast Collisional Dynamics of Molecules", **Phys. Rev. Lett.** 122, 193401 (2019).

12. K. Lin, I. Tutunnikov, J. Qiang, **J. Ma**, Q. Song, Q. Ji, W. Zhang, H. Li, F. Sun, X. Gong, H. Li, P. Lu, H.Zeng, Y. Prior, I. Averbukh, and J. Wu, "All-optical fieldfree three-dimensional orientation of asymmetric-top molecules", **Nature Communications** 9, 5134 (2018).

13. W. Zhang, X. Gong, H. Li, P. Lu, F. Sun, Q. Ji, K. Lin, **J. Ma**, H. X. Li, J. Qiang, F. He, and J. Wu, "Electron-nuclear correlated multiphoton-route to Rydberg fragments of molecules", **Nature Communications** 10, 757 (2019).

14. K. Lin, X. Jia, Z. Yu, F. He, **J. Ma**, H. Li, X. Gong, Q. Song, Q. Ji, W. Zhang, H. Li, P. Lu, H. Zeng, J. Chen, and J. Wu, "Comparison study of strong-field ionization of molecules and atoms by bicircular two-color femtosecond laser pulses", **Phys. Rev. Lett.** 119, 203202 (2017).

15. K. Lin, **J. Ma**, X. Gong, Q. Song, Q. Ji, W. Zhang, H. Li, P. Lu, H. Li, H. Zeng, J. Wu, J. Hartmann, O. Faucher, E. Gershnabel, Y. Prior, and I. Averbukh, "Rotated echoes of molecular alignment: fractional, high order and imaginary", **Opt. Express** 25, 24917 (2017).

16. K. Lin, P. Lu, **J. Ma**, X. Gong, Q. Song, Q. Ji, W. Zhang, H. Zeng, J. Wu, G. Karras, G. Siour, J. Hartmann, O. Faucher, E. Gershnabel, Y. Prior, and I. Sh. Averbukh,

"Echoes in space and time", **Phys. Rev. X** 6, 041056 (2016).

17. X. Gong, P. He, **J. Ma**, W. Zhang, F. Sun, Q. Ji, K. Lin, H. Li, J. Qiang, P. Lu, H. Li, H. Zeng, J. Wu, and F. He, "Observation of photon-nucleus angular-momentum transfer in the strong-field breaking of molecules", **Phys. Rev. A** 99, 063407 (2019).

18. W. Zhang, Z. Li, P. Lu, X. Gong, Q. Song, Q. Ji, K. Lin, **J. Ma**, F. He, H. Zeng, and J. Wu, "Photon energy deposition in strong-field single ionization of multielectron molecules", **Phys. Rev. Lett.** 117, 103002 (2016).

19. W. Zhang, Z. Yu, X. Gong, J. Wang, P. Lu, H. Li, Q. Song, Q. Ji, K. Lin, **J. Ma**, H. X. Li, F. Sun, J. Qiang, H. Zeng, F. He, and J. Wu, "Visualizing and steering dissociative frustrated double ionization of hydrogen molecules", **Phys. Rev. Lett.** 119, 253202 (2017).

20. W. Zhang, P. Lu, X. Gong, H. Li, Q. Ji, K. Lin, **J. Ma**, H. Li, F. Sun, J. Qiang, Fei Chen, J. Tong, and Jian Wu, "Electron trapping in strong-field dissociative frustrated ionization of CO molecules", **Phys. Rev. A** 101, 033401 (2020).

21. W. Zhang, H. Li, K. Lin, P. Lu, X. Gong, Q. Song, Q. Ji, **J. Ma**, H. Li, H. Zeng, F. He, and J. Wu, "Photon-number-resolved asymmetric dissociative single ionization of H_2", **Phys. Rev. A.** 96. 033405 (2017).

22. W. Zhang, H. Li, X. Gong, P. Lu, Q. Song, Q. Ji, K. Lin, **J. Ma**, H. X. Li, F. Sun, J. Qiang, H. Zeng, and J. Wu, "Tracking the electron recapture in the dissociative frustrated double ionization of D2", **Phys. Rev. A** 98, 013419 (2018).

23. W. Zhang, P. Lu, **J. Ma**, H. Li, X. Gong, and J. Wu, "Correlated electron-nuclear dynamics of molecules in strong fields", **Invited Review** (**J. Phys. B,** in press).

24. F. Sun, W. Zhang, P. Lu, Q. Song, K. Lin, Q. Ji, **J. Ma**, H. Li, J. Qiang, X. Gong, H. Li and J. Wu, "Dissociative frustrated double ionization of N_2Ar dimers in strong laser fields", **J. Phys. B** 53, 035601 (2020).

25. Q. Ji, S. Pan, P. He, J. Wang, P. Lu, H. Li, X. Gong, K. Lin, W. Zhang, **J. Ma**, H. Li, C. Duan, P. Liu, Y. Bai, R. Li, F. He, and J. Wu, "Timing dissociative ionization of

H_2 using a polarization-skewed femtosecond laser pulse", **Phys. Rev. Lett.** 123, 233202 (2019).

26. P. Lu, J. Wang, H. Li, K. Lin, X. Gong, Q. Song, Q. Ji, W. Zhang, **J. Ma**, H. Li, H. Zeng, F. He, and J. Wu, "High-order above-threshold dissociation of molecules", **PNAS** 115, 2049 (2018).

27. Q. Song, H. Li, J. Wang, P. Lu, X. Gong, Q. Ji, K. Lin, W. Zhang, **J. Ma**, H. Li, H. Zeng, F. He, and J. Wu, "Double ionization of nitrogen molecules in orthogonal two-color femtosecond laser fields", **J. Phys. B** 51, 074002 (2018).

28. X. Gong, C. Lin, F. He, Q. Song, K. Lin, Q. Ji, W. Zhang, **J. Ma**, P. Lu, Y. Liu, H. Zeng, W. Yang, and J. Wu, "Energy-resolved ultrashort delays of photoelectron emission clocked by orthogonal two-color laser fields", **Phys. Rev. Lett.** 118, 143203 (2017).

29. Q. Ji, J. Wang, P. Lu, H. Li, X. Gong, Q. Song, K. Lin, W. Zhang, **J. Ma**, M. Kling, H. Zeng, J. Wu, and F. He, "Subcycle characterization of photoelectron emission with multicycle laser pulses", **Phys. Rev. A** 96, 053423 (2017).

30. Q. Song, P. Lu, X. Gong, Q. Ji, K. Lin, W. Zhang, **J. Ma**, H. Zeng, and J. Wu, "Dissociative double ionization of CO in orthogonal two-color laser fields", **Phys. Rev. A** 95, 013406 (2017).

31. P. Lu, W. Zhang, X. Gong, Q. Song, K. Lin, Q. Ji, **J. Ma**, F. He, H. Zeng, and J. Wu, "Electron-nuclear correlation in above-threshold double ionization of molecules", **Phys. Rev. A** 95, 033404 (2017).

32. Q. Song, Z. Li, H. Li, P. Lu, X. Gong, Q. Ji, K. Lin, W. Zhang, **J. Ma**, H. Zeng, F.He, and J. Wu, "Orientation-dependent strong-field dissociative single ionization of CO", **Opt. Express** 25, 2221 (2017).

33. X. Gong, H. Li, P. Lu, Q. Song, Q. Ji, K. Lin, W. Zhang, **J. Ma**, H. Li, H. Zeng and J. Wu, "Ellipticity dependent symmetric break of doubly ionized acetylene in strong laser fields", **J. Opt.** 19, 124008 (2017).

34. Q. Song, Z. Li, S. Cui, P. Lu, X. Gong, Q. Ji, K. Lin, W. Zhang, **J. Ma**, H. Pan, J. Ding, M. F. Kling, H. Zeng, F. He, and J. Wu, "Disentangling the role of laser coupling in directional breaking of molecules", **Phys. Rev. A** 94, 053419 (2016).

35. K. Lin, X. Gong, Q. Song, Q. Ji, W. Zhang, **J. Ma**, P. Lu, H. Pan, J. Ding, H. Zeng, and J. Wu, "Directional bond breaking by polarization-gated two-color ultrashort laser pulses", **J. Phys. B** 49, 025603 (2016).

Awards

1. China Scholarship Council, 2018

2. The President’s Scholarship of East China Normal University, 2020

Acknowledgment

It would be a right moment for me to express my deepest gratitude to all those who give me the possibility to complete this long and special journey.

The research work of my thesis is the well cooperation of East China Normal University in China and Université Bourgogne Franche-Comté in France. I am deeply indebted to my two supervisors Prof. Jian WU and Prof. Olivier FAUCHER, who provide me with consistent care, help, support and encouragement during my PhD years. I am greatly benefited from all the promising projects they assigned to me. Their rigorous academic insight enlighten me not only in the past years but also in my future career. They also help me a lot in daily life, especially during the two years I studied in France. I feel words cannot express how thankful I am.

I would like to thank Dr. Jean-Michel HARTMANN, Dr. Laurent COUDERT and Prof. Christian BOULET for conducting the theoretical simulations. Without their support and help, a lot of work would have never been accomplished. The discussions with them help me to have a deeper understanding of ultrafast molecular rotational and collisional dynamics.

I want to thank all the *PFL* group members in France. I am thankful to Dr. Bruno LAVOREL for his valuable guidance through all the experiment and data analysis. His passion in the scientific work impressed me a lot. He could not even realize how much I have learned from him. I would like to thank Dr. Franck BILLARD for helping me deal with a lot of experiment problems. He is the best engineer I have ever met. I would like to appreciate Dr. Pierre BEJOT, Prof. Frédéric CHAUSSARD, and Prof. Edouard HERTZ for sharing their rich knowledge and experiences. I want to thank Ester SZMYGEL and Manon BOURNAZEL, as well as former members Postdoc Dr. Haisu ZHANG, Dr. Emilien PROST, and Jérémy BERT.

Many thanks to members working on the *MOLSF* group in China. I would like to

thank Dr. Xiaochun GONG for his a lot of useful advices on the experiment operation and data explanation. I would like to thank Dr. Hui LI for her help in about any possible circumstance and the correction of my first scientific manuscript. I would like to thank Dr. Peifen LU for helping me on experiment skills including the operation of laser system. I would like to thank Dr. Hongcheng NI for his help on the theoretical calculations and reading my thesis. I am thankful to Dr. Zheng SUN, Dr. Qiying SONG, Dr. Qinying JI, Dr. Kang LIN, Dr. Wenbin ZHANG, Hanxiao LI, Fenghao SUN, Junjie QIANG, Jihong TONG, Fei CHEN, Lianrong ZHOU, Wenyu JIANG, Shengzhe PAN, Yongzhe MA, Xiaodan MAO, Shanshan SONG, Chenxu LU, Jiawei WANG, Postdoc Dr. Jian GAO and undergraduate Yue HU. I thank Wenbin for helping me to deal with all kinds of my affaires when I was not in China.

I deeply appreciate the supports from so many researchers in the Lab of ECNU and UBFC, among them Prof. Heping Zeng, Prof. E WU, Dr. Wenxue LI, Dr. Guang WU, Dr. Haifeng PAN, Dr. Shian ZHANG, Prof. Olivier MUSSET, Bernard SINARDET, and Stéphane PERNOT.

I would like to thank my supportive friends Xiaofei JU, Xiao YU, Gang XU, Kaipeng LIU, Haisu ZHANG and his wife Jinhong CAO when I studied in Dijon.

Especially, I would like to express my heartfelt thanks to Olivier’s family for inviting me to the family gathering many times, including celebrating Christmas and New Year.

I would like to thank my thesis reviewers for their carefully reading the entire manuscript and making many helpful suggestions to improve the quality of this thesis.

Last but not least, I have to express my greatest acknowledgement to my family for their understanding and support during all these years.

Shanghai, China

2021/04/10